Stony Brook University

Cavitation Phenomena in Hyperelastic Solids: A Finite-Element Approach

A Thesis Presented

by

Yu Chen

to

The Graduate School

in Partial Fulfillment of the

Requirements

for the Degree of

Master of Science

in

Mechanical Engineering

Stony Brook University

December 2009

Stony Brook University

The Graduate School

Yu Chen

We, the thesis committee for the above candidate for the

Master of Science degree, hereby recommend

acceptance of this thesis.

Oscar Lopez-Pamies – Thesis Advisor

Assistant Professor – Department of Mechanical Engineering

Toshio Nakamura – Chairperson of Defense

Professor – Department of Mechanical Engineering

Chad Korach – Member of Defense

Assistant Professor – Department of Mechanical Engineering

This thesis is accepted by the Graduate School

Lawrence Martin

Dean of the Graduate School

Abstract of the Thesis

Cavitation Phenomena in Hyperelastic Solids: A Finite-Element Approach

by

Yu Chen

Master of Science

in

Mechanical Engineering

Stony Brook University

2009

Physical evidence has shown that sufficiently large tensile loads can induce the sudden appearance of internal cavities in soft solids (i.e., solids that are able to undergo large reversible deformations). The occurrence of such instabilities, commonly referred to as cavitation, can be attributed to the growth of pre-existing defects into finite sizes. Because of its close connection with material failure initiation, the phenomenon of cavitation has received much attention from the materials and mechanics communities. Cavitation has also been a subject of interest in the mathematical community because its modeling has prompted the development of techniques to deal with a broad class of nonconvex variational problems. While in recent years considerable progress has been made via energy minimization methods to establish existence results, fundamental problems regarding the quantitative prediction of the occurrence of cavitation in real material systems remain largely unresolved.

The main objective of this thesis is to make use of the finite element method (FEM) to investigate the onset of cavitation in nonlinear elastic materials that are subjected to generally nonsymmetric loading conditions. To this end, we first cast the phenomenon of cavitation as the boundary value problem of a nonlinear elastic material, which contains a single infinitesimally small vacuous cavity (i.e., a vacuous defect), that is subjected to uniform displacement boundary conditions. By means of FEM, we then generate numerical solutions for such a problem. These include solutions for the change in size of the underlying cavity as a function of the applied loading conditions, from which we are able to determine the onset of cavitation corresponding to the event when the (initially infinitesimal) cavity suddenly grows into finite sizes. The focus is on 2D compressible isotropic materials, but some 3D problems are also explored. Comparisons with cavitation criteria recently developed in the literature are also included.

To my parents and friends

for their supports

Table of Contents

List of Figures

Acknowledgements

The two and a half years' study in pursuing a master degree is the best experience of my life. I am deeply grateful to my advisor, Assistant Professor Oscar Lopez-Pamies. His broad knowledge and passion toward scientific research encourage me to devote myself to the study of cavitation in hyperelastic solids. He is not only a mentor on academics but also with a concern for the well being of his students. Besides my advisor, I also want to thank the rest of my thesis committee, Prof. Nakamura and Chad, who gave me insightful comments and reviewed my work on a very shot of notice.

I also want to thank all my fellow group colleagues: Xi Yang, Chong Huang, Shu Guo, and many others, for their care, support and friendship.

Last but not the least, I want to thank my parents and my girlfriend, for their loving, supporting, concerning and understanding during my graduate study. This thesis is dedicated to them.

To all of you, thank you.

1 Introduction

Under tensile loading conditions, solids—much like fluid—may exhibit cavitation. In elastomers, the occurrence of this phenomenon was first reported by Busse [3], Yerzley [4], and Gent and Lindley [5]. In particular, these authors conducted tension experiments on thin disks of rubber bonded to plane metal end-pieces in such a way that the stress at the center of their specimens was approximately hydrostatic. They observed that flaws in the form of roughly spherical cavities consistently appeared in the rubber disks at well defined values of the applied tensile load. Similar observations were later reported by Lindsey [6]. More recently, the occurrence of cavitation has also been observed in the vicinity of inclusions in particle–reinforced elastomers [7, 8], as well as in the rubber phase of rubber–toughened glassy polymers (see, e.g., [9, 11]).

In a pioneering contribution, Gent and Lindley [6] proposed a criterion for the onset of cavitation in rubber. In essence—making use of the work of Green and Zerna [12] for thick spherical shells—they considered the problem of a spherical cavity of finite size embedded in an infinite matrix subjected to uniform hydrostatic pressure on its boundary, i.e., at infinity. Assuming the matrix to be made out of incompressible Neo-Hookean material, they found that as the applied pressure approaches the critical value $P_{crit} = 5/2\mu$ —with μ denoting the classical shear modulus of the matrix material—the size of the cavity becomes unbounded. In view of this result, they effectively proposed that cavitation occurs at any place in a rubbery solid where the hydrostatic part of the stress reaches the critical value $P_{crit} = 5/2\mu$. Quite remarkably, this criterion turned out to be in very good agreement with their experimental observations.

In a different effort, Ball [13] examined a class of non-smooth bifurcation problems for the equations of nonlinear elastostatics which model the creation of a cavity in the interior of a nonlinearly elastic solid once a critical external load is

attained. Specifically, he considered the problem of a unit ball (in n dimensions), made out of isotropic hyperelastic material, that is subjected to radially symmetric uniform tensile load on its boundary. For certain materials, he found that when the applied load is small, the ball remains a solid ball, but that when the load is sufficiently large, it is energetically more favorable for the material to open up a spherical (or, if n = 2, circular) cavity at the center of the ball.

When specialized to a unit sphere of incompressible Neo-Hookean material, Ball's analysis leads to $P_{crit} = 5/2\mu$ for the critical applied pressure at which a cavity forms at the origin of the sphere. This is exactly the same value obtained by Gent and Lindley [5] for the critical applied pressure at which a pre–existing spherical cavity embedded in an infinite Neo-Hookean medium grows unbounded. The reason for this agreement, as already noticed by Ball [13], is twofold: (i) because of the scaling laws of nonlinear elastostatics, an infinitesimal hole in a finite medium behaves like a finite hole in an infinite medium; and (ii) the solution for the problem of a spherical shell is expected to tend to the solution for the problem of a solid sphere in the limit when the size of the cavity in the shell tends to zero. This connection between the approach of Gent and Lindley [5] and that of Ball [13] reveals that the phenomenon of cavitation in hyperelastic solids can be viewed rather equivalently as: (i) the sudden rapid growth of an imperfection or (ii) a (non-smooth) bifurcation problem in an initially perfect material.

For incompressible materials, the cavitation results put forward by Ball [12] are complete and explicit. For compressible materials, on the other hand, Ball's results are relatively limited. This is because for compressible (unlike for incompressible) solids, it is necessary to solve the underlying nonlinear differential equation of equilibrium. Extensions of Ball's work—yet within the context of radially symmetric cavitation in compressible isotropic materials—have been provided by Stuart [14], Sivaloganathan [15, 16], Horgan and Abeyaratne [17], Horgan [18], and Meynard [19] among others. Radially symmetric cavitation problems in anisotropic materials have been studied, for instance, by Antman and Negron-Marrero [20] and by

Polignone and Horgan [21]. Extensions considering dynamic and surface-energy effects have also been examined by other researchers (see, e.g., [22, 11]). For a review on radially symmetric cavitation, the interested reader is referred to [23].

All of the above-cited efforts address the problem of radially symmetric cavitation. However, the majority of practical situations do not posses radially symmetry. One of the first (and few) studies on non-symmetric cavitation is that of James and Spector [24]. These authors provided a qualitative analysis for the formation of non-spherical cavities in a class of compressible isotropic materials subjected to radially deformations. Furthermore, they showed that non-radially cavities are energetically more favorable than radially ones for certain materials. Later, Hou and Abeyaratne [25] derived an approximate criterion for the onset of cavitation in incompressible isotropic solids subjected to non-symmetric loading. Specifically, these authors examined the boundary value problem of a sphere, containing an infinitesimal spherical cavity at its origin, subjected to uniform Cauchy traction on its boundary. After casting the problem in a variational form, they proposed a particular kinematically admissible trial field as an approximate solution. Making use of this approximation, they then derived an analytical expression for the loci of critical applied stresses (or cavitation surface) at which the initially infinitesimal cavity suddenly becomes of finite size. For the special case of hydrostatic loading, the results of Hou and Abeyaratne [25] have the merit that they recover the exact results of Ball [13] for incompressible materials. For more general loading conditions, on the other hand, their results are expected (by construction) to be conservative. Finally, it should be mentioned that the problem of non-symmetric cavitation has also been studied numerically by some authors (see, e.g., [26]), but mostly in the different context of elastoplasticity (see, e.g., [27, 28]).

The work of this thesis is devoted to a finite-element approach to study of cavitation in compressible, isotropic hyperelastic solids, such as Neo-Hookean material and Blatz-Ko material, under general deformations. We work out the numerical cavitation and compare the FEM results with approximately analytical

solution of 2D problem for Neo-Hookean material on the deformation space and corresponding Cauchy stress space. We also find surface instability for the Blatz-Ko material. The present work on the 3D problem is focused on the study of compressible, isotropic Neo-Hookean material under hydrostatic.

2 Problem Setting

Consider a material made of a vacuous inhomogeneity embedded in an otherwise homogenous matrix. We assume this material has a volume Ω_o, with boundary $\partial\Omega_o$, in the undeformed configuration. Moreover the initial size of the cavity is considered to be much smaller than the size of the specimen, i.e., the cavity is considered to be a small imperfection.

For two-dimension (2D) problem, as mentioned above, we assume that the vacuous inhomogeneity is cylindrical and has initially circular cross section. For convenience, we set the long axis of the void to be parallel to the fixed laboratory basis vector e_3. Further, we take Ω_0 to be infinite in extent (see Figure. 1). The analysis is thus relevant to the sudden growth of a void into an elongated shape.

For three-dimension (3D) problem, we assume that the vacuous inhomogeneity is spherical void in the center of a large cube. Further, we take Ω_0 to be infinite in extent (see Figure. 2). The analysis is thus relevant to the sudden growth of a void into an elongated shape.

Material points in the solid are identified by their initial position vector X in the undeformed configuration Ω_0, while the current position vector of the same point in the deformed configuration Ω is given by $\mathrm{x} = \chi(\mathrm{X})$. Motivated by physical arguments, the mapping χ is required to be continuous (i.e., the material is not allowed to fracture) and one-to-one on Ω_0 (i.e., the material is not allowed to interpenetrate itself). In addition, we also assume that χ is twice continuously differentiable, except possibly on the infomogeneity/matrix boundary. The deformation gradient F at X, a quantity that measures the deformation in the neighborhood of X, is defined by

$$\mathrm{F}=\mathrm{Grad}\chi \quad \text{in} \quad \Omega_0 \tag{1}$$

and is required to satisfy the local material impenetrability constraint $J = \det \mathrm{F} > 0$.

The constitutive behavior of the matrix phase—which occupies the subdomain $\Omega_0^{(1)}$ in the undeformed configuration—is characterized by a stored-energy function $W^{(1)}$ that is an objective, non-convex function of the deformation gradient tensor F. On the other hand, the constitutive behavior of the void-which occupies the subdomain $\Omega_0^{(2)} = \Omega_0 - \Omega_0^{(1)}$—is taken to be characterized by $W^{(2)}$. Note that this prescription directly implies that the cavity is traction-free. It then follows that the local stored-energy function of this two-phase system may be conveniently written as

$$W(\mathrm{X},\mathrm{F}) = (1-\chi_0(\mathrm{X}))W^{(1)}(\mathrm{F}) + \chi_0(\mathrm{X})W^{(2)}(\mathrm{F}) = (1-\chi_0(\mathrm{X}))W^{(1)}(\mathrm{F})\,; \tag{2}$$

where $\chi_0(\mathrm{X})$ is the characteristic function defined as:

$$\chi_0(\mathrm{X}) = \begin{cases} 1 & \mathrm{X} \in \Omega_0^{(2)} \\ 0 & \mathrm{X} \in \Omega_0^{(1)} \end{cases} \tag{3}$$

In this connection, it is noted that the initial volume fraction of the void (or initial porosity) is given by $f_0 \doteqdot \Omega_0^{(2)} \,/\, |\,\Omega_0\,| = \langle \chi_0 \rangle$, where the triangular brackets $\langle \bullet \rangle = (1/|\,\Omega_0\,|)\int_{\Omega_0} \bullet \mathrm{dX}$, which have been defined as the volume average over the specimen in the undeformed configuration. According to compressible isotropic materials, together with that of objectivity, the stored-energy function $W^{(1)}$ can be expressed as function of the principal invariants of the right Cauchy-Green Deformation tensor $\mathrm{C}=\mathrm{F}^{\mathrm{T}}\mathrm{F}$:

$$\begin{aligned} I_1 &= \mathrm{trC} = \lambda_1^2 + \lambda_2^2 + \lambda_3^2 \\ I_2 &= \frac{1}{2}[(\mathrm{trC})^2 - \mathrm{trC}^2] = \lambda_1^2\lambda_2^2 + \lambda_1^2\lambda_2^2 + \lambda_2^2\lambda_3^2 \\ I_3 &= \det\mathrm{C} = \lambda_1^2\lambda_2^2\lambda_3^2 \end{aligned} \tag{4}$$

or, as a symmetric function of the principle stretch $\lambda_1, \lambda_2, \lambda_3$ associated with F. Namely, $W^{(1)}$ may be written as

$$W^{(1)}(\mathrm{F}) = g(I_1, I_2, I_3) = h(\lambda_1, \lambda_2, \lambda_3)\,; \tag{5}$$

where h is symmetric.

The local constitutive relation for the material can then be expressed as

$$\mathrm{S}=\frac{\partial W}{\partial F}(\mathrm{X},\mathrm{F})=(1-\chi_0(\mathrm{X}))\frac{\partial W^{(1)}(\mathrm{F})}{\partial \mathrm{F}}; \tag{6}$$

Here, S denotes the first Piola-Kirchhoff stress tensor and sufficient smoothness has been assumed for $W^{(1)}$ on F.

We suppose now that the body is subjected to the homogeneous displacement boundary condition

$$\mathrm{x}=\bar{\mathrm{F}}\mathrm{X} \quad \text{on} \quad \partial\Omega_o; \tag{7}$$

where the second-order tensor $\bar{\mathrm{F}}$ is a prescribed, constant quantity. In the absence of body forces, it follows that the total elastic energy (per unit undeformed volume) stored in the material is given by

$$E(\bar{\mathrm{F}})=\min_{F\in\kappa(\bar{\mathrm{F}})}\langle W(\mathrm{X},\mathrm{F})\rangle=\min_{F\in\kappa(\bar{\mathrm{F}})}(1-f_0)\langle W^{(1)}(\mathrm{F})\rangle^{(1)} \tag{8}$$

where $\langle\bullet\rangle^{(1)}$ indicates the volume average over the matrix phase $\Omega_0^{(1)}$ and κ stands for the set of kinematically admissible deformation gradient fields:

$$\kappa(\bar{F})=\left\{\mathrm{F}\,|\,\exists \mathrm{x}=\chi(\mathrm{X}) \quad \text{with } \mathrm{F}=\mathrm{Grad}\chi, J>0 \quad \text{in } \Omega_0, \mathrm{x}=\bar{\mathrm{F}}\mathrm{X} \quad \text{on } \partial\Omega_0\right\} \tag{9}$$

Furthermore, the equilibrium equations-the Euler-Lagrange equations associated with the variational problem (8)-take the form:

$$\mathrm{Div}\left[\frac{\partial W}{\partial \mathrm{F}}(\mathrm{X},\mathrm{F})\right]=0 \quad \text{in} \quad \Omega_o; \tag{10}$$

The main idea to the study of the solution of equation (10), subject to the stored-energy function (8) and affine boundary condition (12), in the limit as $f_0\to 0+$ (in the limit when the initial size of the cavity is infinitesimally small). In particular, we are going to determine in this limit the critical values of the applied deformation $\bar{\mathrm{F}}$ at which the actual size of the deformed cavity and define the cavitation criterion by measuring the current porosity in the deformed configuration:

$$f = \frac{\langle \det \mathrm{F} \rangle^{(2)}}{\langle \det \mathrm{F} \rangle} = \frac{\langle \det \mathrm{F} \rangle^{(2)}}{\det \overline{\mathrm{F}}} f_0 \tag{11}$$

suddenly starts growing and becomes finite.

In 2D problem, we will concern on the plane-strain deformations in the $e_1 - e_2$ plane, so that the out-of-plane components of $\overline{\mathrm{F}}$ are given by:

$$\overline{F}_{\alpha\beta} = diag(\overline{\lambda}_1, \overline{\lambda}_2) \tag{12}$$

In 3D problem, we do the similar way:

$$\overline{F}_{\alpha\beta} = diag(\overline{\lambda}_1, \overline{\lambda}_2, \overline{\lambda}_3) \tag{13}$$

3 Approximately Analytical Solution for 2D Problem

3.1 Analytical Cavitation Criterion

To get the cavitation criterion is to solve the system of nonlinear partial differential equations (10) for the above-specified geometry (Figure. 1 and 2), compressible stored-energy function (8), and the general loading conditions (12) is focused on solving the following stationary variational principle instead of solving minimization problem (8)[1]:

$$\widehat{E}(\overline{\mathrm{F}}) = \underset{F\in\kappa(\overline{F})}{\mathrm{stat}} \langle W(\mathrm{X},\mathrm{F})\rangle = \underset{F\in\kappa(\overline{F})}{\mathrm{stat}} (1-f_0)\langle W^{(1)}(\mathrm{F})\rangle^{(1)} \tag{14}$$

where it is emphasized that the stat(ionary) operation means that the total elastic energy $\widehat{E}$ is evaluated at the above-described "principle" solution of the Eular-Lagrange equations (10).

The proposal to solve approximately problem (14) is to make use of the "linear–comparison" variational procedure of Lopez-Pamies and Ponte Castaneda [2]. Specifically, with the help of this approach, we will generate analytical estimates for the total elastic energy (14) and the associated current porosity (11); as explained in the sequel, knowledge of $\widehat{E}$ and f suffices to determine the onset of cavitation in the hyperelastic solid. The key idea of this technique consists in devising an optimally chosen linear comparison medium (LCM) with the same microstructure as the actual hyperelastic material (i.e., the same χ_0) which can then be used to convert available exact results for linear materials into estimates for the hyperelastic material. In the present context (of a single inhomogeneity embedded in an infinite matrix) we will exploit a generalized version of the exact Eshelby solution [30] for linear materials in order to generate an approximate closed-form solution for the actual nonlinear problem (14).

The main procedure of this method is organized as follows. First, we introduce a linear comparison medium (LCM) with the same microstructure as the actual hyperelastic material (i.e., the same χ_0) and with local stored-energy function

$$W_T(\mathrm{X},\mathrm{F}) = (1-\chi_0(\mathrm{X}))W_T^{(1)}(\mathrm{F}) \tag{15}$$

where the quadratic potential $W_T^{(1)}$ is given by the second-order Taylor expansion of the nonlinear stored-energy function $W^{(1)}$ about $\bar{\mathrm{F}}$:

$$W_T^{(1)}(\mathrm{F}) = W^{(1)}(\bar{\mathrm{F}}) + S^{(1)}(\bar{\mathrm{F}})\cdot(\mathrm{F}\text{-}\bar{\mathrm{F}}) + \frac{1}{2}(\mathrm{F}\text{-}\bar{\mathrm{F}})\cdot \mathrm{L}(\mathrm{F}\text{-}\bar{\mathrm{F}}) \tag{16}$$

where $S^{(1)}(\bullet) = \partial W^{(1)}(\bullet)/\partial \mathrm{F}$ and L is a fourth-order tensor with matrix representation:

$$L_{\alpha\beta\gamma\delta} = \begin{bmatrix} l_1 & l_3 & & \\ l_3 & l_2 & & \\ & & l_4 & \sqrt{(l_1-l_4)(l_2-l_4)}-l_3 \\ & & \sqrt{(l_1-l_4)(l_2-l_4)}-l_3 & l_4 \end{bmatrix} \tag{17}$$

where l_I (I=1,2,3,4) are independent variables can be determined by the way in the paper [1] and [31]. With above LCM, we can get an estimate for the total elastic energy (14) for small (but finite) values of initial porosity f_0:

$$\widehat{E}(\bar{\mathrm{F}}) = (1-f_0)\left[W^{(1)}(\widehat{E}^{(1)}) - S^{(1)}(\bar{\mathrm{F}})\cdot(\widehat{E}^{(1)} - \bar{\mathrm{F}}^{(1)})\right] \tag{18}$$

where $\bar{\mathrm{F}}^{(1)} \doteq \langle \mathrm{F}\rangle^{(1)}$ is the average deformation gradient in the matrix phase of the LCM. Then making use of these results, we then construct an estimate for the associated porosity (11) in the deformed configuration:

$$f = \frac{\det \bar{\mathrm{F}}^{(2)}}{\det \bar{\mathrm{F}}} f_0 \tag{19}$$

After that, we consider the limit $f_0 \to 0^+$ of the expressions generated in equation (18) and (19) for $\widehat{E}$ and f, respectively. With loading condition (12), they can be rewritten:

$$\begin{aligned} \widehat{E}(\bar{\mathrm{F}}) = \varepsilon(\bar{\lambda}_1,\bar{\lambda}_2) = \Psi(\bar{I},\bar{J}) - (\Psi(\bar{I},\bar{J}) + \\ \bar{\lambda}_1\bar{\lambda}_2 \frac{\left(\frac{\bar{\lambda}_1}{\bar{\lambda}_2} + \frac{\bar{\lambda}_2}{\bar{\lambda}_1}\right)(4\Psi_{\bar{I}}^3 + 3\Psi_{\bar{I}}\Psi_{\bar{J}}^2) + 12\Psi_{\bar{I}}^2\Psi_{\bar{J}} + \Psi_{\bar{J}}^3}{4\Psi_{\bar{I}}^2 - \Psi_{\bar{J}}^2}) f_0 + \mathrm{O}(f_0^2) \end{aligned} \tag{20}$$

where $\Psi_{\bar{I}} = \partial\Psi(\bar{I},\bar{J})/\partial I$, $\Psi_{\bar{J}} = \partial\Psi(\bar{I},\bar{J})/\partial J$ with $\bar{I} = \overline{\lambda_1}^2 + \overline{\lambda_2}^2$, $\bar{J} = \overline{\lambda_1}\overline{\lambda_2}$.

$$f = \frac{16\Psi_{\bar{I}}^2(2\overline{\lambda}_2\Psi_{\bar{I}} + \overline{\lambda}_1\Psi_{\bar{J}})(2\overline{\lambda}_1\Psi_{\bar{I}} + \overline{\lambda}_2\Psi_{\bar{J}})}{\overline{\lambda}_1\overline{\lambda}_2(4\Psi_{\bar{I}}^2 - \Psi_{\bar{J}}^2)} f_0 + \mathrm{O}(f_0^2) \tag{21}$$

For hydrostatic loading, i.e. $\overline{\lambda_1} = \overline{\lambda_2} = \overline{\lambda}$:

$$f = \frac{16\Psi_{\bar{I}}^2}{(2\Psi_{\bar{I}} - \Psi_{\bar{J}})^2} f_0 + \mathrm{O}(f_0^2) \tag{22}$$

Finally, Focusing on equation (21), it is observed that the current porosity f (which, again, serves to measure the actual size of the cavity in the deformed configuration) becomes arbitrarily large at applied deformations approaching the curve $4\Psi_{\bar{I}}^2 - \Psi_{\bar{J}}^2 = 0$. This means that $4\Psi_{\bar{I}}^2 - \Psi_{\bar{J}}^2 = 0$ may actually correspond to the loci of critical deformations at which cavitation occurs. Of course, this is a somewhat naive interpretation of the result given that the asymptotic expression (21) ceases to be valid precisely at deformations satisfying $4\Psi_{\bar{I}}^2 - \Psi_{\bar{J}}^2 = 0$. Nevertheless, with the help of the full numerical solution for finite values of f_0, it can be verified that the condition $4\Psi_{\bar{I}}^2 - \Psi_{\bar{J}}^2 = 0$ does indeed define the loci of critical points in deformation space at which f suddenly begins to grow, and therefore at which cavitation takes place. In this regard, it is expedient to recognize from (22) that $2\Psi_{\bar{I}} - \Psi_{\bar{J}} = 0$, not $2\Psi_{\bar{I}} + \Psi_{\bar{J}} = 0$, is the relevant cavitation condition for the case of hydrostatic loading. Then, given that for physically reasonable stored-energy functions Ψ the curve $2\Psi_{\bar{I}} - \Psi_{\bar{J}} = 0$ and $2\Psi_{\bar{I}} + \Psi_{\bar{J}} = 0$ are not expected to cross, a simple continuity argument finally leads to the following criterion: inside a homogeneous, compressible, isotropic, hyperelastic material with stored-energy function $W(\mathrm{F}) = \Psi(I,J) = \Phi(I,J)$, cavitation will occur at a material point P whenever along a given loading path the deformation at that point first satisfies the condition:

$$2\frac{\partial\Psi}{\partial I}(I,J) - \frac{\partial\Psi}{\partial J}(I,J) = 0 \tag{23}$$

or
$$\frac{\frac{\partial \Phi}{\partial \lambda_1}(\lambda_1,\lambda_2)-\frac{\partial \Phi}{\partial \lambda_2}(\lambda_1,\lambda_2)}{\lambda_1-\lambda_2}=0\,; \tag{24}$$

For the special case $\lambda_1=\lambda_2=\lambda$, a formal calculation shows that (24) reduces to

$$\frac{\partial^2 \Phi}{\partial \lambda_1 \partial \lambda_1}(\lambda,\lambda)-\frac{\partial^2 \Phi}{\partial \lambda_2 \partial \lambda_2}(\lambda,\lambda)=0\,; \tag{25}$$

3.2 Remarks about Cavitation Criterion

First, it is noted that if the function Ψ is such that there is no pair of positive real numbers (I, J) that satisfies condition (23), cavitation does not occur. In the event that cavitation does occur, the set of (real and positive) points satisfying condition (25) defines a curve $C(I,J)=0$ in the (I, J)-deformation space. Similarly, (26) defines a curve $C(\lambda_1,\lambda_2)=0$ in (λ_1,λ_2)–deformation space. Henceforth, we refer to such curves as cavitation curves.

It is also important to remark from (23)-or, equivalently, from (24)-that cavitation does not occur within the context of classical linear elasticity. This expected result is a direct consequence of the fact that $2\partial\Psi/\partial I-\partial\Psi/\partial J\to 2\mu>0$ in the limit of small deformations (i.e., as $I\to 2$ and $J\to 1$), where μ is the shear modulus in the ground state.

Moreover, the stretch-based form (23) of the criterion is seen to be intimately related to the inequality: $(\partial\Phi/\partial\lambda_1-\partial\Phi/\partial\lambda_2)/(\lambda_1-\lambda_2)>0$, which is known to be a necessary condition for the positive definiteness of the incremental modulus tensor $L=\partial^2 W/\partial F^2$. In this regard, it is recognized that the critical deformations defined by condition (24) happen to correspond-rather interestingly-to deformations that are not incrementally stable.

In addition, condition (24) is seen to be reminiscent of the Baker-Ericksen (B-E) inequality: $(\lambda_1 \partial\Phi/\partial\lambda_1 - \lambda_2 \partial\Phi/\partial\lambda_2)/(\lambda_1 - \lambda_2) > 0$. In this connection, it is relevant to point out that while strong ellipticity (or strict rank-one convexity) implies the B-E inequality, it does not imply that condition (24) will not be satisfied at some critical finite deformation. In other words—in agreement with the findings of Ball [12]—strong ellipticity does not preclude cavitation.

The corresponding critical (principal) Cauchy stresses, t_1 and t_2, at which cavitation occurs are given by

$$t_1 = \frac{1}{\lambda_2^*}\frac{\partial\Phi}{\partial\lambda_1}(\lambda_1^*, \lambda_2^*) \quad \text{and} \quad t_2 = \frac{1}{\lambda_1^*}\frac{\partial\Phi}{\partial\lambda_2}(\lambda_1^*, \lambda_2^*) \tag{26}$$

where, for clarity of notation, λ_1^* and λ_2^* have been introduced to denote the critical stretches that satisfy condition (24). The set of points generated by evaluating expressions (25) at all pairs of critical stretches $(\lambda_1^*, \lambda_2^*)$ constitutes a cavitation curve $S(t_1, t_2) = 0$ in (t_1, t_2)–stress space.

The criterion (23)—or, equivalently, (24)—is a local criterion. However, it is known from the work of Ball [12] that cavitation depends in general on the global character of *W*. Thus, while (23) may be exact for some classes of materials, it cannot possibly be exact in general because of its local nature. In any case—as illustrated in the next section—the simple criterion (23) appears to constitute a remarkably accurate approximation for the onset of cavitation in large classes of compressible, isotropic, hyperelastic materials.

Finally, it should be emphasized that the above-proposed criterion is built around the problem of the sudden rapid growth of a vanishingly small cavity with initially circular cross section. It is plausible that different initial cavity shapes may lead to significantly different cavitation criteria. This important issue will be studied elsewhere, but here we note that the methods presented in this work are equally applicable to material systems with non-circular cavities.

4 Finite-Element Approach for 2D Problem

4.1 Mesh Geometry

The finite-element approach model of a cylindrical vacuous inhomogeneity, with initially circular cross section, in an infinite matrix phase is generated in commercial code ABAQUS of performed hyperelastic-mechanical analysis by 2D plane strain method. It is very difficult to generate the infinite matrix in ABAQUS, thus we generate the model of an infinitesimally cylindrical vacuous inhomogeneity, with initially circular cross section, in a finite matrix phase in the ABAQUS.

4.1.1 Shell Mesh for Hydrostatic Deformations

We develop a cirque structured mesh which we call shell mesh with initial porosity of 10^{-2} and 10^{-4} in ABAQUS CAE, and place 120 elements per layer in the circumferential direction (see Figure 3 (a)). In order to get the near square element size, we set up bias in the radial direction and the details of bias and element number are depend on the initial porosity. To apply the hydrostatic deformations, $\overline{\lambda_1} = \overline{\lambda_2} = \overline{\lambda}$, it is better to transfer the nodes on boundary into cylindrical coordinate system (axis z is perpendicular to the plane), so r-direction is 1-direction in the cylindrical coordinate system and it is very convenience to apply the hydrostatic loading by applying the displacement boundary condition in 1-direction (see Figure 3 (b)). Figure 4 shows the contour on the deformed and undeformed configuration from ABAQUS, i.e. compressible Neo-Hookean material at initial porosity $f_0 = 10^{-2}$ and compressibility ratio $\mu'/\mu = 10$ as an example.

4.1.2 Wedge Mesh for Hydrostatic Deformations

According to radially symmetric geometry and hydrostatic deformations, the above shell mesh model can be simplified to one layer mesh with hydrostatic

deformation, which we called wedge mesh (see Figure 5). The purpose of doing this is to cut computational cost.

The wedge mesh with $\theta = 3^o$, which is the same as the shell mesh, can also be easily generated in the ABAQUS CAE (see Figure 6(a)). We fix the bottom line in Y-direction and use command EQUATION to let the upper line deform in the radial direction. And we also apply the radial displacement loading condition on both point P1 and P2. We show the deformed and undeformed configuration from ABAQUS, i.e. compressible Neo-Hookean material at initial porosity $f_0 = 10^{-2}$ and compressibility ratio $\mu'/\mu = 10$ as an example (see Figure 6(b)).

4.1.3 Generally Non-symmetric Deformations Mesh

According to generally non-symmetric deformations, $\overline{\lambda_1} \neq \overline{\lambda_2}$, we cannot use wedge mesh to simulate cavitation phenomenon in hyperelastic solids under this kind of deformation. We just can simplify the model a cylindrical vacuous inhomogeneity, with initially circular cross section, in an infinite matrix phase, into the 2D model of an infinitesimal circle in a finite square. Since this model is symmetric, we just generate one quarter of the model.

We generate this generally non-symmetric deformations mesh in MATLAB, which we call rectangular mesh. From the hydrostatic deformations result, there will be a high stress concentration on the region near the void, thus we place more nodes and radially symmetric mesh in this region (see Figure 8). For the rest part, it is almost homogenous and we just place structured transition mesh in this area. During the analysis of hydrostatic deformations result, we also monitor the size of the elements. The reason of this step is that quadrilateral rectangular elements perform best if their shape is approximately square. We generate approximate square element near the void in wedge mesh. When the cavitation occurs, we find that the length of the element, l_1 which is in X-direction, is much less than the width of the element,

l_2 which is in Y-direction and the ratio is approximately: $l_2/l_1 \doteq 50$ (see Figure 7). To get the more accurate result when cavitation occurs, we generate a rectangular element with $l_2/l_1 = 2$ in the initial.

The procedure of making this mesh is organized as following. For the radially symmetric mesh region, we generate rectangular elements with $l_2/l_1 = 2$ in the initial and place 30 elements on the edge of the circle, in order to keep the same $\theta = 3^o$ as above two meshes, and 30 layers of elements in this region as following (see Figure 8):

$$\begin{aligned} &\Delta r = r_{i+1} - r_i = 2r_{i+1} \bullet \theta \qquad i = 1 \to 30 \\ &r_{i+1} = \frac{r_i}{1 - 2\theta} \end{aligned} \tag{27}$$

where r_i is the radius of No. i layer and it starts from $r_1 = 1$. Because there are 30 elements on the edge of the circle, thus $\theta = 3^o$. For the transition mesh region (see Figure 8), which means changing the arc to the straight line, we use the following transition formula and place 15 layers of element in this region to generate the mesh:

$$\frac{\Delta a_i}{a} = \frac{\Delta l_i}{l} \quad \text{and} \quad \Delta l_{i+1} = \Delta l_i * \delta \qquad i = 1 \to 15 \tag{28}$$

where l is the total length from the arc to the end edge of square in the bottom line, a is the total length from the arc to the end edge of the square in an arbitrary line in the middle of the square, Δl_i is the increment of No. i layer in the bottom line and it starts from $\Delta l_1 = 2$ in the case of initial porosity $f_0 = 10^{-6}$, Δa_i is the related increment of No. i layer in the above arbitrary line in the middle of square, δ is the increment parameter of the Δl_i and we choose $\delta = 1.1$ in the case of initial porosity $f_0 = 10^{-6}$.

For different initial porosity, take the case of changing initial porosity $f_0 = 10^{-6}$ general loading mesh into initial porosity $f_0 = 10^{-7}$ general loading mesh as example (see Figure 9), we use following method to change the elements' size, but not increase the number of elements: For the first 5 layer elements, we don't change the size, because there is a high stress concentration in this region. For the left elements in the radially symmetric mesh region, we use following increment way to change the size of elements:

$$R_i = \frac{r_i^2}{2.6} + r_i - 1.3 \times 1.1^{i-6} \tag{29}$$

where r_i is the radius of No. *i* layer in the mesh of initial porosity $f_0 = 10^{-6}$, R_i is the radius of No. *i* layer in the mesh of initial porosity $f_0 = 10^{-7}$. For the gradual mesh region, we still use the formula (28) to generate the mesh, but we choose the right δ for the mesh of initial porosity $f_0 = 10^{-7}$.

The detail of the loading condition in generally non-symmetric deformation will be discussed in the subsection 4.1.3.1.

4.1.3.1 Loading Condition

For convenience, we use the following formula to transfer the (λ_1, λ_2)–deformation space into the related (e_1, e_2)–deformation space:

$$\begin{aligned} e_1 &= \ln \lambda_1 \\ e_2 &= \ln \lambda_2 \end{aligned} \tag{30}$$

For the incompressible Neo-Hookean material, $J = \lambda_1 \lambda_2 = 1$, in the related (e_1, e_2)–deformation space, the material behavior is a solid straight line through the origin (see the solid line in the Figure 10) and we can see that there will be no cavitation for incompressible Neo-Hookean material in the 2D problem. For the compressible Neo-Hookean material, $J = \lambda_1 \lambda_2 > 1$, and the transformation (30), the

material behavior should be in the right side space from the above the incompressible Neo-Hookean material behavior and parallel with the incompressible Neo-Hookean material behavior (see the dash line in the Figure 10).

If we apply the loading condition along the line $e_2 = \tan\phi e_1$, (see the red line in the Figure 10), when this loading hit the compressible Neo-Hookean material behavior (see the dash line in Figure 10), there will occur cavitation for the compressible Neo-Hookean material. Thus there is a related point for the critical stretch in the (λ_1, λ_2)–deformation space. Thus we can apply the displacement loading condition as following:

$$\lambda_1 = \lambda_2^{\tan\phi} \quad \text{and} \quad \begin{matrix} u_1 = (\lambda_1 - 1) * l \\ u_2 = (\lambda_2 - 1) * l \end{matrix} \tag{31}$$

where ϕ is the loading angle, which is the angle in the related (e_1, e_2)–deformation space and l is the length of the square cell.

In the ABAQUS, we use the command AMPLITUDE at the time interval 0.1 (or maybe smaller in some special cases) to simulate this kind of displacement boundary condition. So there will be 11 interval points (even more in some special cases) in the loading and between every related 2 points ABAQUS use linear displacement boundary condition to get the approximate loading. From the Figure 10, we can see that all the material behavior is symmetric to the line $e_1 = e_2$, thus if we do the loading angle $\phi = -45^o \to 45^o$, we can get the entire (λ_1, λ_2)–deformation space.

Finally, We show the deformed and undeformed configuration from ABAQUS, i.e. compressible Neo-Hookean material at initial porosity $f_0 = 10^{-7}$ and compressibility ratio $\mu'/\mu = 10$ with loading angle $\theta = 35^o$ (see Figure 11 (a)) and $\theta = -15^o$ (see Figure 11 (b)) as examples.

4.2 ABAQUS Element Type

The elements used in the wedge mesh and rectangular mesh were solid (continuum) elements. The solid elements in ABAQUS are suitable for linear analysis and also for complex non-linear analyses involving hyperelastic and large deformations. There are a number of continuum elements available within the ABAQUS element library. A brief description of the attributes of the elements used for the cavitation of hyperelastic analysis is given below.

Quadrilateral elements were chosen over rectangular elements as the quadrilateral elements have a better convergence rate and sensitivity to mesh orientation in regular meshes is not an issue. Quadrilateral elements perform best if their shape is approximately rectangular or square. The elements become much less accurate when they are initially distorted.

The second order form of the quadrilateral elements was used as this provides higher accuracy than first order elements for 'smooth' problems that do not involve complex contact conditions or impact. Second order elements have more nodes per element than first order elements (i.e. they have a midsize node). They capture stress concentrations more effectively and are better for modeling geometric features.

Reduced integration is available for quadratic elements and was utilized in the cavitation of hyperelastic analysis. It uses a lower-order integration to form the element stiffness. Reduced integration reduced the running time of an analysis. Second order reduced integration elements generally yield more accurate results that the corresponding first order fully integrated elements.

A further element option is the hybrid element. Hybrid elements are intended mainly for use with incompressible and almost incompressible materials. For a near incompressible material a very small change in displacement produces extremely large changes in pressure. Therefore, a purely displacement-based solution is too sensitive to be useful numerically. This singular behavior is removed by treating the pressure stress as an independently interpolated basic solution variable, coupled to the

displacement. This independent interpolation of pressure stress is the basis of the hybrid elements. Hybrid elements have more internal variables than non-hybrid elements and this increases running time. Hybrid elements are recommended for hyperelastic materials.

For structural applications, the ABAQUS element library includes plane stress, plane strain and generalized plane strain elements. Plane stress elements can be used when the thickness of a body is small relative to its lateral (in-plane) dimensions. Modeling with this element generally applies to thin, flat bodies. In contrast, plane strain elements are generally used for modeling bodies that are very thick relative to their lateral dimensions. In these elements it is assumed that the strains in the loaded body are functions of the planar coordinates only and out-of-plane normal and shear strains are equal to zero. An alternative type of plane strain element is the generalized plane strain element.

In this case, the formulation places the model indicates that cavitation of hyperelastic solids is a highly non-linear problem and the geometry shows that there will be a high stress concentration near the void. Thus, if the edge mesh and general loading mesh use quadrilateral elements, they would have the ability to respond to Poisson's contractions and cavitation. It is assumed that the deformation of the model is independent of the axial position so the relative motion of the two planes causes a direct strain in the axial direction only. There are no transverse shear strains. Both plane strain and generalized plane strain elements have been considered in the analysis of cavitation of hyperelastic. Finally, we choose CPE8R as the element type for compressible material and CPE8RH as the element type for incompressible material.

4.3 Define Material in ABAQUS

We first introduce some definitions in ABAQUS: in ABAQUS, for simplicity, it define $\overline{\mathrm{F}} = J^{-1/3}\det(\mathrm{F})$ as the deformation gradient with the volume change

eliminated, thus the deviatoric stretch matrix (the left Cauchy-Green strain tensor) of $\overline{\mathrm{F}}$ as $\overline{\mathrm{B}}=\overline{\mathrm{F}}\bullet\overline{\mathrm{F}}^{\mathrm{T}}$ so that the related first train invariant is $\overline{I} = \mathrm{trace}\overline{\mathrm{B}}$.

For compressible hyperelastic material, ABAQUS already build the package in itself. For example, for compressible Neo-Hookean material:

$$U = C_{10}(\overline{I}_1 - 3) + \frac{1}{D_1}(J-1)^2 \tag{32}$$

We can use command HYPERELASTIC, NEO HOOKE and define the parameter C_{10} and D_1 in the next line to define the compressible Neo-Hookean like (32). For compressible Blatz-Ko material, ABAQUS use hyperfoam potential to define:

$$U = \sum_{i=1}^{N} \frac{2\mu_i}{\alpha_i^2}\left[\lambda_1^{\alpha_i} + \lambda_2^{\alpha_i} + \lambda_3^{\alpha_i} - 3 + \frac{1}{\beta_i}(J^{-\alpha_i\beta_i} - 1)\right] \tag{33}$$

We can use command HYPERFOAM and input the parameter i, μ_i, α_i, β_i in the next line to define the compressible Blatz-Ko like (35)

For the incompressible material, we can use subroutine HYPER with stored-energy function and related 15 derivatives, and program in FORTRAN to define the material.

5 Results and Discussion on 2D Problem

In this sequel, we make use of the finite-element approach put forward in Section 4 to explicitly determine and discuss the onset of cavitation in variety of compressible, isotropic, hyperelastic material. The objective is to gain more physical insight into the cavitation phenomenon in these hyperelastic solid, as well as to compare the FEM result with approximately analytical solution.

5.1 Compressible Neo-Hookean Material

Now we are in the position to discuss about the compressible Neo-Hookean material and use the following compressible Neo-Hookean material (see, e.g., Chapter 7.4 in [29]):

$$\Phi(\lambda_1,\lambda_2)=\frac{\mu}{2}[\frac{\lambda_1^2+\lambda_2^2+1}{(\lambda_1\lambda_2)^{2/3}}-3]+\frac{\mu'}{2}(\lambda_1\lambda_2-1)^2 \tag{34}$$

where $\mu>0$ and $\mu'>0$ are material parameters. The stored-energy function (34) is a generalization-capable to account for finite compressibility-of the standard incompressible Neo-Hookean material. Indeed, in the limit as the compressibility ratio $\mu'/\mu\to\infty$, (34) reduces identically to

$$\Phi(\lambda_1,\lambda_2)=\frac{\mu}{2}(\lambda_1^2+\lambda_2^2-2) \tag{35}$$

together with the incompressibility constraint $J=\lambda_1\lambda_2=1$.

Ball [13] showed that radially symmetric cavitation does not occur in incompressible Neo-Hookean materials (35) subject to hydrostatic pressure. He also examined the occurrence of cavitation in a particular class of compressible Neo-Hookean materials, but his results do not apply to (34). Accordingly, in order to work out the numerical cativitation for compressible Neo-Hookean material and compare with the approximately analytical solution in this case, we carried out a finite element (FEM) simulation of the problem using the commercial code ABAQUS.

5.1.1 Result and Discussion on Hydrostatic Deformations

The structure of this section is organized as following. In subsection 5.1.1.1, we will check finite-element approach model by analytical solution on incompressible Neo-Hookean material, including shell mesh and wedge mesh. Then, in subsection 5.1.1.2, we show the result and discussion on numerical cavitation criterion for compressible Neo-Hookean material and how small the void represents to $f_0 \to 0+$ by hydrostatic deformations result.

5.1.1.1 Check Finite-Element Approach Model.

With regard to porous elastomers subjected to finite deformations, there are very few exact results available. For the special case of hydrostatic loading, Hashin [32] obtained the exact equilibrium solution by making use of the idea of the composite spheres assemblage. Following that work, it is straightforward to show that the exact stored-energy function for the in-plane hydrostatic deformation of a porous rubber with incompressible isotropic matrix $W(\mathrm{F}) = \Phi(\lambda_1, \lambda_2)$ may be written as:

$$\widetilde{W}^I = 2\int_{\sqrt{f_0}}^{1} \Phi(\lambda, \lambda^{-1}) R \mathrm{d}R \tag{36}$$

where

$$\lambda = \sqrt{1 + \frac{\overline{\lambda}^2 - 1}{R^2}} \tag{37}$$

In general, the integral in (36) cannot be computed analytically; however, for the particular case of a porous elastomer with incompressible Neo-Hookean matrix phase (35), Thus the exact stored-energy function may be expressed as

$$\Phi = \frac{\mu}{2}(\overline{\lambda}^2 - 1)\left[\ln\left(\frac{\overline{\lambda}^2 + f_0 - 1}{f_0}\right) - \ln(\overline{\lambda}^2)\right] \tag{38}$$

According to (26), we can see the corresponding Cauchy stress in deformation can be written as:

$$\frac{t}{\mu} = \frac{1}{2\bar{\lambda}\mu}\frac{\partial \Phi}{\partial \bar{\lambda}}$$
$$= \frac{1}{2}\left\{\left[\ln\left(\frac{\bar{\lambda}^2 + f_0 - 1}{f_0}\right) - \ln(\bar{\lambda}^2)\right] + (\bar{\lambda}^2 - 1)\left[\frac{1}{\bar{\lambda}^2 + f_0 - 1} - \frac{1}{\bar{\lambda}^2}\right]\right\} \tag{39}$$

For incompressible matrix phase materials, a simple conservation of mass argument (for the matrix phase) allows for the determination of the evolution of the porosity f as a function of deformation. The result is:

$$f = 1 - \frac{1 - f_0}{\bar{J}} = 1 - \frac{1 - f_0}{\bar{\lambda}^2} \tag{40}$$

We develop the shell mesh and edge mesh on the initial porosity 10^{-2} and 10^{-4} with the same geometry, $\theta = 3^o$. We use UHYPER to define the incompressible Neo-Hookean material (35) and apply the hydrostatic deformations. Figure 12 shows the good agreement on current porosity check among the FEM shell mesh result, FEM wedge mesh result and analytical solution (40). To check the Cauchy stress, we output the CENTROID stress from ABAQUS, which is stress from the center of element and more accurate. Figure 13 shows the good agreement on Cauchy stress check among the FEM shell mesh result, FEM wedge mesh result and analytical solution (40). Thus we can see that our FEM models with material definition and loading condition are right.

For compressible Neo-Hookean material, we just need to change the material and compressible Neo-Hookean material is the package in ABAQUS, thus if our models work for incompressible Neo-Hookean material, it will also work for compressible Neo-Hookean material. To study hydrostatic deformation, we prefer to use wedge mesh, because it will cut the computation cost.

5.1.1.2 Result and Discussion on Hydrostatic Deformation

Now we are in the position to use wedge mesh to study the compressible Neo-Hookean material under hydrostatic deformations. It is very difficult to generate infinitesimally small void in ABAUQS, thus the first problem we need to solve is to examine how small the void can simulate an "infinitesimal" circle and represent $f_0 \to 0+$. Specifically, we considered a cylindrical shell with different small initial porosity of $f_0 = 10^{-4}, 10^{-5}, 10^{-6}, 10^{-7}, 10^{-8}, 10^{-9}$ subjected to radially symmetric deformation $\lambda_1 = \lambda_2 = \lambda$, on its boundary using the wedge mesh, and monitored the increase in porosity and the resulting surface tractions. Because it is the hydrostatic loading condition, we expect the inside and outside edge of the circle shell can remain arc during the deformation. However it is very difficult to keep that, especially in smaller initial porosity, because the computer use small line to get the approximate arc and we cannot place too many nodes to get a good approximate arc. But for the cases of $f_0 = 10^{-4}, 10^{-5}, 10^{-6}, 10^{-7}, 10^{-8}, 10^{-9}$, we use two ways to calculate the current porosity: one is add all volume of the elements together, the other is assume the inside and outside edge of the circle shell can remain circle and use the ratio of area of void over that of total circle. From the result, we find the difference is not too much, but if we do the case of $f_0 = 10^{-11}$, the difference will be too large. That is why we only do cases of $f_0 = 10^{-4}, 10^{-5}, 10^{-6}, 10^{-7}, 10^{-8}, 10^{-9}$, but the result also shows that it is small enough to represent $f_0 \to 0+$.

For all the examined cases, we print out the relationship between current porosity f and principle stretch λ (see Figure 14) and the relationship between porosity ratio f/f_0 and principle stretch λ (see Figure 15). We can see that if the initial porosity is smaller than $f_0 = 10^{-6}$, the deformations of current porosity f and porosity ratio f/f_0 are very close and similar. From above result we can see that the

initial porosity $f_0 = 10^{-7}$ is a sufficiently small initial porosity that is representative of $f_0 \to 0+$.

Because cavitation is detected as the phenomenon of the sudden growth of the void, we need to work out the numerical caviation criterion for compressible Neo-Hookean material to signal the cavitation. We monitor the increase in the current porosity of above cases. For all the examined cases, during deformation we find that the current porosity f remained in the order of initial porosity up to some critical value of the applied stretch after which f increased very rapidly with increasing deformation (see Figure 14 and 15 for the representative results). These numerically exact results thus indicate that compressible Neo-Hookean materials of the form (34) do cavitate. Thus we work out the relationship between the initial porosity f_0 and the critical principle stretch λ_{crit}, where the critical principle stretch λ_{crit}, for definiteness, is the principle stretch whenever the current porosity reached the critical value one-order-of-magnitude increase $f_{crit} = 10 \times f_0$, two-orders-of-magnitude increase $f_{crit} = 100 \times f_0$ and three-orders-of-magnitude increase $f_{crit} = 1000 \times f_0$ (see Figure 16). To get results based on these three criterions, we use Cubic Spline Curve Interpolation and program in MATLAB to gain the data. Based on critical principle stretch λ_{crit}, we also work out the relationship between the initial porosity f_0 and the corresponding critical Cauchy stress t_{crit}/μ, where the corresponding critical Cauchy stress t_{crit}/μ, for definiteness, is generated by $t_{crit}/\mu = 1/(\mu\lambda_{crit})\partial\Phi(\lambda_{crit}, \lambda_{crit})/\partial\lambda_1$ (see Figure 17).

From the figure 16 and 17, we can see that the difference on both principle stretch λ_{crit} and corresponding Cauchy stress t_{crit}/μ between values of one-order-of-magnitude increase $f_{crit} = 10 \times f_0$ and two-orders-of-magnitude

increase $f_{crit} = 100 \times f_0$ is very large, however the difference between values of two-orders-of-magnitude increase $f_{crit} = 100 \times f_0$ and three-orders-of-magnitude increase $f_{crit} = 1000 \times f_0$ is almost zero, especially in smaller initial porosity. Thus we can take this two-orders-of-magnitude increase $f_{crit} = 100 \times f_0$ to signal the onset of cavitation. They also show that 10^{-7} is small enough to represent $f_0 \to 0+$, because the difference in principle stretch λ_{crit} and corresponding critical Cauchy stress t_{crit}/μ among the cases of $10^{-6}, 10^{-7}, 10^{-8}, 10^{-9}$ is very small.

It should be noted, however, that using different criteria such as one-order-of-magnitude increase $f_{crit} = 10 \times f_0$ or three-orders-of-magnitude increase $f_{crit} = 1000 \times f_0$ may lead to somewhat different values for the critical stretch λ_{crit} at which cavitation occurs, but the qualitative character of the results remains of course unchanged.

From above discussion, The FEM results in the following section generated in this manner (i.e., using $f_{crit} = 100 \times f_0$ as cavitation criterion) for the critical stretch λ_{crit} and corresponding critical Cauchy stress $t_{crit}/\mu = 1/(\mu\lambda_{crit})\partial\Phi(\lambda_{crit}, \lambda_{crit})/\partial\lambda_1$ at which cavitation occurs on the initial porosity $f_0 = 10^{-7}$.

To study the material parameter compressibility ratio μ'/μ, we develop the models of compressibility ratios μ'/μ in the range of $0.1 \le \mu'/\mu \le 100$ on initial porosity $f_0 = 10^{-7}$ subject to hydrostatic deformations. First we work out relationships of current porosity f (see Figure 18), porosity ratio f/f_0 (see Figure 19), corresponding Cauchy stress t/μ (see Figure 20) as a function of principle stretch λ for the representative cases of $\mu'/\mu = 1, 10, 50$. The result shows that in deformation space with decrease in compressibility ratio μ'/μ which means the

material is more compressible, the compressible Neo-Hookean material is more stable means cavitation occurs at large deformations. In stress space, with increase in compressibility ratio μ'/μ, corresponding Cauchy stress t/μ increase which means material is more stable in incompressibility.

We also apply the approximately analytical cavitation criterion (25) for hydrostatic deformation and the numerical cavitation criterion and compare the result together on the deformation space and stress space in hydrostatic deformation.

Now we use the approximately analytical cavitation criterion (25) to work the deformation space for compressible Neo-Hookean material (34) under hydrostatic deformations. There now follows the specialization of the cavitation criterion (25) to compressible Neo-Hookean materials of the form (34):

$$C(\lambda,\frac{\mu'}{\mu}) = 1 + 5\lambda^2 + 3(\lambda^{10/3} - \lambda^{16/3})\frac{\mu'}{\mu} = 0 \tag{41}$$

Note that this condition depends on the parameters μ and μ' only through the ratio μ'/μ, which, again, serves to measure the compressibility of the material; the larger the value of μ'/μ, the smaller the compressibility of the Neo-Hookean solid (34).

Figure 21 illustrates various results for the onset of cavitation in compressible Neo-Hookean materials (34), as determined by condition (41) and by finite element simulations. It provides results for the critical stretch λ_{crit} at which cavitation ensues under hydrostatic loading $\lambda_1 = \lambda_2 = \lambda$, as a function of the compressibility ratio μ'/μ. In line with the accuracy of the criterion (25) for the two preceding classes of materials, Figure 21 shows that the critical stretch λ_{crit} determined from (34) is in very good agreement with the FEM calculations for all values of the compressibility ratio μ'/μ. Moreover, note from this figure that $\lambda_{crit} \geq 1$ and that it decreases

monotonically with increasing μ'/μ. That is, compressible Neo-Hookean materials (34) are more stable in deformation space—in the sense that cavitation occurs at larger deformations—when they are more compressible. In this regard, it is straightforward to verify from (41) that $\lambda_{crit} \to \infty$ in the limit as $\mu'/\mu \to 0$, so that cavitation does not occur in this extreme case. This asymptotic behavior is also exhibited by the FEM results. On the other hand, in the limit as $\mu'/\mu \to \infty$, $\lambda_{crit} \to 1$ according to the approximate criterion (41) as well as to the FEM calculations. This limiting behavior indicates that cavitation may take place at zero applied strain in compressible Neo-Hookean solids (34) when they are taken to be incompressible. In order to corroborate that cavitation does indeed take place in this limit, however, we need to check whether the corresponding critical stress remains finite. The reason for this extra step is that incompressible solids behave as rigid materials when subjected to non-isochoric deformations, such as hydrostatic loading. As a result, the critical stretch reduces trivially to $\lambda_{crit} = 1$ and the relevant question is then whether the corresponding critical hydrostatic stress is of finite value. In the event that the critical pressure is not finite, cavitation does not, of course, occur. The critical stresses are discussed further below, but here we anticipate that, according to the criterion (41), they do remain finite in the limit as $\mu'/\mu \to \infty$. The FEM simulations also appear to support that the stresses do remain finite in this limit. Further comment on this controversial result is deferred to the discussion of Figure 22.

We now turn to examine the onset of cavitation in compressible Neo-Hookean materials (34) in stress space. To this end, it is expedient first to recognize that the cavitation condition (25) in deformation space takes the explicit form

$$S\left(\frac{t}{\mu},\frac{\mu'}{\mu}\right)=1+\frac{2^{3/2}}{(\frac{t}{\mu})^{3/2}}+\frac{2^{7/2}}{(\frac{t}{\mu})^{3/2}}+3\left[\frac{2^{5/2}}{(\frac{t}{\mu})^{5/2}}-\frac{2^{4}}{(\frac{t}{\mu})^{4}}\right]\frac{\mu'}{\mu}=0 \qquad (42)$$

in stress space. Note also that depends only on compressibility ratio μ'/μ,

Figure 22 presents results for the critical Cauchy stress $t_{crit}/\mu = 1/(\mu\lambda_{crit})\partial\Phi(\lambda_{crit},\lambda_{crit})/\partial\lambda_1$ at which cavitation ensues in compressible Neo-Hookean materials (34) under hydrostatic loading $\lambda_1 = \lambda_2 = \lambda$. The results, which correspond to the approximate criterion (42) (solid line) and to finite element calculations (points), are shown as a function of the compressibility ratio μ'/μ. It is interesting to notice that the quantitative agreement between the approximate stress criterion (42) and the FEM results is not as good as that exhibited in deformation space (see Figure 21). This is because small discrepancies in deformation space get amplified by a factor of μ'/μ in stress space. Another interesting observation from Figure 22 is that t_{crit}/μ is a monotonically increasing function of the compressibility ratio μ'/μ. Physically, this means that compressible Neo-Hookean materials (34) are more stable in stress space—in the sense that cavitation occurs at larger stresses—when they are more incompressible, which is in direct contrast to the behavior exhibited in deformation space (see Figure 21). In particular, note that $t_{crit} \to 0$ as $\mu'/\mu \to 0$, according to both, the criterion (42) and the FEM calculations. On the other hand, in the limit as $\mu'/\mu \to \infty$, condition (42) renders $t_{crit} = 2\mu$, while the FEM results lead approximately to $t_{crit} = 2.6\mu$. Thus, in the case when the material is most compressible ($\mu'/\mu = 0$) cavitation does not occur. By contrast, in the case when the material is taken to be incompressible ($\mu'/\mu = \infty$), cavitation does occur. This latter result is in contradiction with the exact result of Ball [12] for incompressible Neo-Hookean materials (35), which are known not to undergo radially symmetric cavitation under hydrostatic pressure. An explanation for this discrepancy is quite simply that, in the strongly nonlinear limit of incompressibility, the approximate criterion (42) is inaccurate and the FEM results for $f_0 = 10^{-7}$ are not representative of those for $f_0 = 0+$. While possible, this explanation is not supported

by our parametric FEM study of the results for decreasing values of f_0. A more interesting explanation—which is supported by our parametric study—is that computing the onset of cavitation first and then taking the limit of incompressibility (as done here) leads to different results than taking the limit of incompressibility first and then computing the onset of cavitation (as done by Ball [12]). In other words, the limits of dilute porosity ($f_0 \to 0+$) and incompressibility ($\mu'/\mu \to \infty$) do not commute in general. From a theoretical perspective, this is a very interesting result worth of further study by analytical means in order to prove or disprove its verity. Moreover, from a practical point of view, it is also worth remarking that initial porosities in the order of $f_0 = 10^{-7}$ (and smaller) are likely to be present in the form of defects in real materials. Thus, the proposed criterion (41)—which, again, is in agreement with the numerically exact FEM results for small initial porosities in the order of $f_0 = 10^{-7}$—can be used as an efficient tool to estimate the critical loads at which defects of realistically small size may rapidly grow to finite size in incompressible Neo-Hookean materials.

5.1.2 Result and Discussion on Generally Non-symmetric Deformations

The structure of this section is organized as following. In subsection 5.1.2.1, we will check finite-element approach model by repeating hydrostatic deformation result. Then, in subsection 5.1.2.2, we show the result and discussion on numerical cavitation criterion for compressible Neo-Hookean material and how small the void represents to $f_0 \to 0+$ by hydrostatic deformations result.

5.1.2.1 Check Finite-Element Approach Model.

As discussed above, $f_0 = 10^{-7}$ is a sufficiently small initial porosity that is representative of $f_0 \to 0+$, thus we working on generally non-symmetric

deformation on cases of $f_0 = 10^{-7}$. To check the generally non-symmetric deformations mesh, we do hydrostatic deformations on compressible Neo-Hookean material with compressibility ratio $\mu'/\mu = 10$ and check whether this result can repeat the previous one.

Figure 23 presents the result on the current porosity check and Figure 24 presents the results on the corresponding Cauchy stress check. There are good agreements in both procedures. Thus we say our generally non-symmetric mesh is safe.

5.1.2.2 Result and Discussion on Generally Non-symmetric Deformations

To study generally non-symmetric deformations, we consider to generally non-symmetric deformations mesh with compressibility ratio $\mu'/\mu = 1, 10, 50$. First to solve the problem how to calculate the volume of inside void, from the deformed shape, it is very close to eclipse, thus we use eclipse's volume to get the approximate volume of the inside void in the deformation.

There now follows the specialization of the cavitation criterion (26) to compressible Neo-Hookean materials of the form (34):

$$C(\lambda_1, \lambda_2) = 1 + \lambda_1^2 + \lambda_2^2 + 3\lambda_1\lambda_2 + 3[(\lambda_1\lambda_2)^{5/3} - (\lambda_1\lambda_2)^{8/3})\frac{\mu'}{\mu} = 0 \qquad (43)$$

Note that this condition depends on the parameters μ and μ' only through the ratio μ'/μ , which, again, serves to measure the compressibility of the material; the larger the value of μ'/μ , the smaller the compressibility of the Neo-Hookean solid (34).

For generally non-symmetric deformation, Figure 25 shows that cavitation curves in (λ_1, λ_2) –deformation space for $\mu'/\mu = 1, 10, 50$ and cavitation occurs only

for volume-increasing deformations (i.e., $J=\lambda_1\lambda_2>1$), as it may be physically expected. Moreover, this figure shows that cavitation is more prone to occur along deformation paths with larger triaxialities, as it may also be physically expected. In addition, similar to the results presented in Figure 25 for the special case $\lambda_1=\lambda_2$, Figure 25 illustrates that decreasing the compressibility ratio μ'/μ consistently improves the stability of the material—in the sense that cavitation occurs at larger deformations—for all applied deformations. In this regard, it is appropriate to remark from (43) that, irrespectively of the applied stretches λ_1 and λ_2, cavitation does not occur in the limit as $\mu'/\mu\to 0$. On the other hand, the cavitation curve approaches the isochoric curve:

$$C(\lambda_1,\lambda_2)=\lambda_1\lambda_2-1=0 \qquad \text{as} \qquad \mu'/\mu\to\infty \tag{44}$$

Again, this is a direct consequence of the fact that as $\mu'/\mu\to\infty$, the material becomes rigid for non-isochoric deformations. In order to conclude whether cavitation takes place or not in this degenerate case needs to be investigated in stress space.

Now we are in the position to examine the onset of cavitation in compressible Neo-Hookean materials (34) in stress space. To this end, it is expedient first to recognize that the cavitation condition (43) in (λ_1,λ_2)–deformation space takes the explicit form

$$S\left(\frac{t_1}{\mu},\frac{t_2}{\mu}\right)=1+\frac{(\frac{t_1}{\mu}+\frac{t_2}{\mu})^{3/2}}{(\frac{t_1t_2}{\mu^2})^{3/2}}+\frac{(\frac{t_1}{\mu}+\frac{t_2}{\mu})^{7/2}}{(\frac{t_1t_2}{\mu^2})^{5/2}}+$$

$$3\left[\frac{(\frac{t_1}{\mu}+\frac{t_2}{\mu})^{5/2}}{(\frac{t_1t_2}{\mu^2})^{5/2}}-\frac{(\frac{t_1}{\mu}+\frac{t_2}{\mu})^{4}}{(\frac{t_1t_2}{\mu^2})^{4}}\right]\frac{\mu'}{\mu}=0 \tag{45}$$

in $(t_1/\mu, t_2/\mu)$ –stress space. Here, it is recalled that t_1 and t_2 stand for the principal Cauchy stresses, as given by expressions (28), where λ_1^*, λ_2^* are to denote the critical stretches that satisfy condition (27) and numerical cavitation criterion. Note also that relation (45)—much like (44)—depends on the parameters μ and μ' only through the compressibility ratio μ'/μ.

We conclude this subsection with the discussion of Figure 26, which shows cavitation curves in $(t_1/\mu, t_2/\mu)$ –stress space for general loading conditions for values of $\mu'/\mu = 1, 10, 50, \infty$, as determined by condition (45). It is interesting to remark from this figure that cavitation occurs only in the first quadrant, where both components of the stress are tensile $(t_1/\mu \geq 0, t_2/\mu \geq 0)$. This is in contrast to the corresponding results in deformation space (see Figure 25) where cavitation may occur even when one of the principal stretches is compressive, namely, when either $\lambda_1 \leq 1$ or $\lambda_2 \leq 1$. Akin to the results in deformation space, Figure 26 also illustrates that cavitation is more prone to occur along loading paths with larger ratios of dilatational to distortional stress, as expected on physical grounds. Finally, similar to the results for the special case of hydrostatic loading displayed in Figure 26, it is worth remarking that compressible Neo-Hookean materials (34) improve their stability in stress space—in the sense that cavitation takes place at larger stresses—with decreasing compressibility; note in particular that no cavitation takes place for $\mu'/\mu = 0$ and for $\mu'/\mu = \infty$ that cavitation occurs at :

$$S(t_1/\mu, t_2/\mu) = (t_1/\mu - 1)(t_2/\mu - 1) - 1 = 0 \tag{46}$$

Interestingly, this behavior is in direct contrast with the corresponding results in deformation space (see Figure 25) where decreasing compressibility leads to smaller critical stretches at which cavitation occurs.

5.2 Blatz-Ko Material

Another important class of compressible isotropic solids (see, e.g., Section II.C in [33] and [34]) are those with stored-energy function

$$\Phi(\lambda_1,\lambda_2)=\frac{\mu}{k}(\lambda_1^{-k}+\lambda_2^{-k}-2+k(\lambda_1\lambda_2-1)) \tag{47}$$

where $\mu>0$ and $k>0$ are material constants. When $k=2$, (50) reduces to the well-known Blatz-Ko material-a phenomenological model for foam rubber [35].

For hydrostatic deformation, Horgan and Abeyaratne [17] determined the exact value for the critical stretch λ_{crit} at which radially symmetric cavitation occurs in a Blatz-Ko material ($k=2$). The result, which is independent of μ, reads as

$$\lambda_{crit}=1.25954 \tag{48}$$

We develop hydrostatic model by edge mesh on cases of $f_0=10^{-4},10^{-5},10^{-6},10^{-7}$. The result presented in Figure 27 shows that Blatz-Ko material behavior likes Neo-Hookean material: the current porosity f remained in the order of initial porosity up to some critical value of the applied stretch after which f increased very rapidly with increasing deformation (see Figure 27). We also calculate the critical principle stretch λ_{crit} for all examined cases based on all three numerical cavitation criterions mentioned before and find the critical principle stretch λ_{crit} of cases of $f_0=10^{-7}$ based on two-orders-of-magnitude increase $f_{crit}=100\times f_0$ and three-orders-of-magnitude increase $f_{crit}=1000\times f_0$ is the most close to analytical result:

$$\lambda_{crit}=\begin{cases}1.26009 & f_{crit}=100\times f_0\\ 1.26010 & f_{crit}=1000\times f_0\end{cases} \tag{49}$$

When we want to apply hydrostatic deformations on generally non-symmetric deformation mesh, it doesn't work when cavitation occurs. The reason of this phenomenon is the surface instability. The surface instability of the voids is a relevant constraint only for periodic microstructures, since it signals—at finite macroscopic strains—the onset of local instabilities at the unit cell level, instabilities which are detected by the more accurate FEM-based calculations. For random microstructures, surface instability of the voids exists even for infinitesimally small macroscopic strains, due to strain concentration in the surface of the smallest pores.

6 Finite-Element Approach for 3D Problem

The finite-element approach model of vacuous inhomogeneity is infinitesimally small spherical void in the center of a large cube phase is also generated in ABAQUS of performed hyperelastic-mechanical analysis by 3D plane stress method. According to symmetric geometry, we just generate one eighth of the whole model to analyze.

We develop the mesh of this model with element type C3D8, 3D plane stress with 8 nodes per element which located in the vertex, in MATLAB. The procedure of making this mesh is organized as following:

First of all, we develop one layer spherical mesh with nearly cubic elements and nearly square cross-section. As we discuss in section 3, when cavitation occurs, the length in radial direction l_2 is much larger than those l_1 in other two directions, thus we generate the cubic element with initial length ratio $l_2/l_1 \doteq 2$ (see Figure 28) is the same as 2D mesh. We also place 30 elements on the each arc. The difficulty to generate this one layer spherical mesh is to make the region A, B and C symmetric to the vector (1, 1, 1) and the elements should be distributed even both on the edge and inside (see Figure 28). As we know, (x, y, z) in spherical coordinate system is

$$\begin{aligned} x &= r\cos\varphi\cos\phi \\ y &= r\cos\varphi\sin\phi \\ z &= r\sin\varphi \end{aligned} \tag{50}$$

Because the nodes of the elements on the 2 spherical surface and in order to meet the requirement initial length ratio $l_2/l_1 \doteq 2$, we can use following formula

$$r_{i+1} = \frac{r_i}{1-2\theta} \qquad \theta = \pi/60 \tag{51}$$

easily to control the parameter r of all nodes on two spherical surface. Now our work turns to determine the parameter φ and ϕ so that we can make the region A, B and C symmetric to the vector (1, 1, 1) and the elements distributed even both on

the edge and inside. Our idea is to make the good mesh on three surface of the cube at first (see Figure 29 (a)) and then mapping elements on these three surface of cube back to the spherical surface. If we place symmetric mesh on these three surface of cube symmetric according to vertex V (L, L, L), thus we can get symmetric mesh on the region A, B and C of the spherical surface symmetric to the vector (1, 1, 1) after mapping. In order to get the distributed even nodes both on the edge and inside, we first place the distributed even nodes on the edge. We take the mesh on surface x=L for example. We place the nodes like following way:

$$z_{x=L} = L\tan(\theta * (i-1)) \qquad \theta = \pi / 60 \tag{52}$$

where i is the place number of the nodes in z-direction. Because there are 30 elements on the arc, there are 15 elements on the line x=L, y=0 and there are 16 nodes on this line which means $i = 1 \to 16$. On the line x=L, z=0, we do the similar way:

$$y_{x=L} = L\tan(\theta * (j-1)) \qquad \theta = \pi / 60 \tag{53}$$

where j is the place number of the nodes in y-direction and $j = 1 \to 16$. Based on these nodes, we make straight line from each node to get the perfect rectangular elements on the surface x=L (see Figure 29 (a)) and we can see that the coordinates of place number (i, j) on the surface x=L is:

$$\begin{aligned} x_{x=L} &= L \\ z_{x=L} &= L\tan(\theta * (i-1)) \\ y_{x=L} &= L\tan(\theta * (j-1)) \end{aligned} \tag{54}$$

Then we do the same thing on surface y=L and z=L. Finally we get the symmetric mesh on these three surfaces of cube symmetric according to vertex V (L, L, L) and distributed even mesh (see Figure 29(a)). Now we are in the position to mapping back to the spherical surface. We take mapping of one node N on the surface x=L for example (see Figure 29 (b)). Our work is to mapping the node N on the surface x=L back to the node N' on the spherical. What we need to do is determine the angles

φ and ϕ because parameter r can be easily determined by (51), otherwise we also make the point N, $N^{'}$ and original point O in the line so that it is very easy to determine the angles φ and ϕ of $N^{'}$ by the angles φ and ϕ of N because they are the same. The procedure is following and takes N for example (see Figure 29 (b)):

$$\begin{aligned} \phi &= \arcsin\left(\frac{y_{x=L}}{\sqrt{x_{x=L}^2 + y_{x=L}^2}}\right) \\ \varphi &= \arcsin\left(\frac{z_{x=L}}{\sqrt{x_{x=L}^2 + y_{x=L}^2 + z_{x=L}^2}}\right) \end{aligned} \tag{55}$$

We do the similar way on the other two surface and finally get symmetric spherical one layer mesh on the region A, B and C of the spherical surface symmetric to the vector (1, 1, 1) and distributed even mesh (see Figure 28).

From 2D result, we know that there is high stress concentration in the region near the void, thus we place the radially symmetric mesh on that region. We use formula (51) to determine the radius of 5 layers like the above one layer spherical mesh (see Figure 30 (a)). In transition region, we use following formula to determine the radius in the edge:

$$r_{i+1} = \frac{r_{Ini}}{(1-2\theta)^i} * 1.05^{i-1} \tag{56}$$

where r_{Ini} is the last radius of the radially symmetric mesh, i is the layer number (see Figure 30 (b)). For the nodes inside, in transition region, they are not on the spherical surface. Taking nodes mapping from surface x=L for example, we use following way to determine the location of nodes inside:

$$
\begin{aligned}
&\Delta l = L - r_i \\
&OR = \sqrt{x_i^2 + y_i^2 + z_i^2} \\
&NR = \sqrt{x_{i+1}^2 + y_{i+1}^2 + z_{i+1}^2} \\
&DR = L / \cos(\phi) / cos(\varphi) - OR \\
&\frac{r_{i+1} - r_i}{\Delta l} = \frac{NR - OR}{DR}
\end{aligned}
\tag{57}
$$

where r_i and r_{i+1} are the radius on the edge of layer i and $i+1$, (x_i, y_i, z_i) and $(x_{i+1}, y_{i+1}, z_{i+1})$ are the coordinates of the nodes inside of layer i and $i+1$. The number i depends on the initial porosity. We also do the similar way on the other nodes. Finally we get the good 3D mesh with element type C3D8 (see Figure 30 (b)). The way to define the material is the same as what we do in 2D problem.

The figure 31 represents the stress contour on the case of initial porosity $f_0 = 10^{-4}$ and compressibility ratio $\mu'/\mu = 10$.

7 Results and Discussion on 3D Problem

In this sequel, we make use of the finite-element approach put forward in Section 6 to explicitly determine and discuss the onset of cavitation in variety of compressible, isotropic, hyperelastic material under hydrostatic deformation.

7.1 Compressible Neo-Hookean Material in 3D Problem

Now we turn to discuss about the compressible Neo-Hookean material in 3D problem and use the following compressible Neo-Hookean material (see, e.g., Chapter 7.4 in [29]):

$$\Phi(\lambda_1,\lambda_2)=\frac{\mu}{2}[\frac{\lambda_1^2+\lambda_2^2+\lambda_3^2}{(\lambda_1\lambda_2\lambda_3)^{2/3}}-3]+\frac{\mu'}{2}(\lambda_1\lambda_2\lambda_3-1)^2 \tag{58}$$

where $\mu>0$ and $\mu'>0$ are material parameters. The stored-energy function (58) is a generalization-capable to account for finite compressibility of the standard incompressible Neo-Hookean material. Indeed, in the limit as the compressibility ratio $\mu'/\mu\to\infty$, (58) reduces identically to

$$\Phi(\lambda_1,\lambda_2)=\frac{\mu}{2}(\lambda_1^2+\lambda_2^2+\lambda_3^2-3) \tag{59}$$

together with the incompressibility constraint $J=\lambda_1\lambda_2\lambda_3=1$.

We carried out a finite element (FEM) simulation of the problem using the commercial code ABAQUS.

7.2 Check Finite-Element Approach Model.

The same as 2D problem, we also use incompressible Neo-Hookean material (59) to check our 3D model.

There is only analytical solution on current porosity check. For incompressible matrix phase materials, a simple conservation of mass argument (for the matrix phase)

allows for the determination of the evolution of the porosity f as a function of deformation. The result in 3D problem is:

$$f = 1 - \frac{1 - f_0}{\overline{J}} = 1 - \frac{1 - f_0}{\overline{\lambda}^3} \tag{60}$$

We develop 3D mesh on the initial porosity 10^{-4}, use UHYPER to define the incompressible Neo-Hookean material (59) and apply the hydrostatic deformations. Figure 32 shows the good match on current porosity check between the FEM result and analytical solution (60), thus we can say that our 3D model is suitable to study the cavitation in 3D problem.

7.3 Result and Discussion

Following 2D problem, in 3D problem we also need to solve is to examine how small the void can simulate an "infinitesimal" spherical void and represent $f_0 \to 0+$ for the compressible Neo-Hookean material (58). Specifically, we considered 3D model with different small initial porosity of $f_0 = 10^{-4}, 10^{-5}, 10^{-6}, 10^{-7}, 10^{-8}, 10^{-9}$ subjected to hydrostatic deformations on its boundary and monitored the increase in porosity and the resulting surface tractions. Because it is the hydrostatic loading condition, we expect the spherical void can remain spherical surface during the deformation. However it is very difficult to keep that, especially in smaller initial porosity, because the computer use small line to get the approximate arc and we cannot place too many nodes to get a good approximate arc. But for the cases of $f_0 = 10^{-4}, 10^{-5}, 10^{-6}, 10^{-7}, 10^{-8}, 10^{-9}$, our expectation still works.

For all the examined cases, we print out the relationship between current porosity f and principle stretch λ (see Figure 33) and the relationship between porosity ratio f/f_0 and principle stretch λ (see Figure 34). These two figures also

show that during deformation the current porosity f remained in the order of initial porosity up to some critical value of the applied stretch after which f increased very rapidly with increasing deformation. We can see that if the initial porosity is smaller than $f_0 = 10^{-6}$, the deformations of current porosity f and especially of porosity ratio f/f_0 are very close and similar. From above result we can see that the initial porosity $f_0 = 10^{-7}$ is a sufficiently small initial porosity that is representative of $f_0 \to 0+$ for 3D problem.

We also use three critical value, $f_{crit} = 10 \times f_0$, $f_{crit} = 100 \times f_0$ and $f_{crit} = 1000 \times f_0$, to detect the cavitation as the phenomenon of the sudden growth of the void. Based on these three critical value, we work out critical principle stretch λ_{crit} (see Figure 35), corresponding critical Cauchy stress t_{crit}/μ (see Figure 36) according to initial porosity f_0.

From the figure 35 and 36, we find the difference between critical values from $f_{crit} = 100 \times f_0$ and $f_{crit} = 1000 \times f_0$ is smaller than the one between critical values from $f_{crit} = 10 \times f_0$ and $f_{crit} = 100 \times f_0$. Otherwise with decreasing in the initial porosity, the difference in critical value becomes smaller, especially in cases of initial porosity smaller than $f_0 = 10^{-6}$. Thus we also take this two-orders-of-magnitude increase $f_{crit} = 100 \times f_0$ to signal the onset of cavitation. From above discussion, The FEM results in the following section generated in this manner (i.e., using $f_{crit} = 100 \times f_0$ as cavitation criterion) for the critical stretch λ_{crit} and corresponding critical Cauchy stress t_{crit}/μ at which cavitation occurs on the initial porosity $f_0 = 10^{-7}$.

To study the material parameter compressibility ratio μ'/μ, we also develop the models of compressibility ratios μ'/μ in the range of $0.1 \le \mu'/\mu \le 100$ on initial porosity $f_0 = 10^{-7}$ subject to hydrostatic deformations. First we work out relationships of current porosity f (see Figure 37), porosity ratio f/f_0 (see Figure 38), corresponding Cauchy stress t/μ (see Figure 39) according to principle stretch λ for the representative cases of $\mu'/\mu = 1,10,100$. The result shows that in deformation space with decrease in compressibility ratio μ'/μ which means the material is more compressible, the compressible Neo-Hookean material is more stable means cavitation occurs at large deformations. In stress space, with increase in compressibility ratio μ'/μ, corresponding Cauchy stress t/μ increase which means material is more stable in incompressibility.

Figure 40 illustrates various results for the onset of cavitation in compressible Neo-Hookean materials (58) on the critical stretch λ_{crit} at which cavitation ensues under hydrostatic loading by finite element simulations. Note from this figure that $\lambda_{crit} \ge 1$ and that it decreases monotonically with increasing μ'/μ. That is, compressible Neo-Hookean materials (58) are more stable in deformation space—in the sense that cavitation occurs at larger deformations—when they are more compressible. In this regard, if $\lambda_{crit} \to \infty$ in the limit as $\mu'/\mu \to 0$, so that cavitation does not occur in this extreme case. This asymptotic behavior is exhibited by the FEM results. On the other hand, in the limit as $\mu'/\mu \to \infty$, $\lambda_{crit} \to 1$ as well as to the FEM calculations. This limiting behavior indicates that cavitation may take place at zero applied strain in compressible Neo-Hookean solids (58) when they are taken to be incompressible. In order to corroborate that cavitation does indeed take place in this limit, however, we need to check whether the corresponding critical stress remains finite.

Now we turn to examine the onset of cavitation in compressible Neo-Hookean materials (58) in stress space. Figure 41 presents results for the critical Cauchy stress t_{crit}/μ at which cavitation ensues in compressible Neo-Hookean materials (58) under hydrostatic loading $\lambda_1 = \lambda_2 = \lambda$. It is also interesting to observe from Figure 41 that t_{crit}/μ is a monotonically increasing function of the compressibility ratio μ'/μ. Physically, this means that compressible Neo-Hookean materials (58) are more stable in stress space—in the sense that cavitation occurs at larger stresses—when they are more incompressible, which is in direct contrast to the behavior exhibited in deformation space (see Figure 40). In particular, note that $t_{crit} \to 0$ as $\mu'/\mu \to 0$, according to the FEM calculations. On the other hand, in the limit as $\mu'/\mu \to \infty$, the FEM results lead approximately to $t_{crit} = 2.6\mu$. Thus, in the case when the material is most compressible ($\mu'/\mu = 0$) cavitation does not occur. By contrast, in the case when the material is taken to be incompressible ($\mu'/\mu = \infty$), cavitation does occur.

8 Concluding Remarks

In this thesis, we made use of the finite element method (FEM) to investigate the onset of cavitation in nonlinear elastic materials that are subjected to generally nonsymmetric loading conditions. The focus was on 2D compressible, isotropic materials including the Neo-Hookean and Blatz-Ko materials. We developed a wedge mesh to study the response of these materials under hydrostatic loading conditions, and tested the results with available analytical solutions for the incompressible Neo-Hookean material and the compressible Blatz-ko solid. The wedge mesh was then utilized to generate results for a wide range of initial porosities in the range $f_0 \in [10^{-12}, 10^{-3}]$ with the objective of understanding how small the initially porosity needs to be in order to study cavitation numerically. For 2D compressible isotropic materials, we concluded that the case with $f_0 = 10^{-7}$ was representative of the case with $f_0 \to 0+$.

By making use of a square mesh, we generated results for general in-plane loading conditions. For the case of compressible Neo-Hookean materials, our results indicated that the onset of cavitation depends very strongly on the entire state of stress and not just on the amount of hydrostatic stress. In addition, an increase in the compressibility of these materials resulted in cavitation occurring at larger critical stretches but smaller critical stresses. The results exhibited also very good agreement with the theoretical cavitation criterion recently put forward by Lopez-Pamies.

Some 3D problems were also investigated. Attention was restricted to compressible Neo-Hookean materials under hydrostatic loading. We managed to develop a robust and structured 3D mesh. The results from this mesh were tested with analytical solutions available for incompressible materials subjected to hydrostatic loading. In general, the 3D results exhibited the same behavior as those found in the 2D cases. Namely, the onset of cavitation depends very strongly on the entire state of

stress and not just on the amount of hydrostatic stress and larger compressibility results in cavitation occurring at larger critical stretches but smaller critical stresses.

References

[1]. Lopez-Pamies, Ocar: Onset of Cavitatio in Compressible, Isotropic, Hyperelastic Solids. *J. Elast* 94, 115–145 (2009).

[2]. Busse, W.F.: Physics of rubber as related to the automobile. *J. Appl. Phys*. 9, 438–451 (1938).

[3]. Yerzley, F.L. Adhesion of neoprene to metal. *Ind. Eng. Chem.* 31, 950–956 (1939).

[4]. Gent, A.N., Lindley, P.B.: Internal rupture of bonded rubber cylinders in tension. *Proc. R. Soc. Lond.* A 249, 195–205 (1958).

[5]. Lindsey, G.H.: Triaxial fracture studies. *J. Appl. Phys*. 38, 4843–4852 (1967).

[6]. Gent, A.N., Park, B.: Failure processes in elastomers at or near a rigid spherical inclusion. *J. Mater. Sci.* 19, 1947–1956 (1984).

[7]. Cho, K., Gent, A.N.: Cavitation in model elastomeric composites. *J. Mater. Sci.* 23, 141–144 (1988).

[8]. Donald, A.M., Kramer, E.J.: Plastic deformation mechanisms in poly (acrylonitrile-butadiene styrene) [ABS]. *J. Mater. Sci.* 17, 1765–1772 (1982).

[9]. Schirrer, R., Fond, C., Lobbrecht, A.: Volume change and light scattering during mechanical damage in polymethy-methacrylate toughened with core-shell rubber particles. *J. Mater. Sci.* 31, 6409–6422 (1996). 34

[10]. Fond, C.: Cavitation criterion for rubber materials: A review of void-growth models. *Journal of Polymer Science: Part B* 39, 2081–2096 (2001).

[11]. Green, A.E., Zerna, W.: *Theoretical Elasticity*. Oxford University Press (1954).

[12]. Ball, J.M.: Discontinuous equilibrium solutions and cavitation in nonlinear elasticity. *Phil. Trans. R. Soc.* A 306, 557–611 (1982).

[13]. Stuart, C.A.: Radiallyly symmetric cavitation for hyperelastic materials. *Ann. Inst. Henri Poincare, Analyse non lineaire* 2, 33–66 (1985).

[14]. Sivaloganathan, J.: Uniqueness of regular and singular equilibria for spherically symmetric problems of nonlinear elasticity. *Arch. Rat. Mech. Analysis* 96, 97–136 (1986).

[15]. Sivaloganathan, J.: A field theory approach to stability of radially equilibria in nonlinear elasticity. *Math. Proc. Cambridge Phil. Soc.* 99, 589–604 (1986).

[16]. Horgan, C.O., Abeyaratne, R.: A bifurcation problem for a compressible nonlinearly elastic medium: growth of a micro-void. *J. Elasticity* 16, 189–200 (1986).

[17]. Horgan, C.O.: Void nucleation and growth for compressible non-linearly elastic materials: an example. *Int. J. Solids Structures* 29, 279–291 (1992).

[18]. Meynard, F.: Existence and nonexistence results on the radiallyly symmetric cavitation problem. *Quarterly of Applied Mathematics L,* 201–226 (1992).

[29]. Antman, S.S., Negron-Marrero, P.V.: The remarkable nature of radiallyly symmetric equilibrium states of aleotropic nonlinearly elastic bodies. *J. Elasticity* 18, 131–164 (1987).

[20]. Polignone, D.A., Horgan, C.O.: Cavitation for incompressible anisotropic nonlinearly elastic spheres. *J. Elasticity* 33, 27–65. (1993).

[21]. Pericak-Spector, K.A., Spector, S.J.: Nonuniqueness for hyperbolic systems: cavitation in nonlinear elastodynamics. *Arch. Rat. Mech. Analysis* 101, 293–317 (1988).

[22]. Horgan, C.O., Polignone, D.A.: Cavitation in nonlinearly elastic solids: a review. *Applied Mechanics Reviews* 48, 471–485. (1995).

[23]. James, R.D., Spector, S.J.: The formation of filamentary voids in solids. *J. Mech. Phys. Solids* 39, 783–813 (1991).

[24]. Hou, H.-S., Abeyaratne, R.: Cavitation in elastic and elastic-plastic solids. *J. Mech. Phys. Solids* 40, 571–592 (1992).

[25]. Steenbrink, A.C., Van der Giessen, E.: On cavitation, post-cavitation and yield in amorphous polymer-rubber blends. *J. Mech. Phys. Solids* 47, 843–876 (1999).

[26]. Huang, Y., Hutchinson, J.W., Tvergaard, V.: Cavitation instabilities in elastic-plastic solids. *J. Mech. Phys. Solids* 39, 223–241 (1991).

[27]. Tvergaard, V., Hutchinson, J.W.: Effect of void shape on the occurrence of cavitation instabilities in elastic-plastic solids. *J. Appl. Mech*. 60, 807–812 (1993).

[28]. Ogden, R.W.: *Non-linear elastic deformations*. Dover Publications, Inc (1997).

[29]. Eshelby, J.D.: The determination of the elastic field of an ellipsoidal inclusion, and related problems. *Proc. R. Soc. Lond.* A 241, 376-396 (1957)

[30]. Lopez-Pamies, O., Ponte Castaneda, P.: On the overall behavior, microstructure evolution, and macrocsopic stability in reinforced rubbers at large deformations. II-Application to cylindrical fibers. *J. Mech. Phys. Solids* 54, 831-863 (2006)

[31]. Z Hashin, Large Isotropic elastic deformation of composites and porous media. Internat. *J. Solids Struct.* 21 (1985) 711-720

[32]. Hill, R.: Aspects of invariance in solid mechanics. *Asv. Appl. Mech.* 18, 1-75 (1978)

[33]. Storakers, B.: On material representation and constitutive branching in finite compressible elasticity. *J. Mech. Phys. Solids* 34, 125-145 (1986)

[34]. Blatz, P.J., Ko, W.L.: Application of finite elastic theory to the deformation of rubbery materials. *Trans. Soc. Rheology* 6, 223-251 (1962)

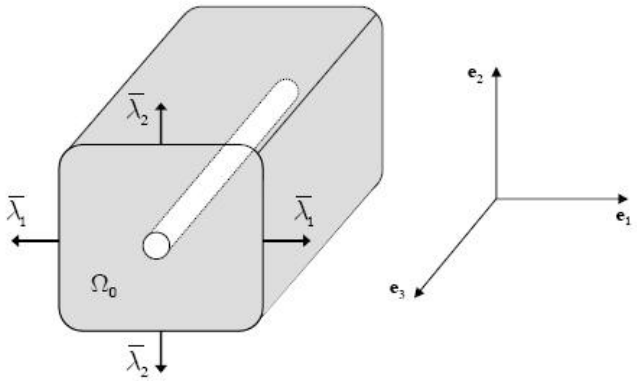

Figure 1. Schematic representation—in the undeformed configuration—of a cylindrical vacuous inhomogeneity, with initially circular cross section, in an infinite matrix phase subjected to in-plane principal stretches $\overline{\lambda}_1$ and $\overline{\lambda}_2$ Note that the long axis of the void has been aligned with the laboratory basis vector e_3.

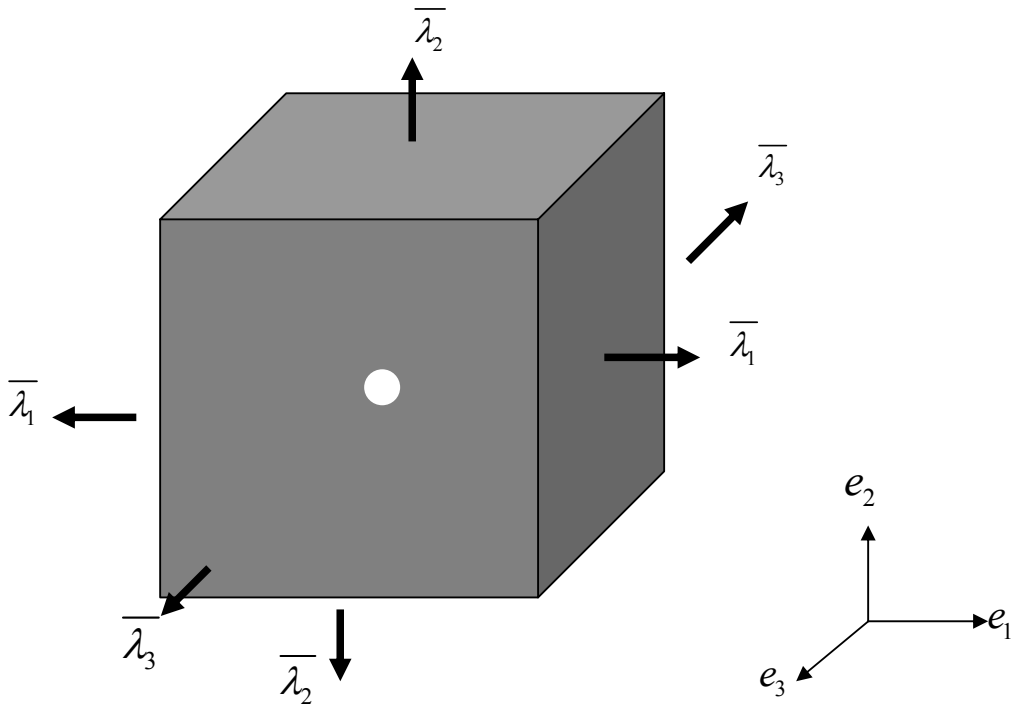

Figure 2. Schematic representation-in the undeformed configuration-of a spherical vacuous inhomogeneity in the center of a large matrix phase subjected to principal stretches $\overline{\lambda}_1$, $\overline{\lambda}_2$ and $\overline{\lambda}_3$.

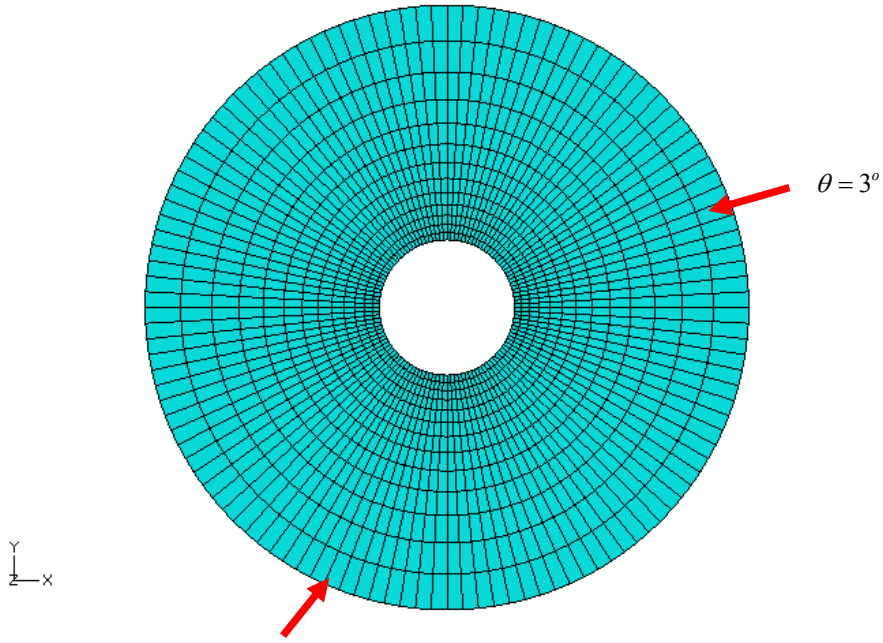

Transfer the nodes on boundary into cylindrical coordinate system to apply the hydrostatic loading condition

(a)

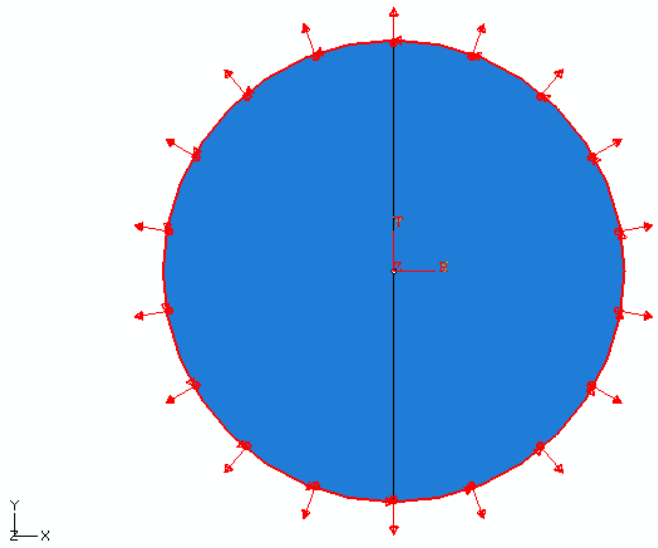

(b)

Figure 3. (a) Schematic representation of the shell mesh model and (b) shows the hydrostatic loading condition applied on the boundary.

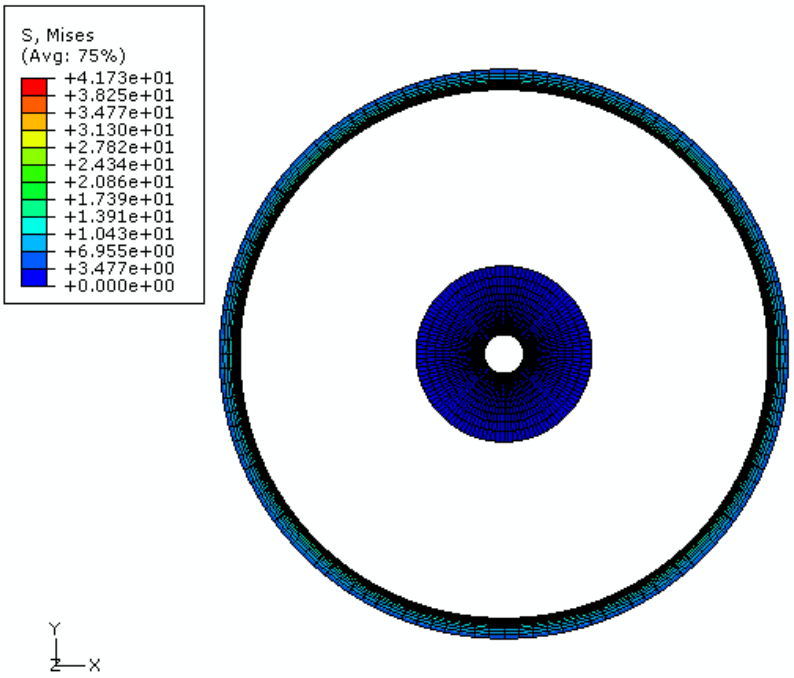

Figure 4. Schematic representation of underformed and deformed configuration of the shell mesh model of the compressible Neo-Hookean materials with initial porosity 10^{-2} and compressibility ratio $\mu'/\mu = 10$.

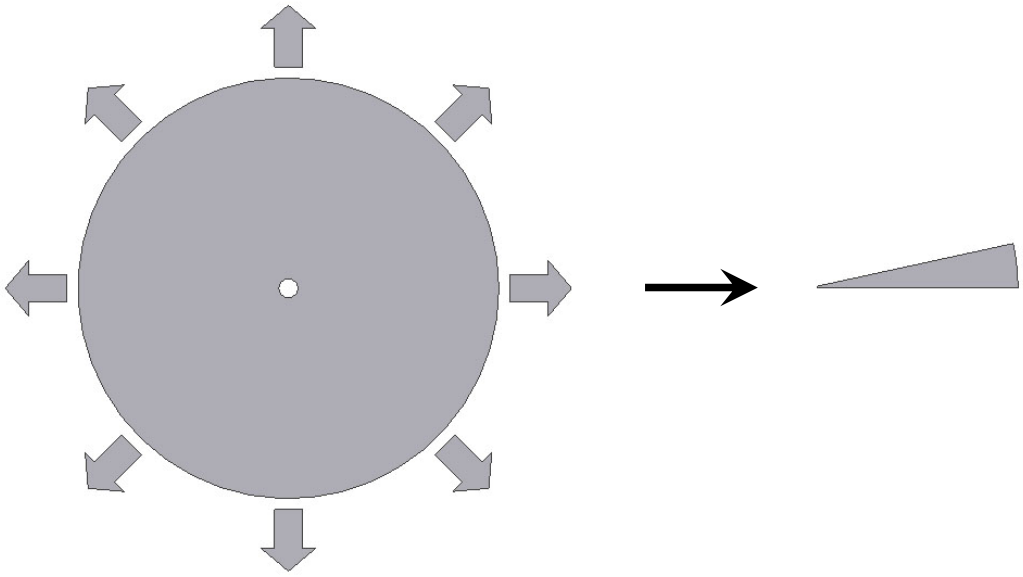

Figure 5. Schematic simplifications of procedure of the 2D model of an infinitesimal circle in a finite circle into the one layer mesh based on symmetric geometry and loading condition.

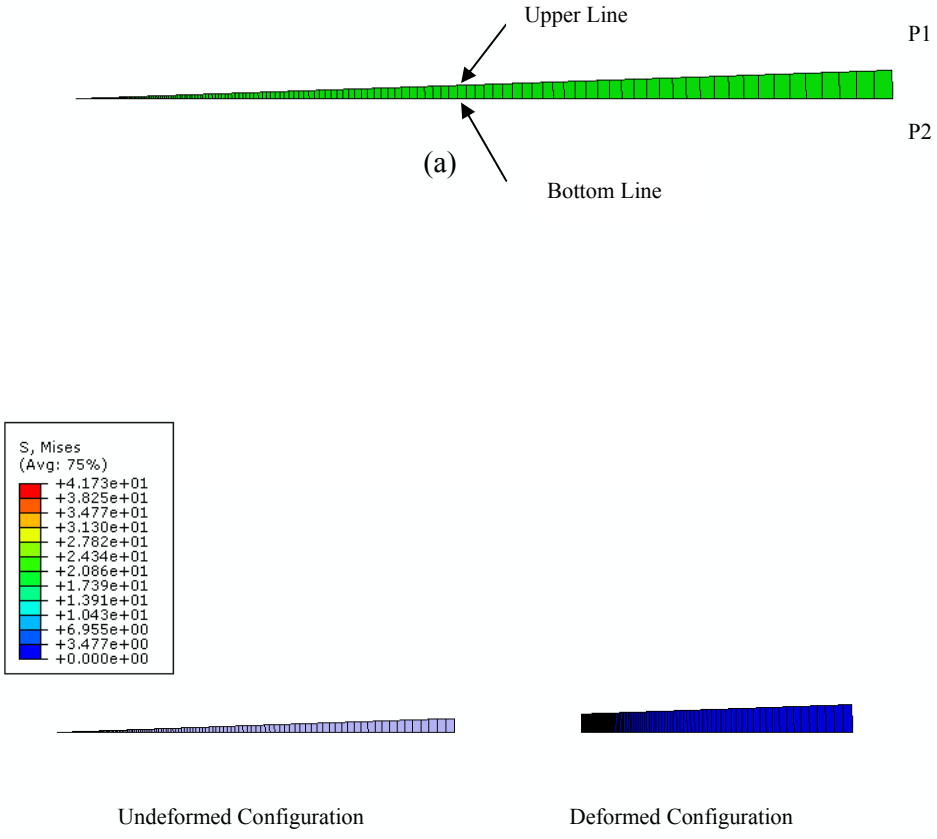

Figure 6. (a) Schematic representation of the wedge mesh subject to hydrostatic loading (b) The undeformed and deformed configuration of wedge mesh model for compressible Neo-Hookean materials at initial porosity $f_0 = 10^{-2}$ and compressibility ratio $\mu'/\mu = 10$.

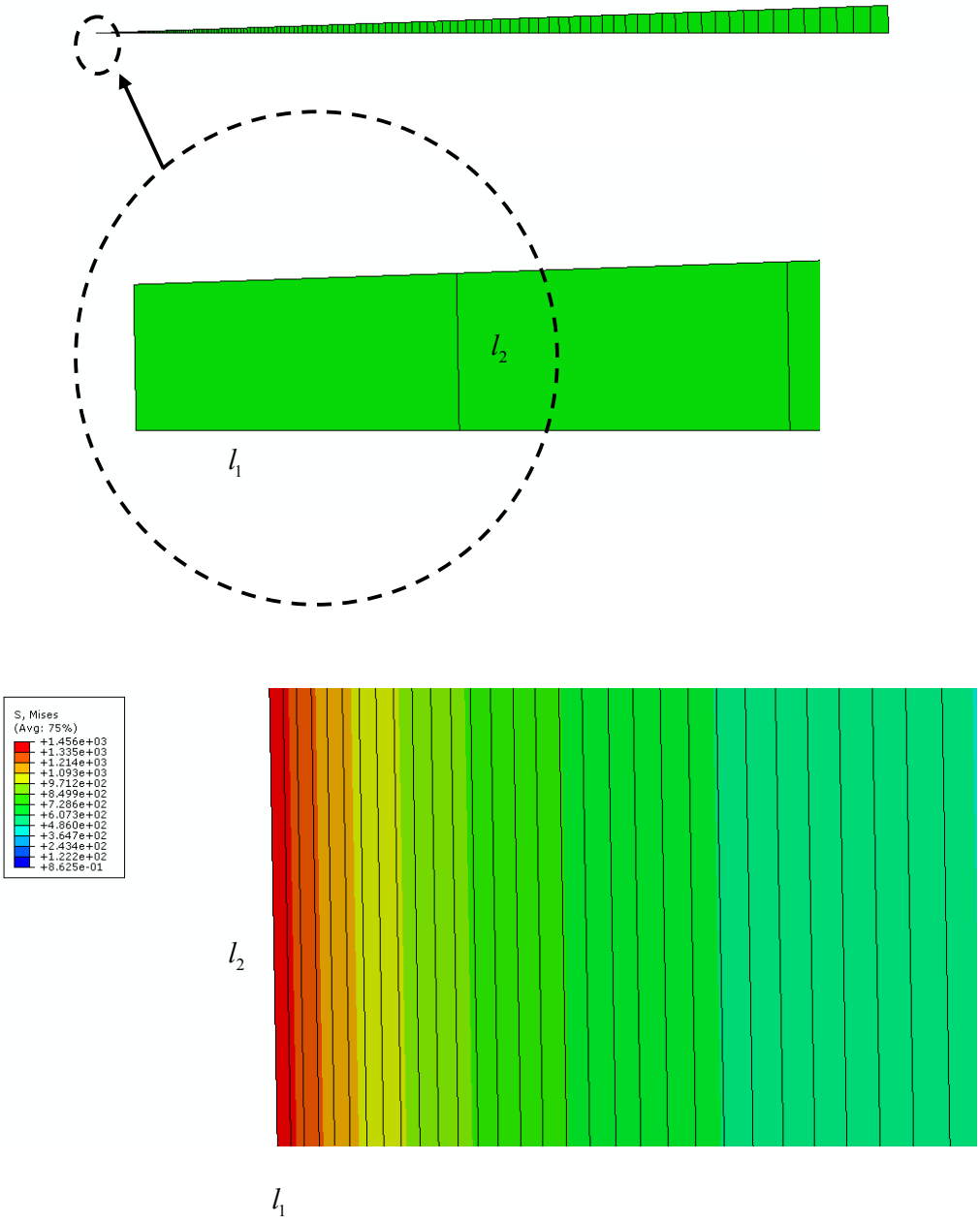

Figure 7. Schematic representations of the deformation of monitored element located near the void when cavitation occurs.

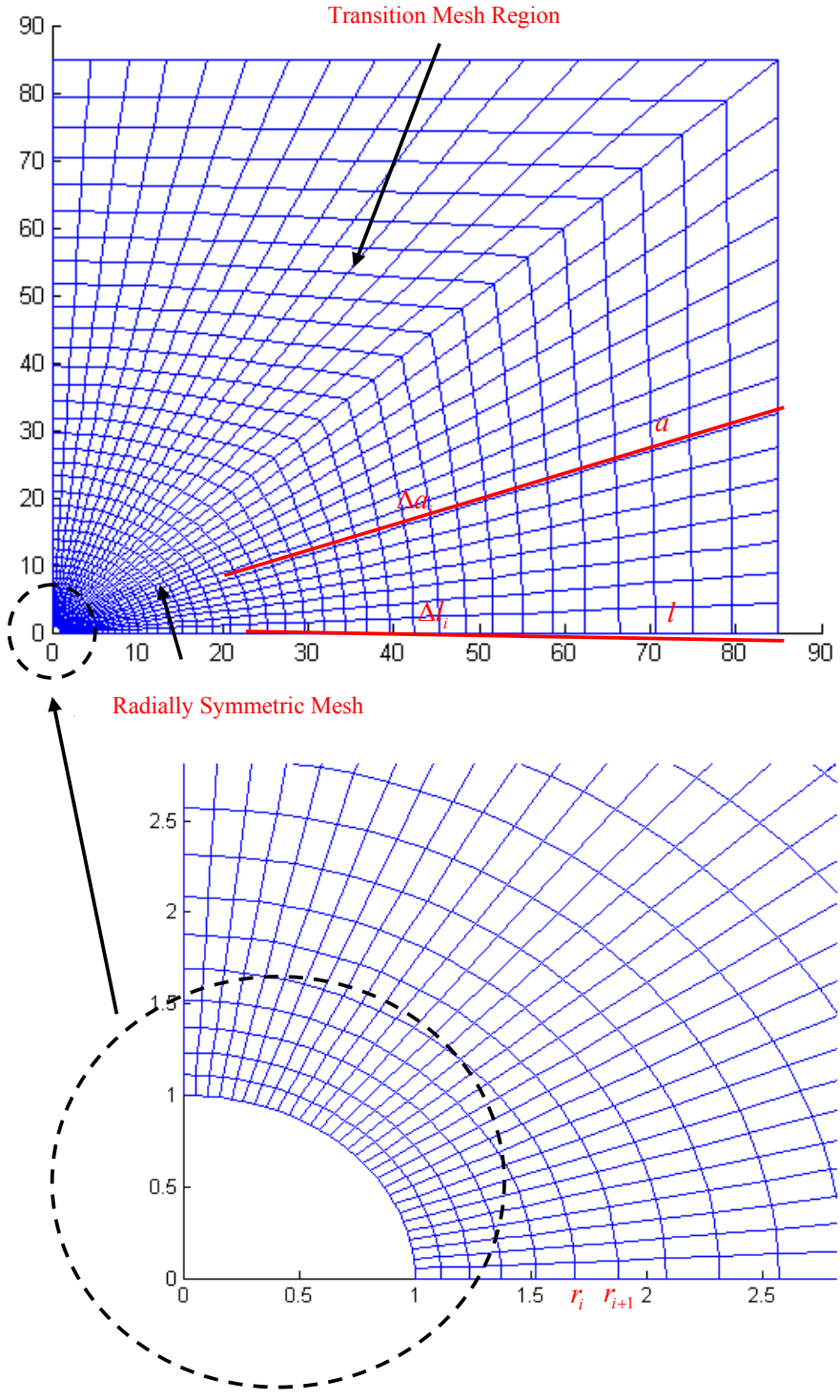

Figure 8. Schematic representations of procedure to make rectangular mesh

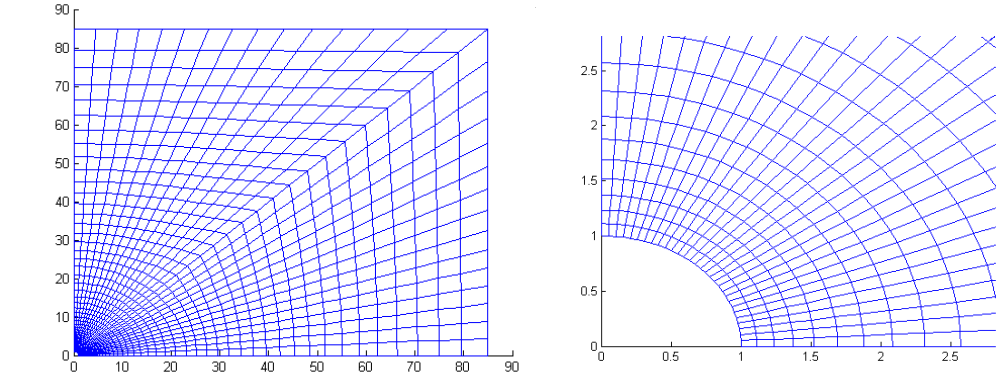

(a)

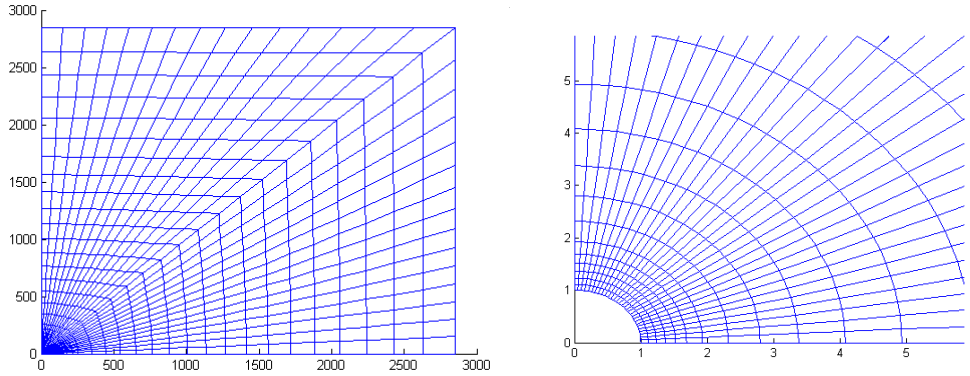

(b)

Figure 9. (a) The rectangular mesh at initial porosity $f_0 = 10^{-6}$ (b) the rectangular mesh at initial porosity $f_0 = 10^{-7}$ after changing.

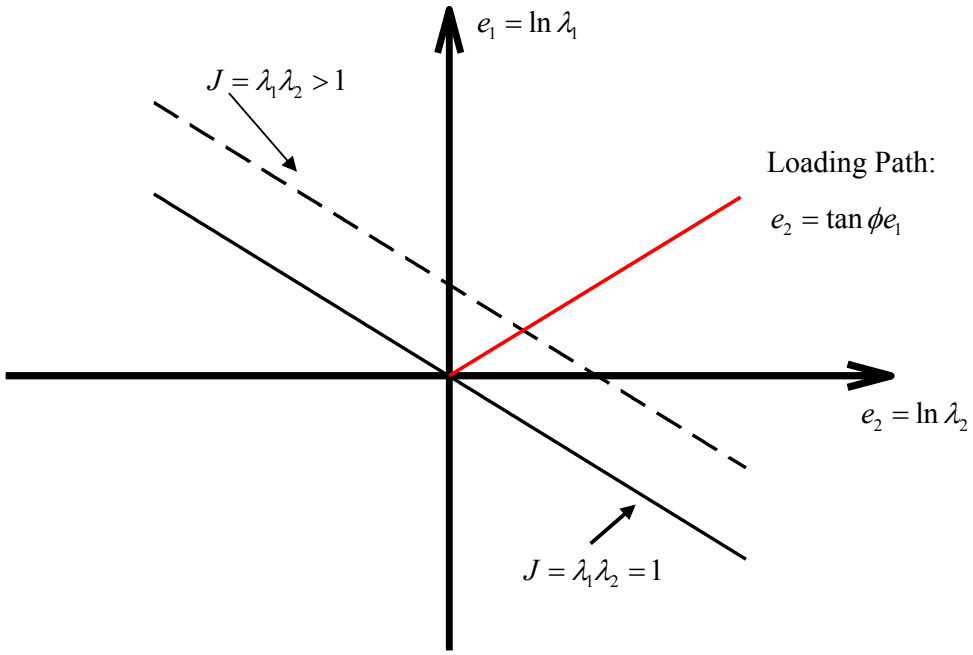

Figure 10. Schematic representations of applied loading condition for generally non-symmetric deformation in related (e_1, e_2) deformation space

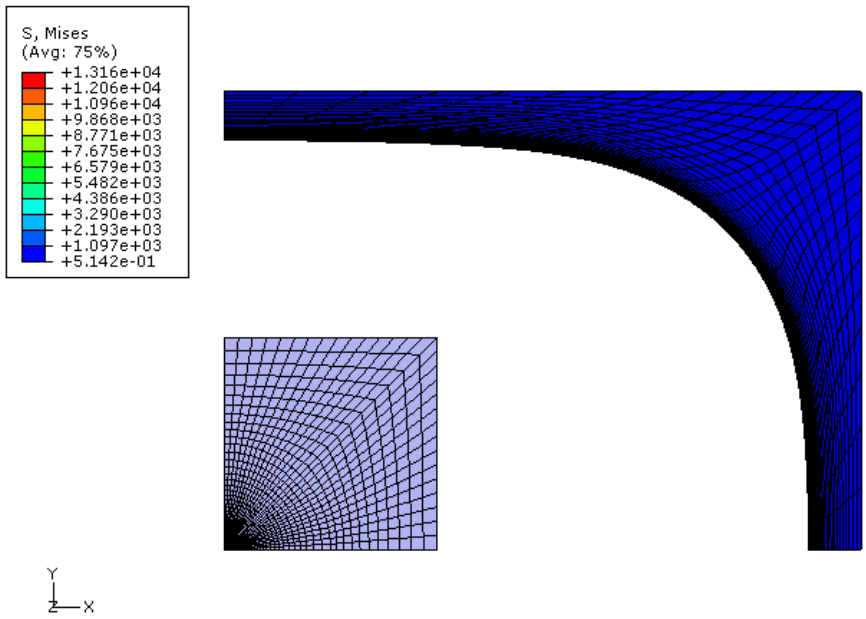

(a)

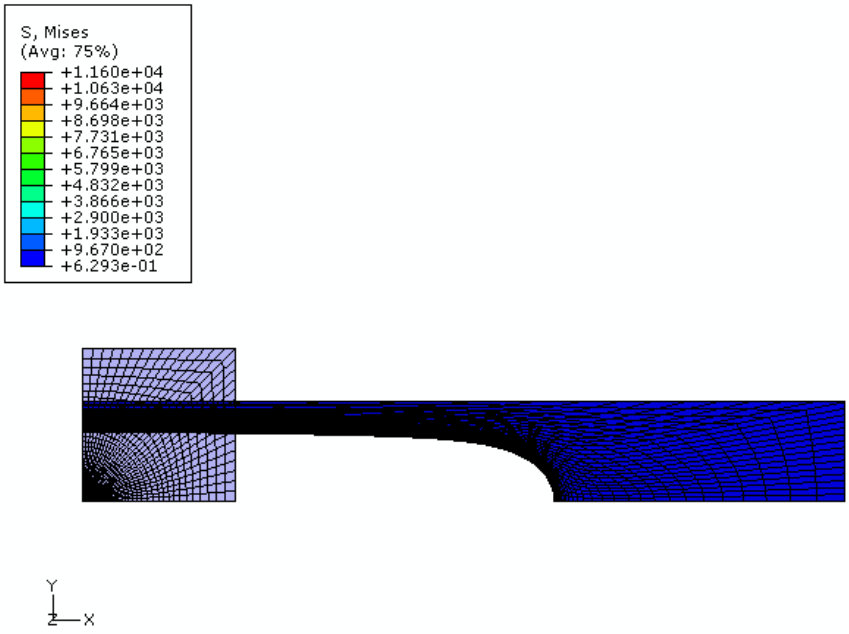

(b)

Figure 11. (a) Undeformed and deformed configuration of rectangular mesh for compressible Noe-Hookean material at initial porosity $f_0 = 10^{-7}$ and compressibility ratio $\mu'/\mu = 10$ under loading angle $\theta = 35^o$, (b) Undeformed and deformed configuration under loading angle $\theta = -15^o$

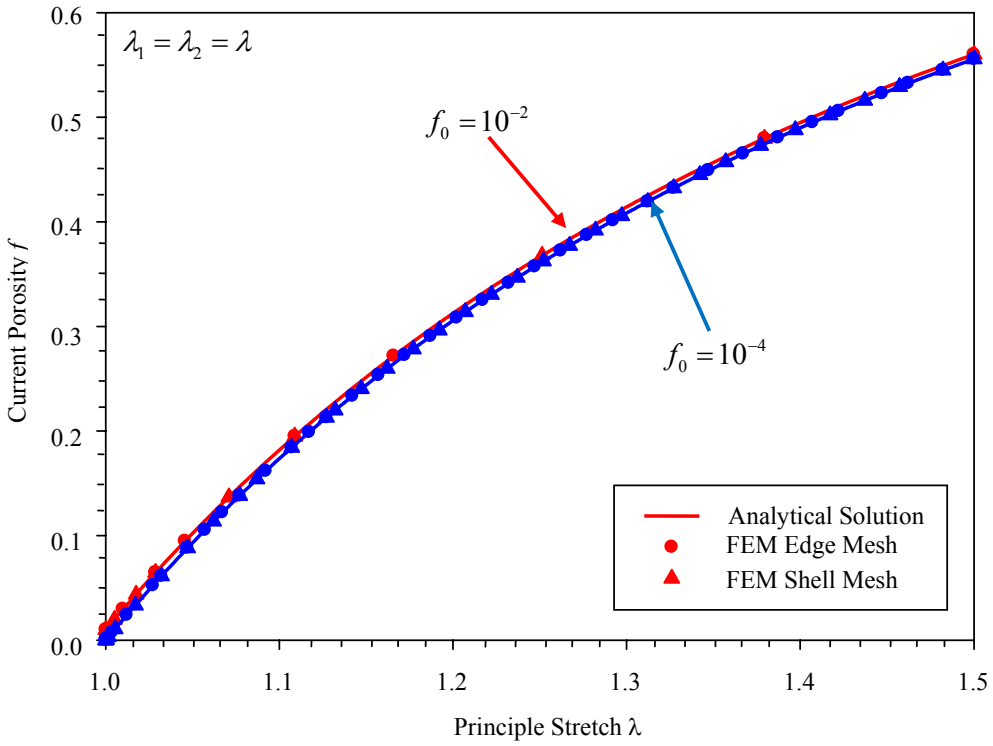

Figure 12. FEM and analytical solution results for current porosity f check among the models of analytical solution, wedge mesh and shell mesh for incompressible Neo-Hookean material (37) at initial porosity 10^{-2} and 10^{-4}.

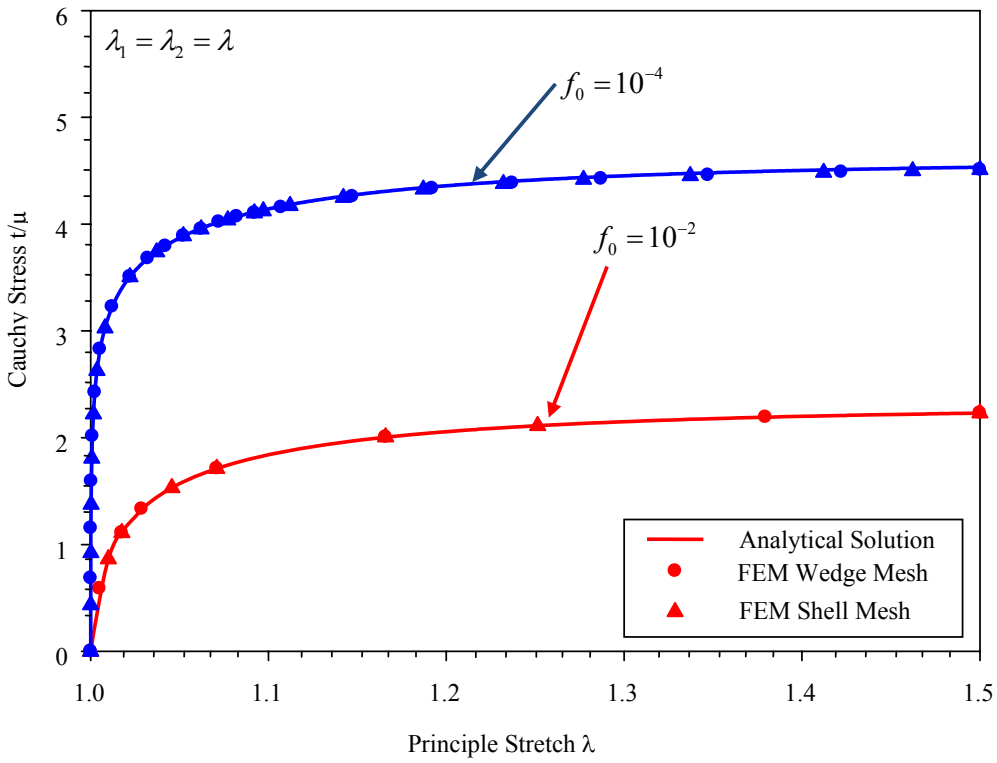

Figure 13. FEM and analytical solution results for corresponding Cauchy stress t/μ check among the models of analytical solution, wedge mesh and shell mesh for incompressible Neo-Hookean material (37) at initial porosity 10^{-2} and 10^{-4}.

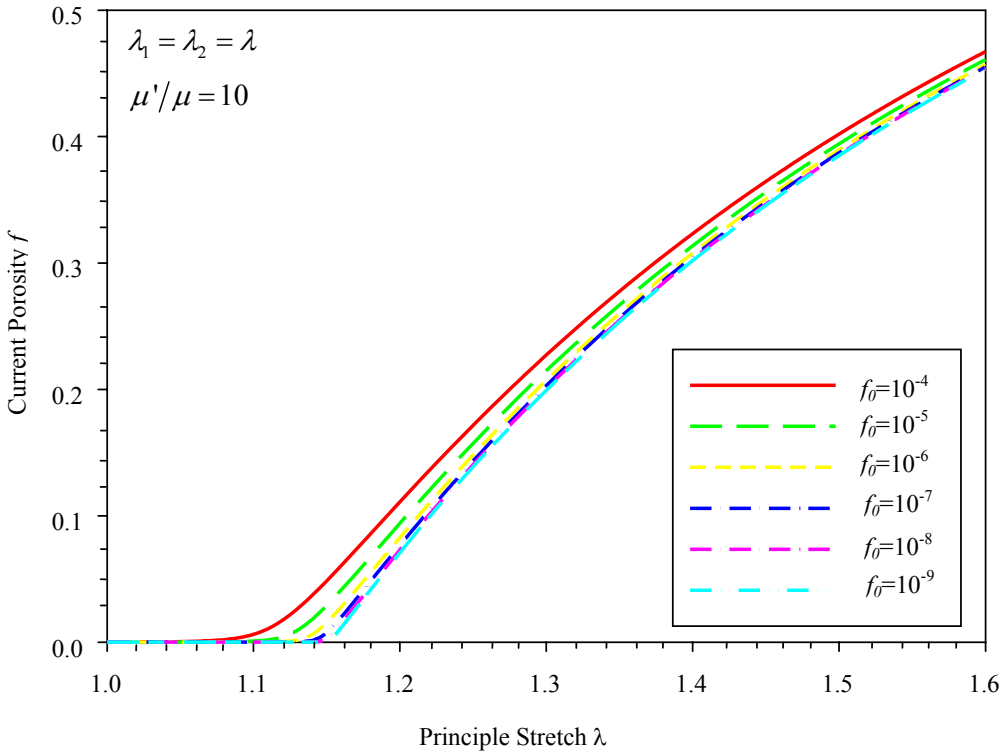

Figure 14. The FEM results of current porosity f on wedge mesh models of different initial porosity for compressible Neo-Hookean materials (36) with compressibility ratio $\mu'/\mu = 10$ under hydrostatic deformation.

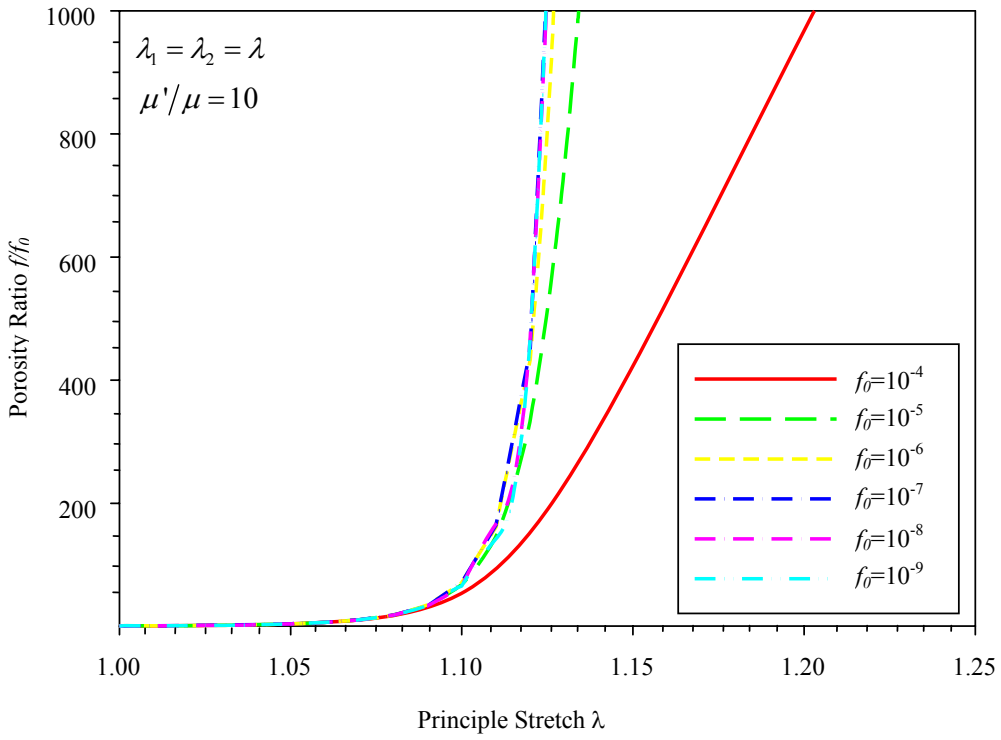

Figure 15. The FEM results of porosity ratio f/f_0 on wedge mesh models of different initial porosity for compressible Neo-Hookean materials (36) with compressibility ratio $\mu'/\mu = 10$ under hydrostatic deformation.

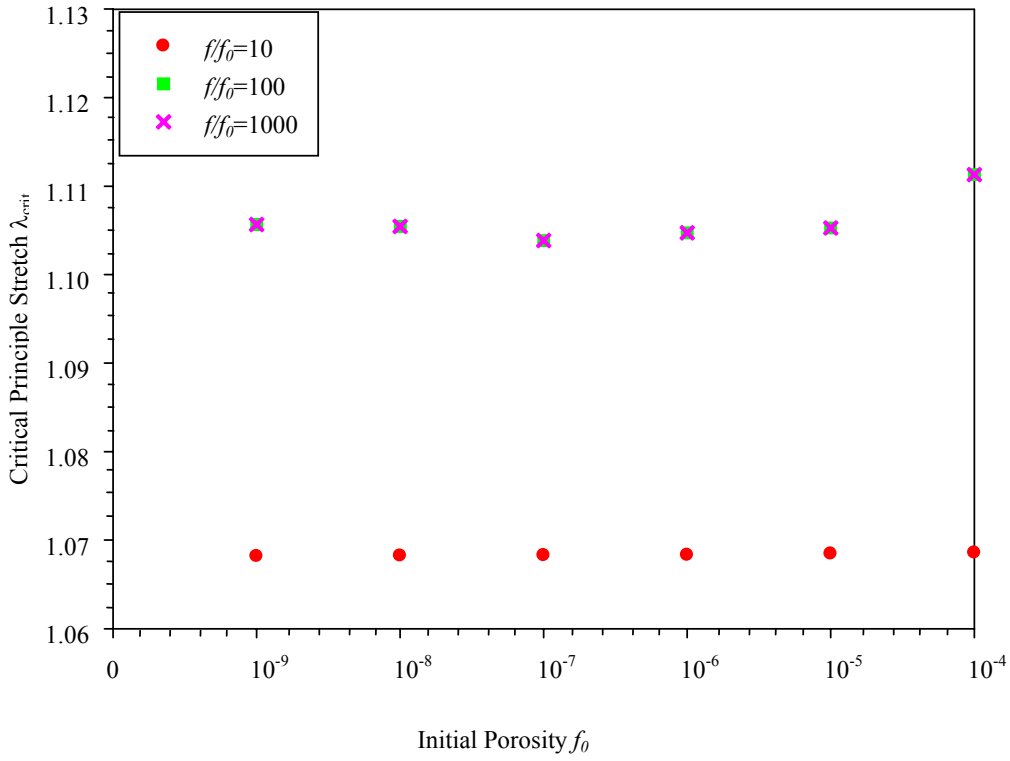

Figure 16. The FEM results of critical principle stretch λ_{crit}, which are generated by three criterions, on wedge mesh models of different initial porosity for compressible Neo-Hookean materials (36) with compressibility ratio $\mu'/\mu = 10$ under hydrostatic deformation

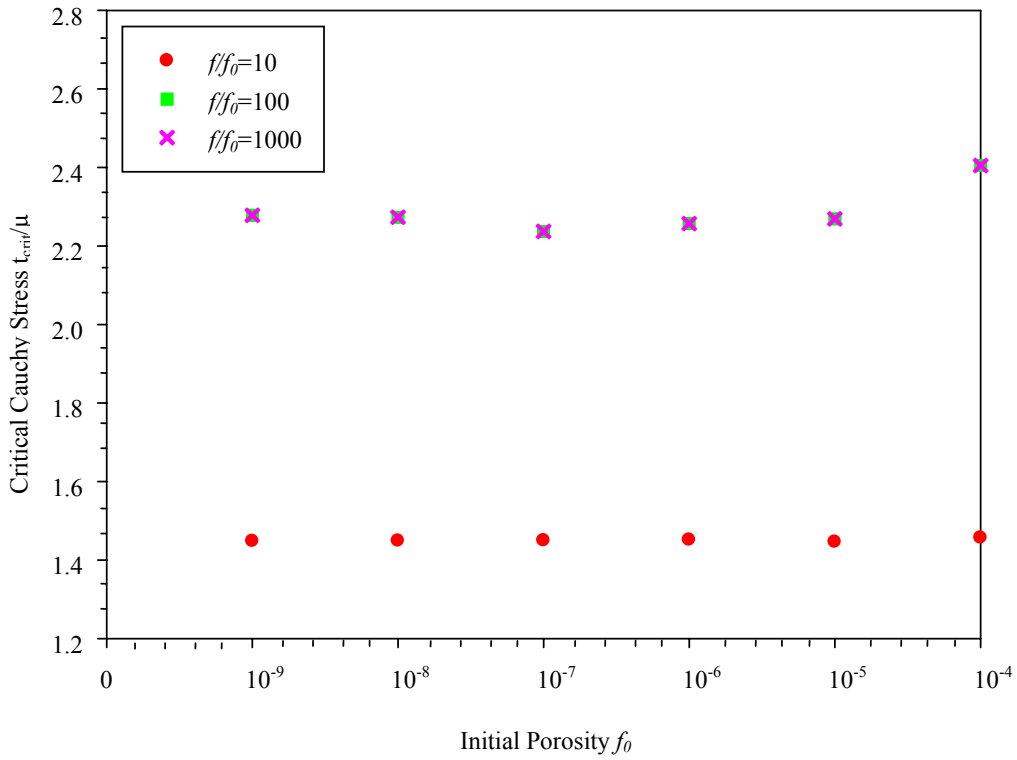

Figure 17. The FEM results of critical corresponding Cauchy stress t_{crit}/μ , which are generated by three criterions, on wedge mesh models of different initial porosity for compressible Neo-Hookean materials (36) with compressibility ratio $\mu'/\mu = 10$ under hydrostatic deformation.

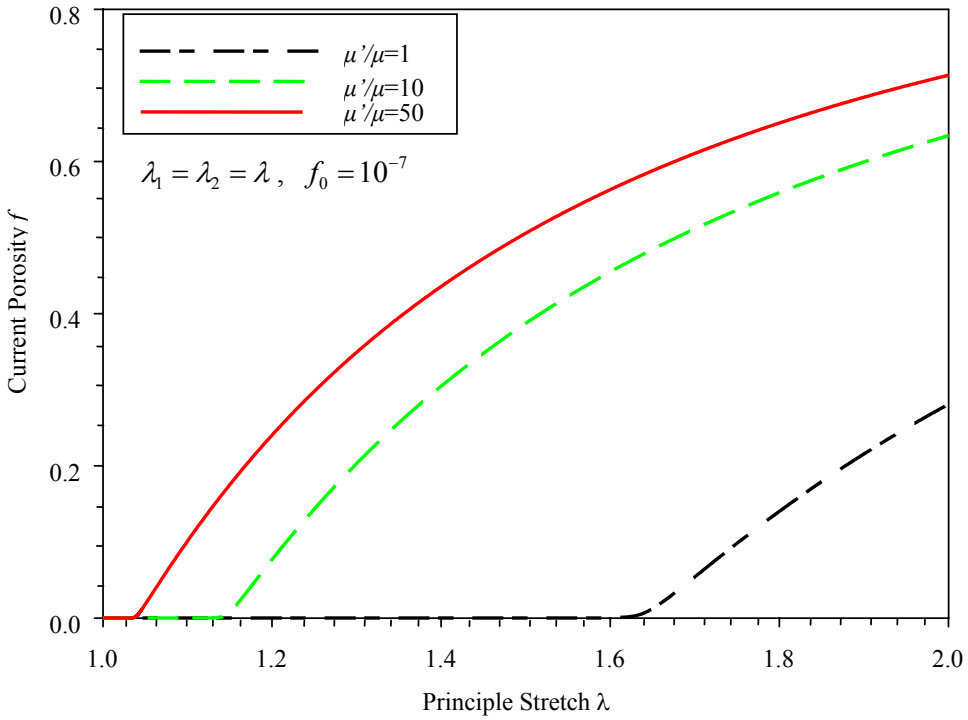

Figure 18. FEM results for absolute current porosity f on wedge mesh models of initial porosity $f_0 = 10^{-7}$ for compressible Neo-Hookean materials (36) with different compressibility ratio $\mu'/\mu = 1, 10, 50$ under hydrostatic deformations.

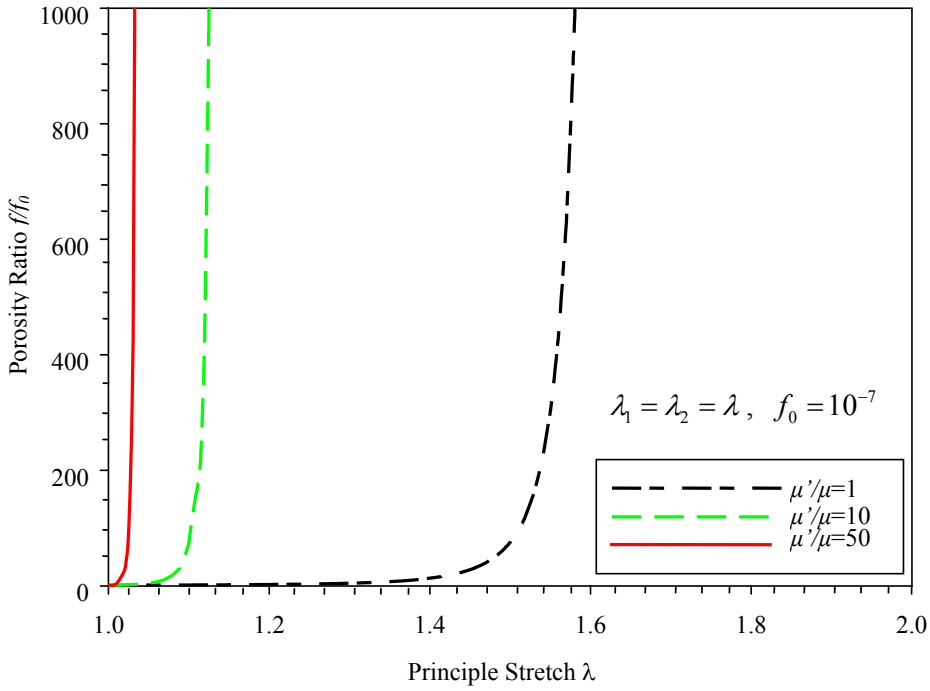

Figure 19. FEM results for porosity ratio f/f_0 on wedge mesh models of initial porosity $f_0 = 10^{-7}$ for compressible Neo-Hookean materials (36) with different compressibility ratio $\mu'/\mu = 1, 10, 50$ under hydrostatic deformations.

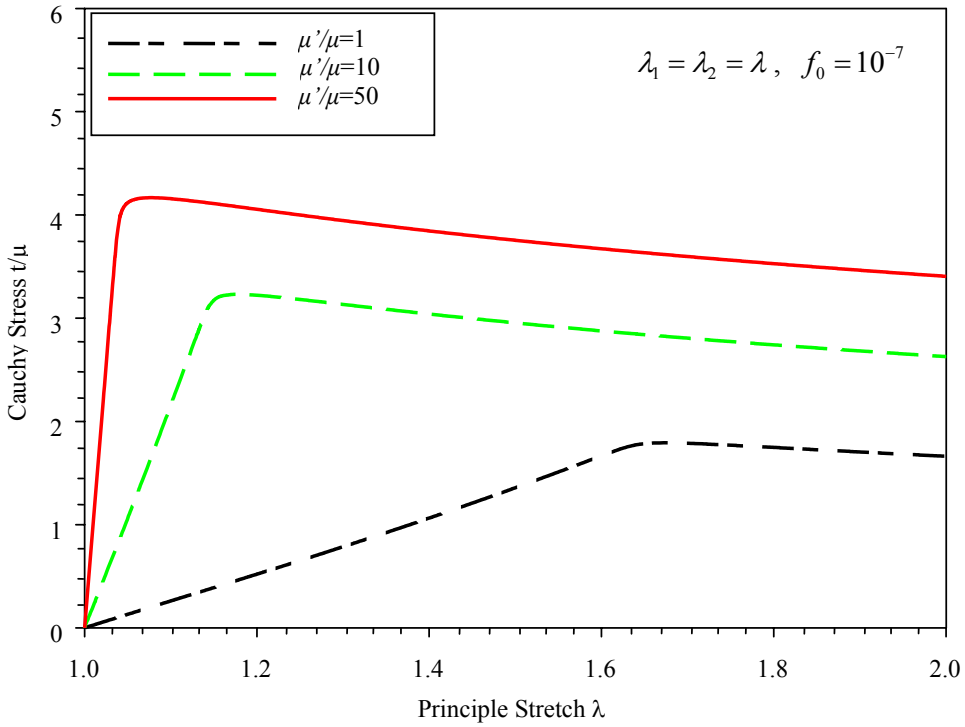

Figure 20. FEM results for corresponding Cauchy stress t/μ on wedge mesh models of initial porosity $f_0 = 10^{-7}$ for compressible Neo-Hookean materials (36) with different compressibility ratio $\mu'/\mu = 1, 10, 50$ under hydrostatic deformations.

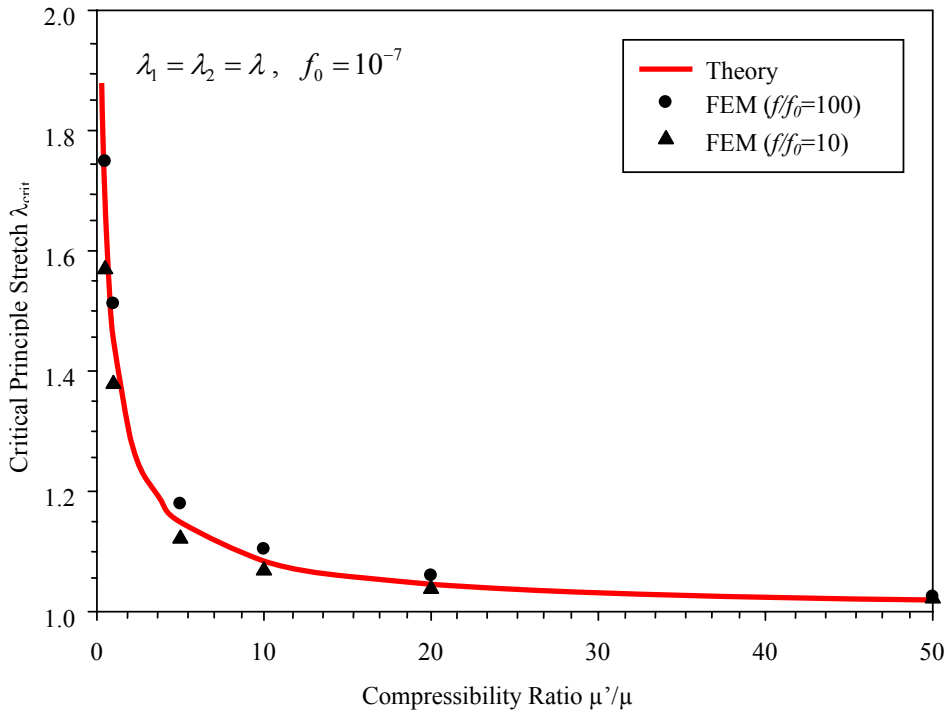

Figure 21. The critical stretch λ_{crit} at which cavitation occurs in compressible Neo-Hookean materials subjected to hydrostatic deformation, as a function of the compressibility ratio μ'/μ. The solid line corresponds to the variational approximation (41), and the points correspond to FEM calculations.

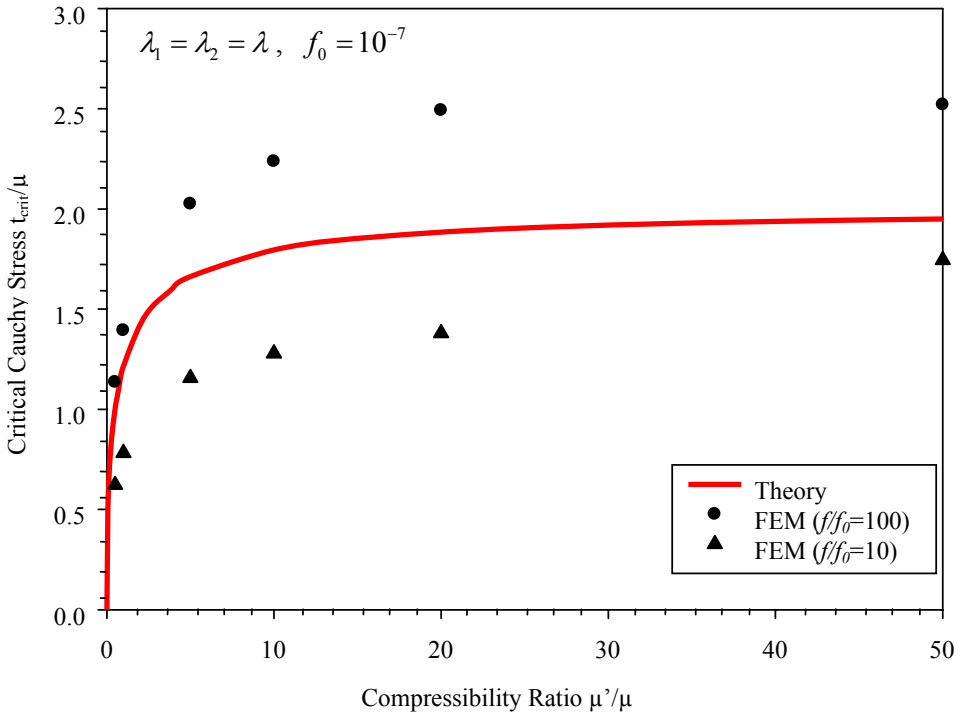

Figure 22. The critical corresponding Cauchy stress t_{crit}/μ at which cavitation occurs in compressible Neo-Hookean materials subjected to hydrostatic deformation, as a function of the compressibility ratio μ'/μ. The solid line corresponds to the variational approximation (42), and the points correspond to FEM calculations.

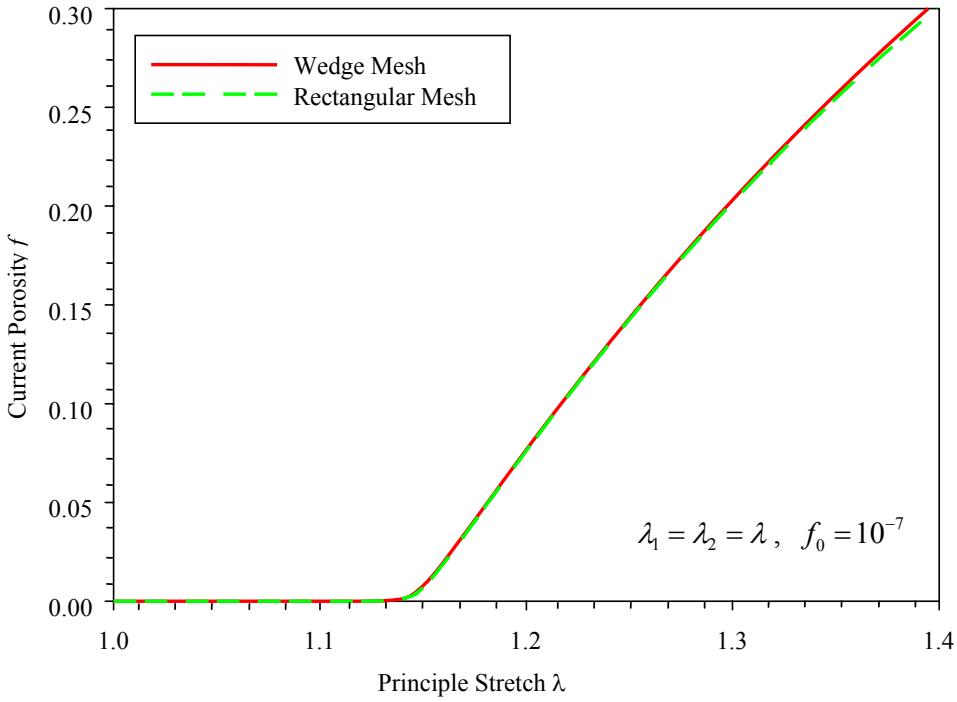

Figure 23. FEM result in current porosity f check on the wedge mesh and rectangular mesh of initial porosity $f_0 = 10^{-7}$ for compressible Neo-Hookean materials (36) with compressibility ratio $\mu'/\mu = 10$ under hydrostatic deformation.

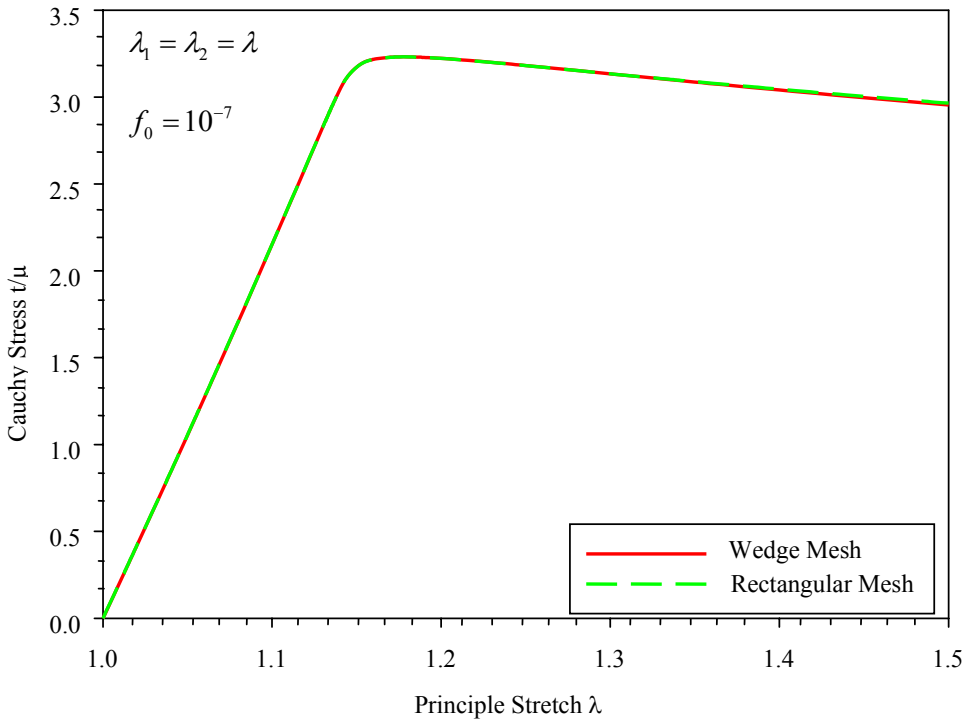

Figure 24. FEM result in corresponding Cauchy stress t/μ check on the wedge mesh and rectangular mesh of initial porosity $f_0 = 10^{-7}$ for compressible Neo-Hookean materials (36) with compressibility ratio $\mu'/\mu = 10$ under hydrostatic deformation..

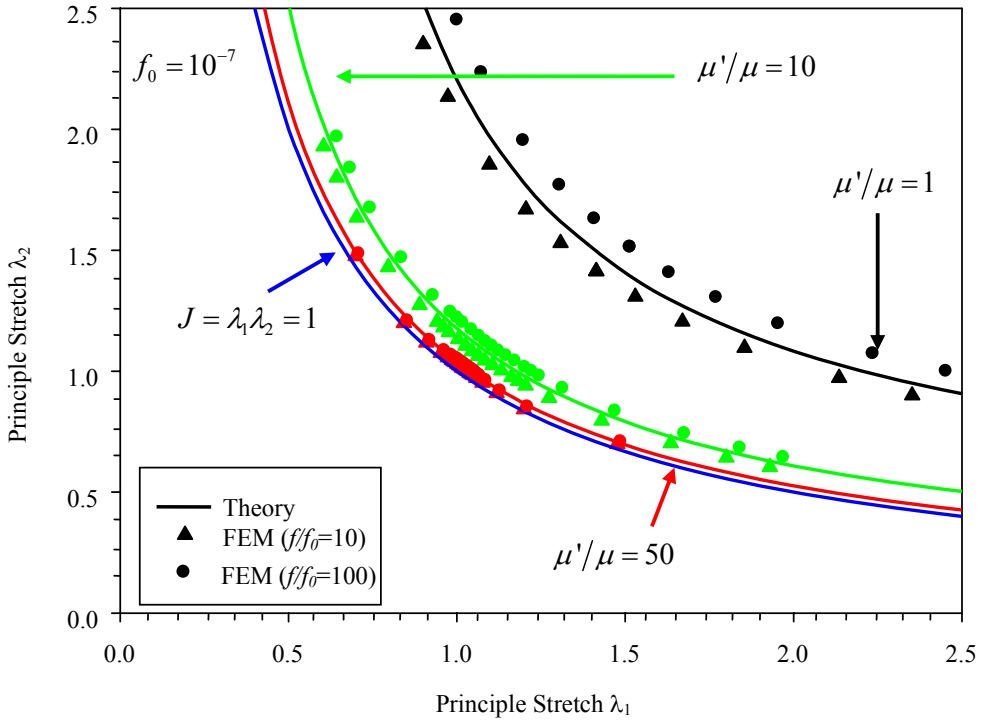

Figure 25. Cavitation curves on FEM results and theory in (λ_1, λ_2)–deformation space for compressible Neo-Hookean materials (36) with $\mu'/\mu = 1, 10, 50$, as determined by the criterion (46).

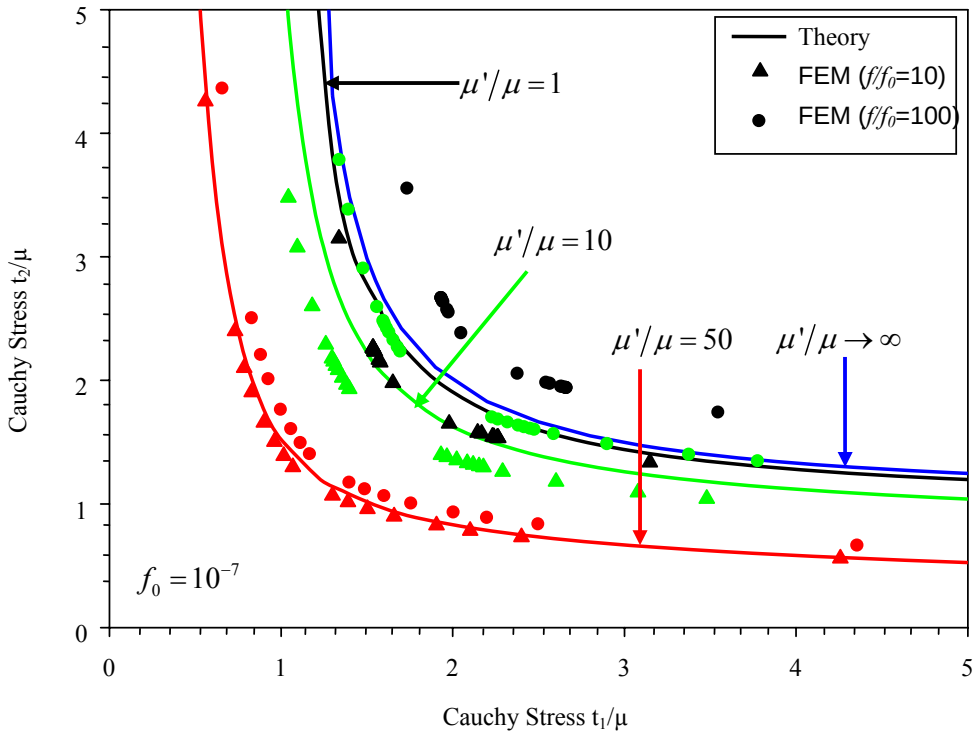

Figure 26. Cavitation curves of FEM and theory in $(t_1/\mu, t_2/\mu)$–stress space for compressible Neo-Hookean materials (36) with $\mu'/\mu = 1, 10, 50$, as determined by the criterion (48).

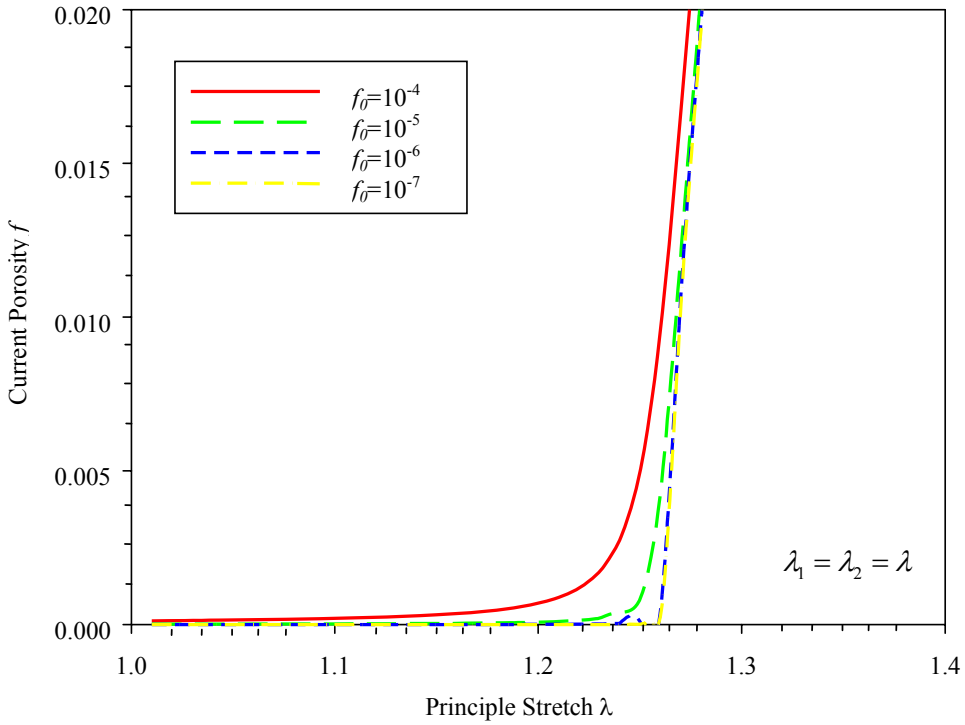

Figure 27. Representative FEM results on wedge mesh models of Blatz-Ko material (50) with initial porosity $f_0 = 10^{-4}, 10^{-5}, 10^{-6}, 10^{-7}$ under hydrostatic deformations.

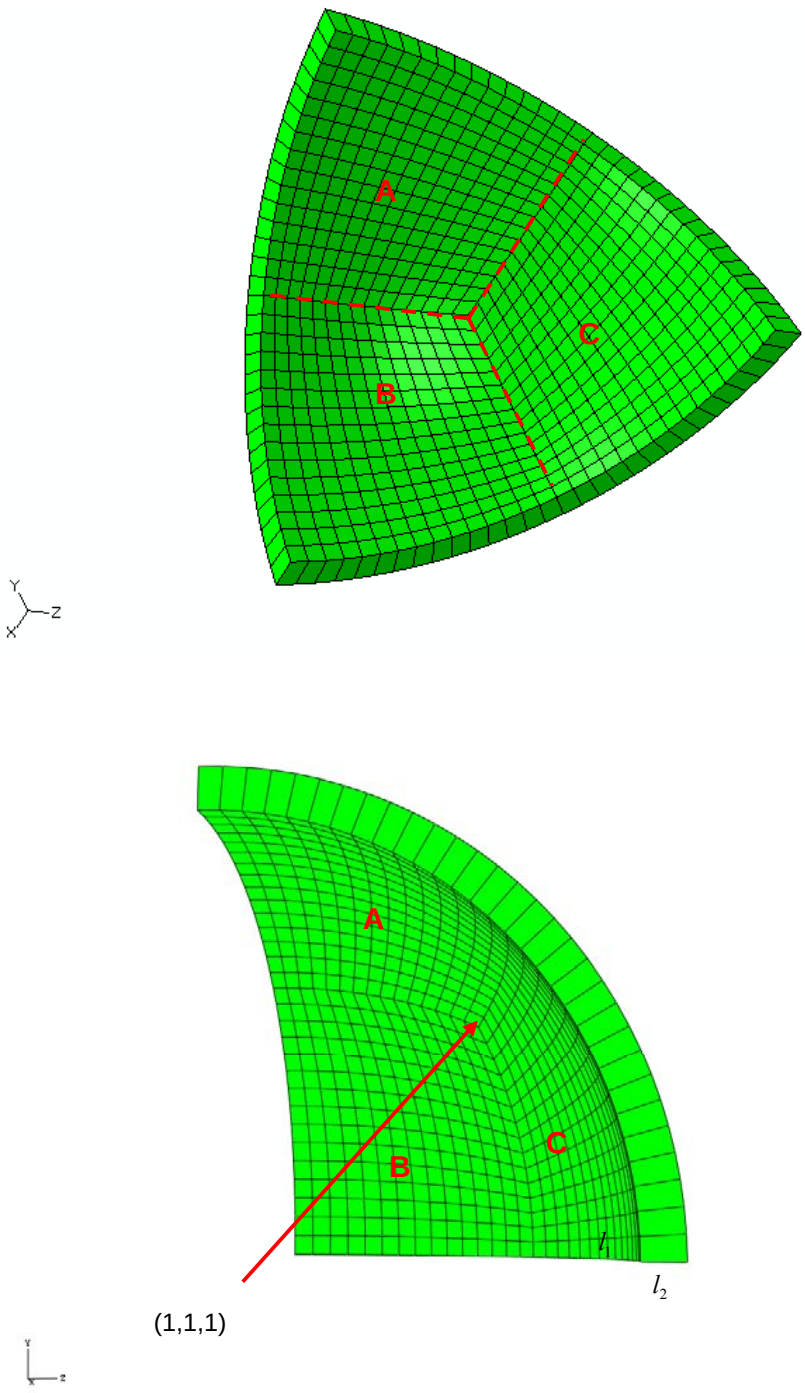

Figure 28. Schematic geometry of one layer spherical mesh with near cube element and nearly square cross-section

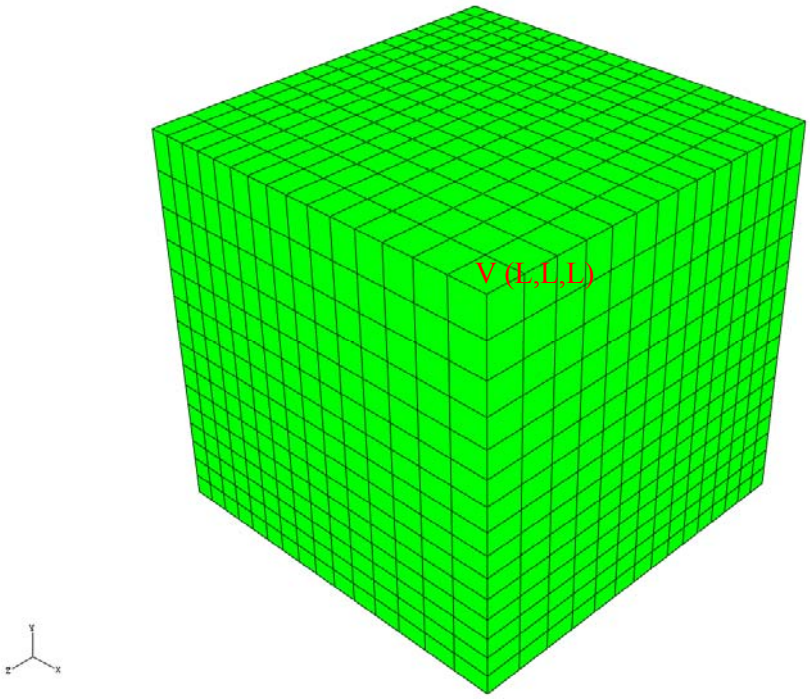

(a)

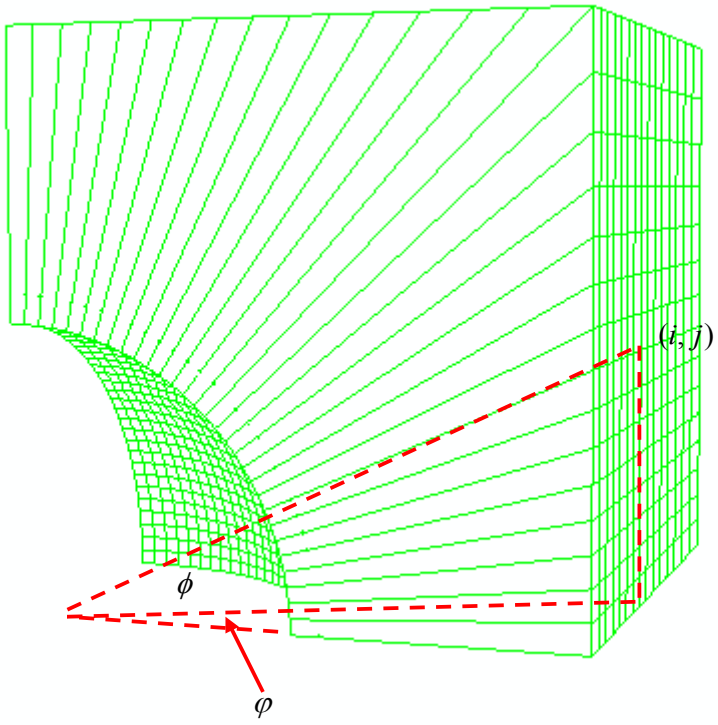

(b)

Figure 29. Schematic representation of procedure to make the symmetric and distributed even element spherical surface

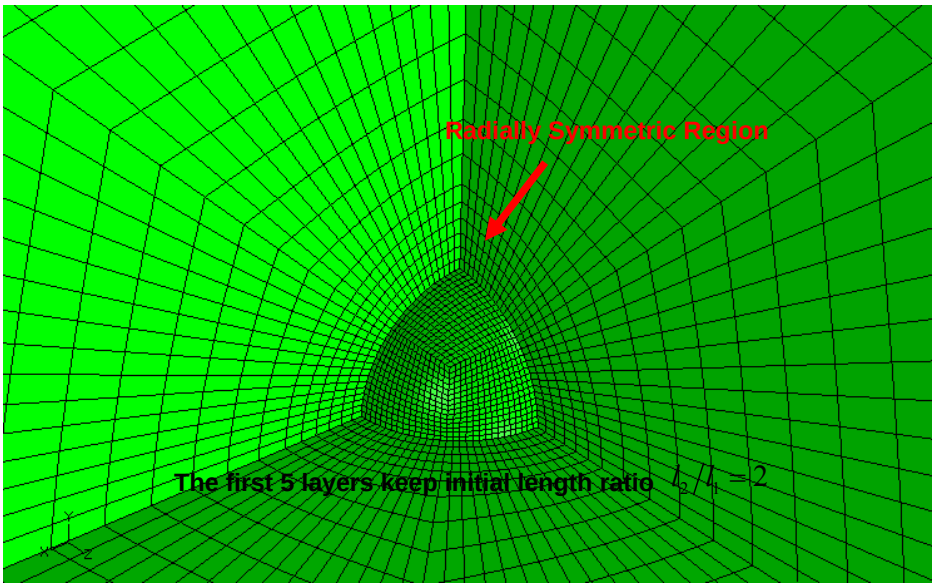

(a)

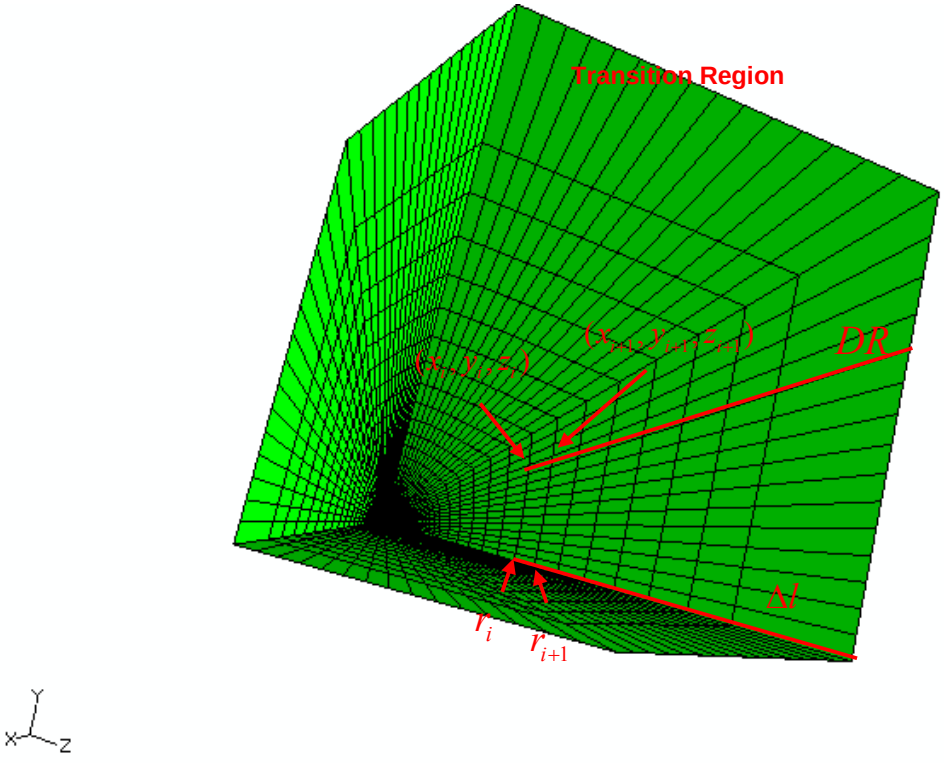

(b)

Figure 30. Schematic representation of procedure to make the whole mesh in radially symmetric region and transition region

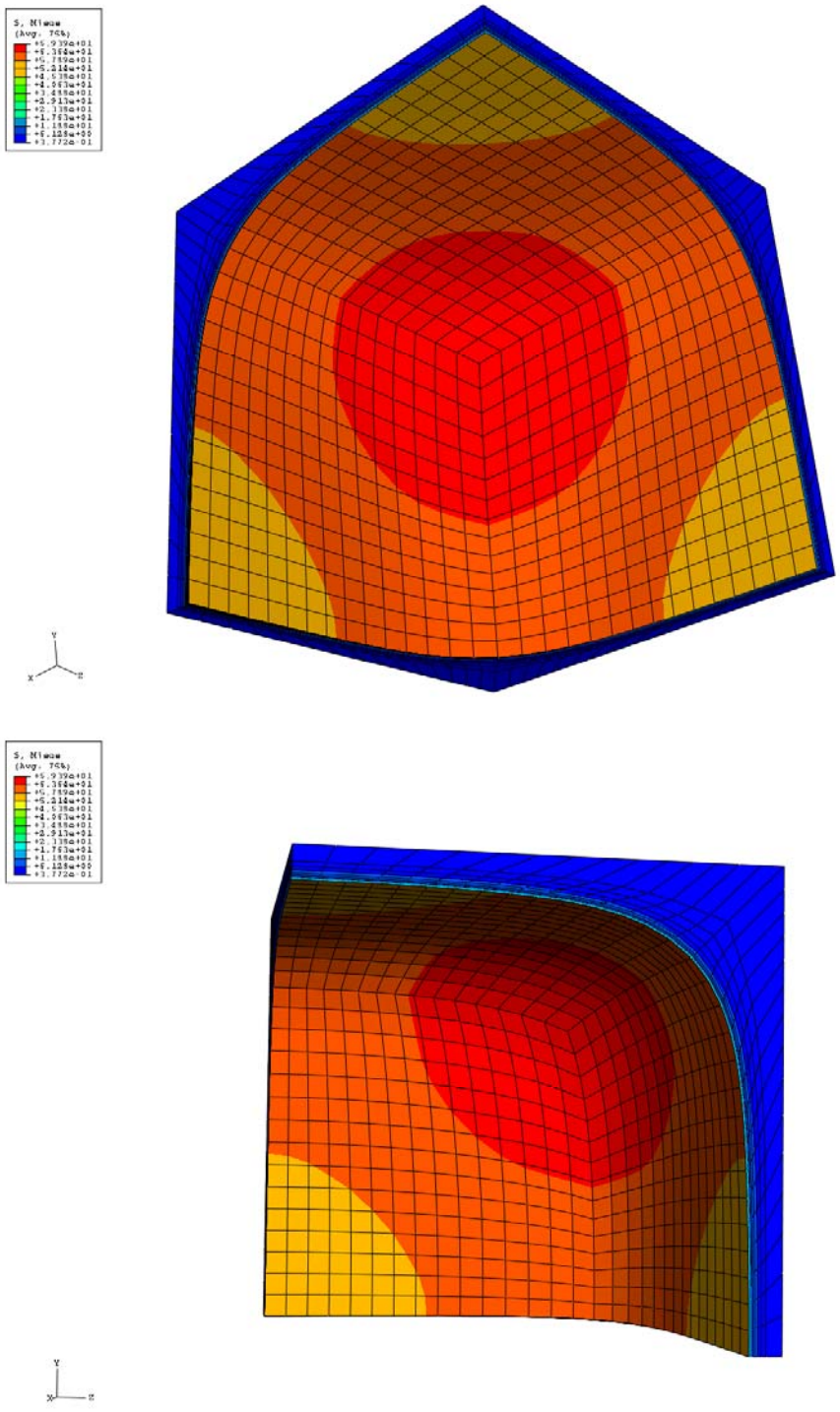

Figure 31. Schematic representation in the stress contour on 3D mesh models for compressible Neo-Hookean materials (58) with initial porosity $f_0 = 10^{-4}$ and compressibility ratio $\mu'/\mu = 10$.

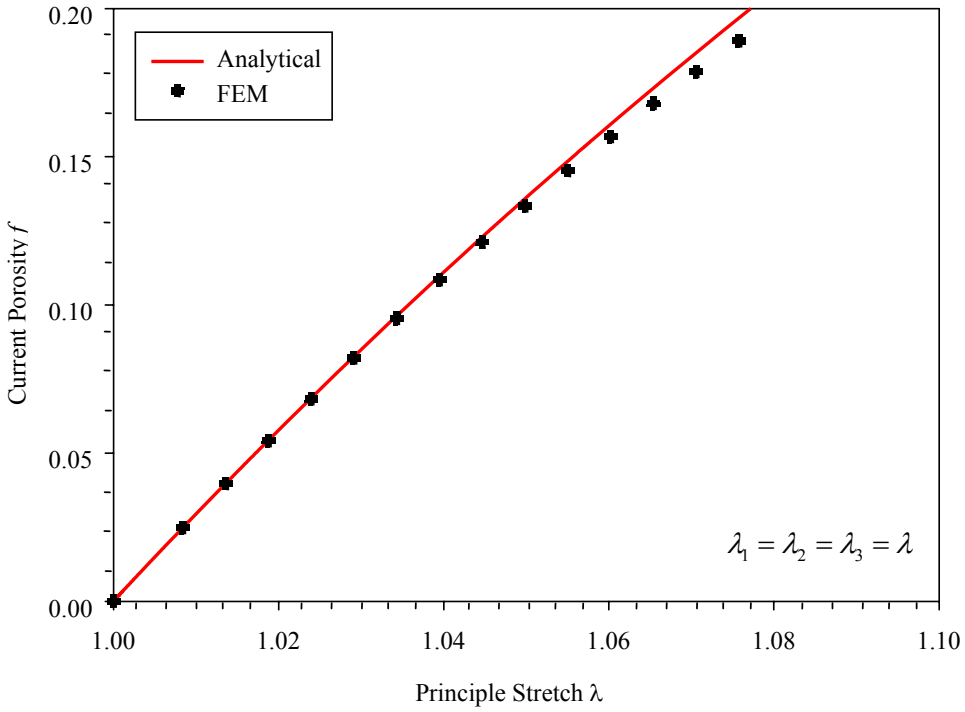

Figure 32. FEM result in current porosity f check on the 3D mesh models and analytical solution of initial porosity 10^{-4} with incompressible Neo-Hookean material (59).

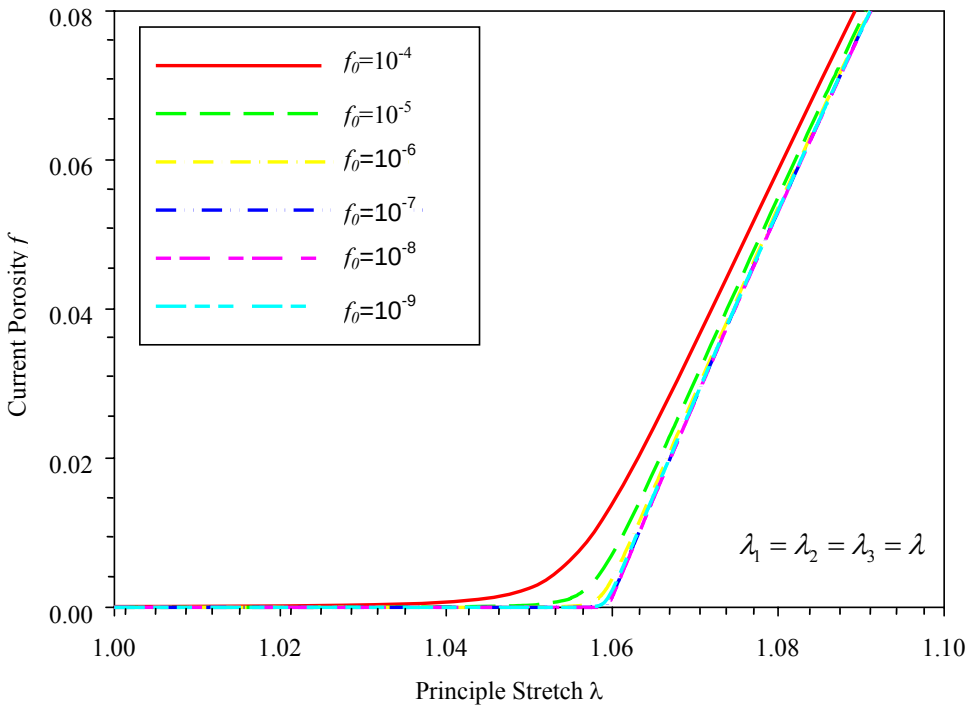

Figure 33. The FEM results of current porosity f on 3D mesh models of different initial porosity for compressible Neo-Hookean materials (59) with compressibility ratio $\mu'/\mu = 10$ under hydrostatic deformation.

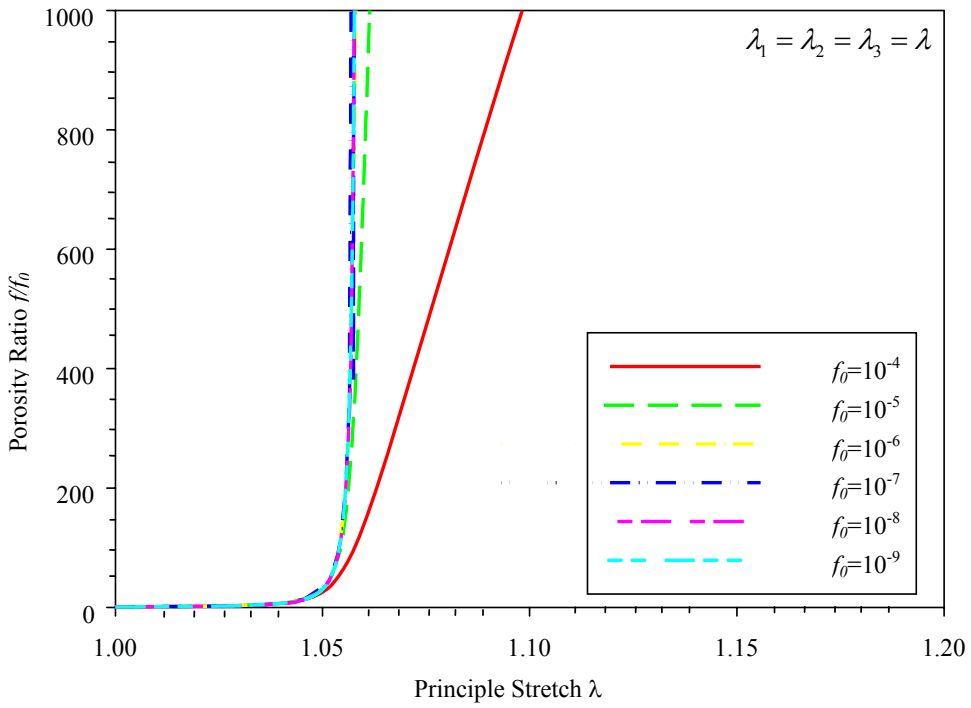

Figure 34. The FEM results of porosity ratio f/f_0 on 3D mesh models of different initial porosity for compressible Neo-Hookean materials (58) with compressibility ratio $\mu'/\mu = 10$ under hydrostatic deformation.

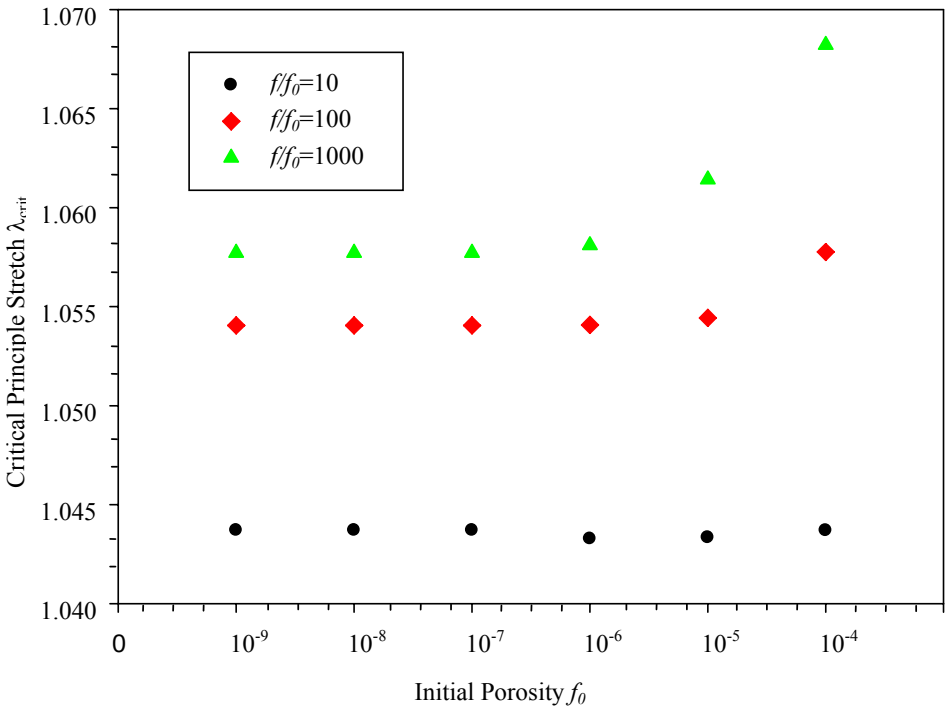

Figure 35. The FEM results of critical principle stretch λ_{crit}, which are generated by three criterions, on 3D mesh models of different initial porosity for compressible Neo-Hookean materials (58) with compressibility ratio $\mu'/\mu = 10$ under hydrostatic deformation.

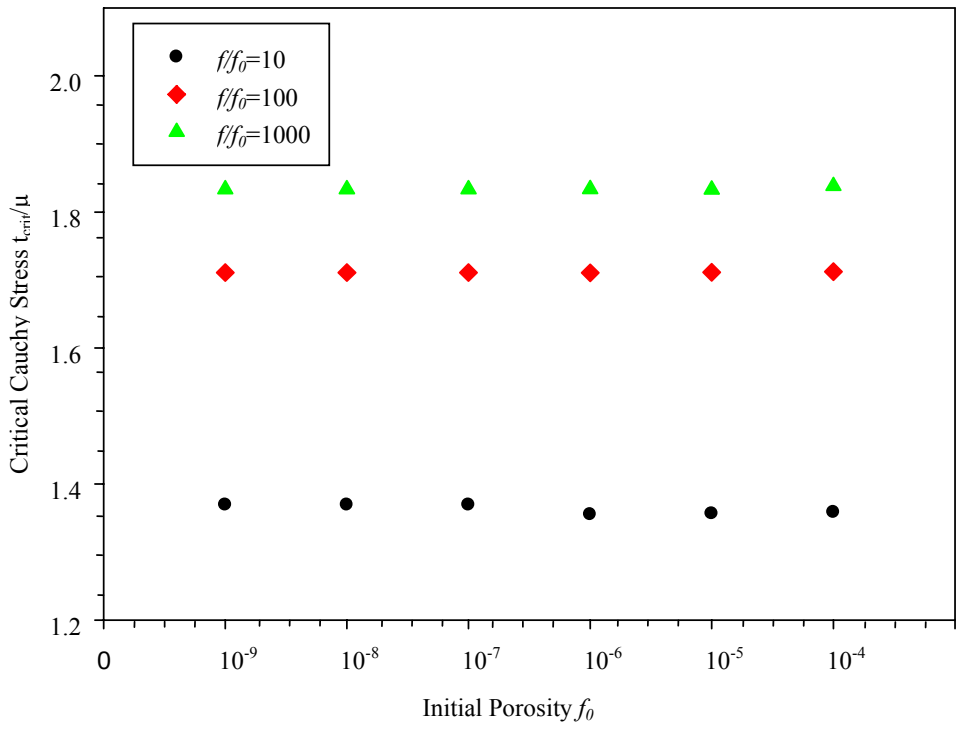

Figure 36. The FEM results of critical corresponding Cauchy stress t_{crit}/μ, which are generated by three criterions, on 3D mesh models of different initial porosity for compressible Neo-Hookean materials (58) with compressibility ratio $\mu'/\mu = 10$ under hydrostatic deformation.

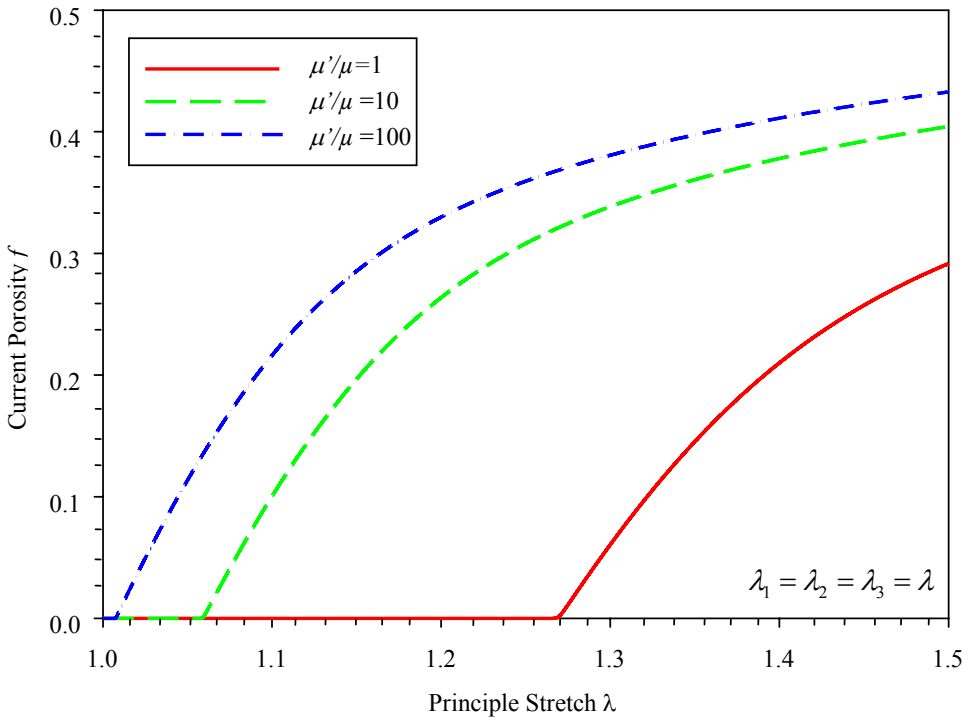

Figure 37. FEM results for absolute current porosity f on 3D mesh models of initial porosity $f_0 = 10^{-7}$ for compressible Neo-Hookean materials (58) with different compressibility ratio $\mu'/\mu = 1,10,100$ under hydrostatic deformations.

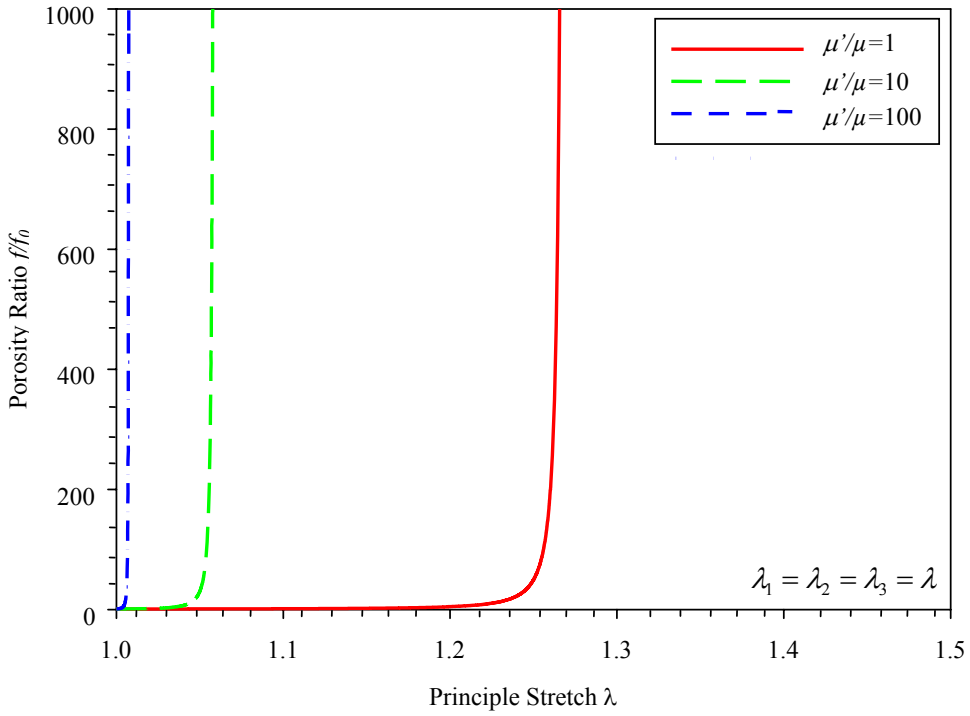

Figure 38. FEM results for porosity ratio f/f_0 on 3D mesh models of initial porosity $f_0 = 10^{-7}$ for compressible Neo-Hookean materials (58) with different compressibility ratio $\mu'/\mu = 1,10,100$ under hydrostatic deformations.

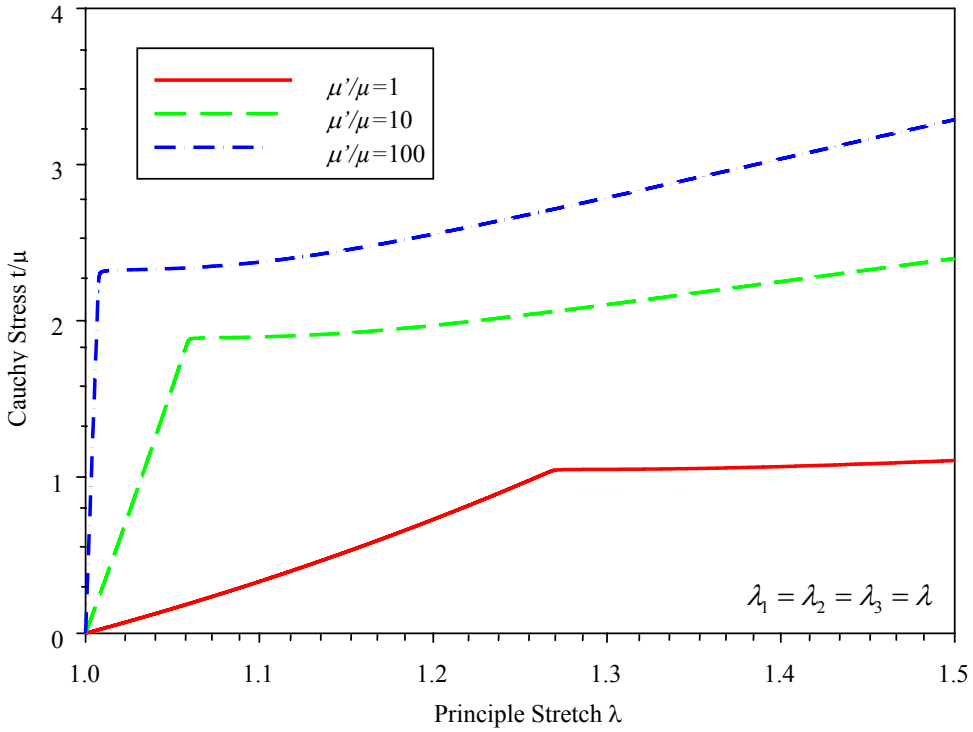

Figure 39. FEM results for corresponding Cauchy stress t/μ on 3D mesh models of initial porosity $f_0 = 10^{-7}$ for compressible Neo-Hookean materials (58) with different compressibility ratio $\mu'/\mu = 1,10,100$ under hydrostatic deformations.

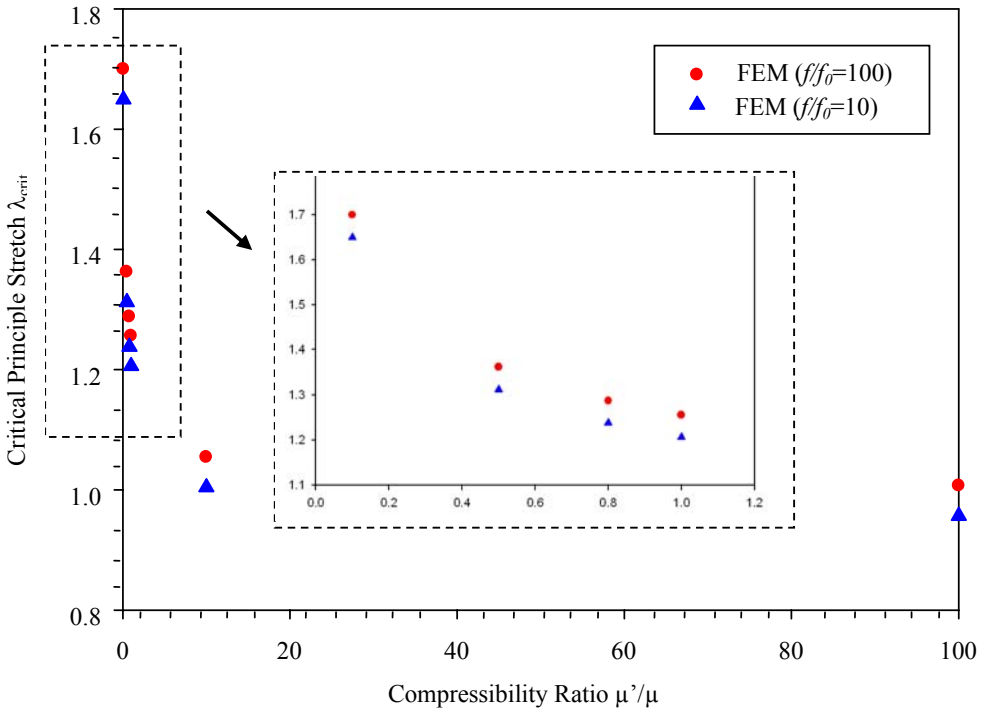

Figure 40. The critical stretch λ_{crit} at which cavitation occurs in compressible Neo-Hookean materials (58) subjected to hydrostatic deformation, as a function of the compressibility ratio μ'/μ from FEM calculations.

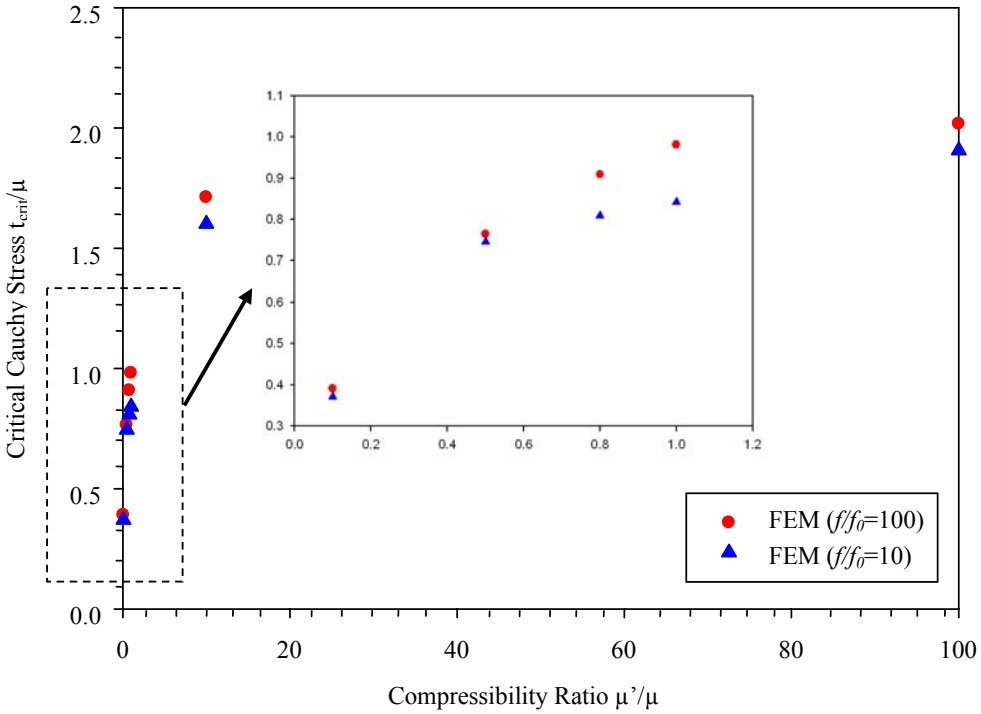

Figure 41. The critical corresponding Cauchy stress t_{crit}/μ at which cavitation occurs in compressible Neo-Hookean materials (61) subjected to hydrostatic deformation, as a function of the compressibility ratio from FEM calculations.

Appendix

Asymptotic expansion in the initial porosity limit $f_0 \to 0+$

In this appendix, we sketch out the asymptotic analysis associated with the limit $f_0 \to 0$ in the estimates (20) and (21) for the total elastic energy $\widehat{E}$ and current porosity f. The analysis is a bit unusual in the sense that as $f_0 \to 0$ the asymptotic behavior of the underlying variables is different depending of the applied loading $\overline{\mathrm{F}} = \mathrm{diag}(\overline{\lambda_1}, \overline{\lambda_2})$. In particular, for non-symmetric loading conditions $(\overline{\lambda_1} \neq \overline{\lambda_2})$—as opposed to hydrostatic loading $(\overline{\lambda_1} = \overline{\lambda_2})$—the asymptotic behavior for small deformations of up to order $\left|\overline{\mathrm{F}} - I\right|^2$ is different from the behavior for deformations larger than order $\left|\overline{\mathrm{F}} - I\right|^2$. In this appendix, we present details only for the large-deformation case, which is the relevant case for our purposes since cavitation does not occur in the small-deformation regime. It is noted that the asymptotic solution resulting from the heuristic derivation that follows has been checked to be in agreement with the full numerical solution.

Motivated by numerical evidence from the results for small values of f_0, we start out by assuming that the 4 relevant unknowns in this problem (i.e. l_1, l_2, l_3, l_4) are of the form

$$l_1 = a_1 + a_2 f_0 + O(f_0^2), \qquad l_2 = b_1 + b_2 f_0 + O(f_0^2)$$

$$l_3 = c_1 + c_2 f_0 + O(f_0^2), \qquad l_4 = d_1 + d_2 f_0 + O(f_0^2) \tag{A.1}$$

in the limit as $f_0 \to 0$. Here, $a_1, a_2, b_1, b_2, c_1, c_2, d_1, d_2$ unknown coefficients that need to be determined from the asymptotic analysis that follows. Having introduced the ansatz (A.1), it proves now helpful to spell out the corresponding expansions for the

components of $\overline{\mathrm{F}}^{(1)}$ and $\widehat{\mathrm{F}}^{(1)}$ -quantities needed in the eventual computation of the estimate (20) for $\widehat{E}$. Thus, substituting expressions (A.1) in following relation:

$$\left\langle \mathrm{F(X)} \right\rangle^{(1)} = \overline{\mathrm{F}}^{(1)} = \overline{\mathrm{F}} - f_0 \left[\mathrm{P}^{-1} - \mathrm{L} \right]^{-1} S^{(1)}(\overline{\mathrm{F}}) \tag{A.2}$$

leads to

$$\begin{aligned} \overline{F}_{11}^{(1)} &= \overline{\lambda}_1 + \overrightarrow{F}_{11}^{(1)} f_0 + O(f_0^2) \\ \overline{F}_{22}^{(1)} &= \overline{\lambda}_2 + \overrightarrow{F}_{22}^{(1)} f_0 + O(f_0^2) \end{aligned} \tag{A.3}$$

and, $\overline{F}_{12}^{(1)} = \overline{F}_{21}^{(1)} = 0$, where use has been made of the specific diagonal form (12) for the applied loading $\overline{F}$. The explicit form of the coefficients $\overrightarrow{F}_{11}^{(1)}$ and $\overrightarrow{F}_{22}^{(1)}$ in these last expressions is too cumbersome to be included here. In any case, at this stage it suffices to remark that they are known in terms of the coefficients a_1, b_1, c_1, and d_1 introduced in (A.1). Moreover, substituting (A.1) in following relations:

$$\begin{aligned} \widehat{F}_{11}^{(1)} &= \overline{\lambda}_1 - sign(\overline{J} - 1) \frac{q_1 k_3 + k_1}{\sqrt{4q_1^2 k_2 + 4q_1 k_3 + k_1}} \\ \widehat{F}_{22}^{(1)} &= \overline{\lambda}_2 - sign(\overline{J} - 1) \frac{4q_1 k_3 + k_1}{2\sqrt{4q_1^2 k_2 + 4q_1 k_3 + k_1}} \\ \widehat{F}_{11}^{(1)} \widehat{F}_{22}^{(1)} &= \left(\widehat{F}_{11}^{(1)} - \overline{\lambda}_1 \right) \left(\widehat{F}_{22}^{(1)} - \overline{\lambda}_2 \right) - k_3/2 \\ \left(\widehat{F}_{11}^{(1)} \right)^2 + \left(\widehat{F}_{22}^{(1)} \right)^2 &= k_4 + q_4 k_3 - 2q_4 \left(\widehat{F}_{11}^{(1)} - \overline{\lambda}_1 \right) \left(\widehat{F}_{22}^{(1)} - \overline{\lambda}_2 \right) \end{aligned} \tag{A.4}$$

leads to

$$\begin{aligned} \widehat{F}_{11}^{(1)} &= \overline{\lambda}_1 + x_1 f_0^{1/2} + x_2 f_0^{3/2} + O(f_0^{5/2}) \\ \widehat{F}_{22}^{(1)} &= \overline{\lambda}_2 + y_1 f_0^{1/2} + y_2 f_0^{3/2} + O(f_0^{5/2}) \\ \widehat{F}_{11}^{(1)} \widehat{F}_{22}^{(1)} &= p_1 f_0 + p_2 f_0^2 + O(f_0^3) \\ \left(\widehat{F}_{11}^{(1)} \right)^2 + \left(\widehat{F}_{22}^{(1)} \right)^2 &= s_1 f_0 + s_2 f_0^2 + O(f_0^3) \end{aligned} \tag{A.5}$$

where, similar to (A.2), the coefficients in these expressions are (known functions of the coefficients defined in (A.1)) too cumbersome to be given explicitly. In passing, it

is instructive to note from (A.5) that the "invariants" $\hat{\mathrm{I}}^{(1)} = \hat{\mathrm{F}}^{(1)} \bullet \hat{\mathrm{F}}^{(1)}$ and $\hat{J}^{(1)} = \det \hat{\mathrm{F}}^{(1)}$ take the asymptotic form

$$\begin{aligned} \hat{I}^{(1)} &= \bar{I} + \hat{I}_1^{(1)} f_0^{1/2} + \hat{I}_2^{(2)} f_0 + O(f_0^{3/2}) \\ \hat{J}^{(1)} &= \bar{J} + \hat{J}_1^{(1)} f_0^{1/2} + \hat{J}_2^{(2)} f_0 + O(f_0^{3/2}) \end{aligned} \tag{A.6}$$

Here, it is recalled that $\bar{I} = \bar{\mathrm{F}} \bullet \bar{\mathrm{F}} = \bar{\lambda}_1^2 + \bar{\lambda}_2^2$, $\bar{J} = \det \bar{\mathrm{F}} = \bar{\lambda}_1 \bar{\lambda}_2$, and $\hat{I}_1^{(1)} = 2\bar{\lambda}_1 x_1 + 2\bar{\lambda}_2 y_2$, $\hat{I}_2^{(1)} = x_1^2 + y_1^2 + s_1$, $\hat{J}_1^{(1)} = \bar{\lambda}_2 x_1 + \bar{\lambda}_1 x_2$ and $\hat{J}_2^{(1)} = x_1 y_1 - p_1$.

Next, by making use of expressions (A.1), (A.3), (A.5) and (A.6) in following equation,

$$S^{(1)}(\hat{\mathrm{F}}^{(1)}) - S^{(1)}(\bar{\mathrm{F}}) = L(\hat{\mathrm{F}}^{(1)} - \bar{\mathrm{F}}) \tag{A.7}$$

A hierarchical system of equations is obtained for the unknown coefficients introduced in (A.1). The first set of equations, of order $O(f_0^0)$, can be shown to yield the following two non-trivial relations:

$$d_1 = 2\Psi_{\bar{I}} \quad \text{and} \quad c_1 = \sqrt{(a_1 - 2\Psi_{\bar{I}})(b_1 - \Psi_{\bar{I}})} + \Psi_{\bar{J}} \tag{A.8}$$

where it is recalled that $\Psi_{\bar{I}} = \partial \Psi(\bar{I}, \bar{J}) / \partial I$ and $\Psi_{\bar{J}} = \partial \Psi(\bar{I}, \bar{J}) / \partial J$. The second set of equations, of order $O(f_0^{1/2})$, renders

$$b_1 = 2\Psi_{\bar{I}} + \frac{(a_1 - 2\Psi_{\bar{I}})(4\bar{\lambda}_2 \Psi_{\bar{I}} \Psi_{\bar{J}} + \bar{\lambda}_1 (4\Psi_{\bar{I}}^2 + \Psi_{\bar{J}}^2))^2}{(4\bar{\lambda}_1 \Psi_{\bar{I}} \Psi_{\bar{J}} + \bar{\lambda}_2 (4\Psi_{\bar{I}}^2 + \Psi_{\bar{J}}^2)^2} \tag{A.9}$$

Note that expressions (A.8) and (A.9) completely define the leading order behavior of the unknown moduli l_1, l_2, l_3, l_4 in (A.1) up to the coefficient a_1. More importantly, expressions (A.8) and (A.9) turn out to be sufficient—in spite of the fact that a1 is not known at this stage—to fully determine the first correcting terms of all components of $\bar{\mathrm{F}}^{(1)}$ and $\hat{\mathrm{F}}^{(1)}$. The results read as follows:

$$\overline{F}_{11}^{(1)} = -\frac{4\overline{\lambda}_2\Psi_{\bar{I}}\Psi_{\bar{J}} + \overline{\lambda}_1(4\Psi_{\bar{I}}^2 + \Psi_{\bar{J}}^2)}{4\Psi_{\bar{I}}^2 - \Psi_{\bar{J}}^2}$$
$$\overline{F}_{22}^{(1)} = -\frac{4\overline{\lambda}_1\Psi_{\bar{I}}\Psi_{\bar{J}} + \overline{\lambda}_2(4\Psi_{\bar{I}}^2 + \Psi_{\bar{J}}^2)}{4\Psi_{\bar{I}}^2 - \Psi_{\bar{J}}^2} \tag{A.10}$$

and $x_1 = y_1 = 0$,

$$p_1 = \frac{(4\overline{\lambda}_2\Psi_{\bar{I}}\Psi_{\bar{J}} + \overline{\lambda}_1(4\Psi_{\bar{I}}^2 + \Psi_{\bar{J}}^2))(4\overline{\lambda}_1\Psi_{\bar{I}}\Psi_{\bar{J}} + \overline{\lambda}_2(4\Psi_{\bar{I}}^2 + \Psi_{\bar{J}}^2))}{(4\Psi_{\bar{I}}^2 - \Psi_{\bar{J}}^2)^2}$$
$$s_1 = \frac{16\overline{I}\Psi_{\bar{I}}^4 + 64\overline{J}\Psi_{\bar{I}}^3\Psi_{\bar{J}} + 24\overline{I}\Psi_{\bar{I}}^2\Psi_{\bar{J}}^2 + 16\overline{J}\Psi_{\bar{I}}\Psi_{\bar{J}}^3 + \overline{I}\Psi_{\bar{J}}^4}{(4\Psi_{\bar{I}}^2 - \Psi_{\bar{J}}^2)^2} \tag{A.11}$$

Making use now of the explicit relations (A.10) and (A.11), together with the asymptotic expressions (A.3) and (A.5) for $\overline{\mathrm{F}}^{(1)}$ and $\hat{\mathrm{F}}^{(1)}$, it is straightforward to show that in the limit as $f_0 \to 0$ the estimate (20) for the total elastic energy $\widehat{E}$ reduces identically to equation (22) in the main body of the text.

Moreover, after having computed the correcting terms (A.10) for $\overline{\mathrm{F}}^{(1)}$, it is trivial to deduce (with the help of the global average condition $\overline{\mathrm{F}} = (1-f_0)\overline{\mathrm{F}}^{(1)} + f_0\overline{\mathrm{F}}^{(2)}$) that the average deformation gradient $\overline{\mathrm{F}}^{(2)}$ in the cavity of the LCM—a quantity needed in the computation of the estimate (21) for the porosity f—is of the form

$$\overline{F}_{11}^{(2)} = \frac{4\Psi_{\bar{I}}(2\overline{\lambda}_1\Psi_{\bar{I}} + \overline{\lambda}_2\Psi_{\bar{J}})}{4\Psi_{\bar{I}}^2 - \Psi_{\bar{J}}^2} + O(f_0)$$
$$\overline{F}_{22}^{(2)} = \frac{4\Psi_{\bar{I}}(2\overline{\lambda}_2\Psi_{\bar{I}} + \overline{\lambda}_1\Psi_{\bar{J}})}{4\Psi_{\bar{I}}^2 - \Psi_{\bar{J}}^2} + O(f_0) \tag{A.12}$$

$\overline{F}_{12}^{(2)} = \overline{F}_{21}^{(2)} = 0$, in the limit as $f_0 \to 0$. It then follows immediately that

$$\det\overline{\mathrm{F}}^{(2)} = \frac{16\Psi_{\bar{I}}^2(2\overline{\lambda}_1\Psi_{\bar{I}} + \overline{\lambda}_2\Psi_{\bar{J}})(2\overline{\lambda}_2\Psi_{\bar{I}} + \overline{\lambda}_1\Psi_{\bar{J}})}{(4\Psi_{\bar{I}}^2 - \Psi_{\bar{J}}^2)^2} + O(f_0) \tag{A.13}$$

and hence that in the limit as $f_0 \to 0$ the estimate (21) for the current porosity f reduces to equation (23), as given in the main body of the text.

For completeness, we record here that expressions (22) and (23) may be alternatively written in terms of the stretch-based form of the stored-energy function Φ as

$$\widehat{E}(\overline{\mathrm{F}}) = (1-f_0)\Phi(\overline{\lambda}_1,\overline{\lambda}_2) - \frac{\overline{\lambda}_1\Phi_{\overline{\lambda}_1}^3 - 3\Phi_{\overline{\lambda}_1}\Phi_{\overline{\lambda}_2}(\overline{\lambda}_2\Phi_{\overline{\lambda}_1} - \overline{\lambda}_1\Phi_{\overline{\lambda}_2}) - \overline{\lambda}_2\Phi_{\overline{\lambda}_2}^3}{2(\Phi_{\overline{\lambda}_1}^2 - \Phi_{\overline{\lambda}_2}^2)} + O(f_0) \tag{A.14}$$

and

$$f = \frac{4\Phi_{\overline{\lambda}_1}\Phi_{\overline{\lambda}_2}(\overline{\lambda}_1\Phi_{\overline{\lambda}_1} - \overline{\lambda}_2\Phi_{\overline{\lambda}_2})^2}{\overline{\lambda}_1\overline{\lambda}_2(\Phi_{\overline{\lambda}_1}^2 - \Phi_{\overline{\lambda}_2}^2)} + O(f_0) \tag{A.15}$$

where, similar to the notation employed in (A.14) and (A.15), $\Psi_{\overline{\lambda}_1} = \partial\Psi(\overline{\lambda}_1,\overline{\lambda}_2)/\partial\lambda_1$ and $\Psi_{\overline{\lambda}_2} = \partial\Psi(\overline{\lambda}_1,\overline{\lambda}_2)/\partial\lambda_2$.